MULTISCALE MODELS OF SEA ICE PHENOMENA

by

Christian Sampson

A dissertation submitted to the faculty of
The University of Utah
in partial fulfillment of the requirements for the degree of

Doctor of Philosophy

Department of Mathematics

The University of Utah

August 2017

The University of Utah Graduate School

STATEMENT OF DISSERTATION APPROVAL

The dissertation of **Christian Sampson**
has been approved by the following supervisory committee members:

Kenneth Golden,	Chair(s)	**5/31/17** Date Approved
Andrej Cherkaev,	Member	**5/31/17** Date Approved
Elena Cherkaev,	Member	**5/31/17** Date Approved
Courtenay Strong,	Member	**5/31/17** Date Approved
Jingyi Zhu,	Member	**5/31/17** Date Approved

by **Peter E. Trapa**, Chair/Dean of
the Department/College/School of **Mathematics**
and by **David B. Kieda**, Dean of The Graduate School.

ABSTRACT

Sea ice can be viewed as a composite material over multiple scales. On the smallest scale, sea ice is viewed as a two-phase composite of ice and brine. On the mesoscale, one may consider pancake ice and slush as a viscoelastic composite. On the larger scale, one may consider the mix of ice floes and water. With this view, a multitude of mathematical tools may be applied to develop novel models of physical sea ice processes. We model fluid and electrical transport viewing sea ice as a two-phase composite of ice and brine. We may then apply continuum percolation models to study critical behavior which we have experimentally confirmed. These percolation models suggest that the electrical conductivity and fluid permeability follow universal power law behavior as a function of brine volume fraction. We apply the results above for the electrical conductivity of sea ice to develop an inversion algorithm for surface impedance DC tomography. The algorithm retrieves both sea ice thickness and a layered stratigraphy of the sea ice resistivity. This is useful as resistivity carries information about the internal microstructure of the ice. We also apply network models to conductivity of sea ice and use some similar ideas to quantify the horizontal connectivity of melt ponds.

On the larger scale, we study the problem of ocean wave dynamics in the marginal ice zone of the Arctic and Antarctic. We adopt the view that the ice and slush may be viewed as a viscoelastic layer atop an inviscid ocean. Models like these produce dispersion relations which describe wave propagation and attenuation into the ice pack. These dispersion relations depend on knowledge of the effective viscoelasticity of the ice/slush mix. This is a difficult parameter to measure in practice. To get around this, we apply homogenization theory to derive bounds on these parameters in the low frequency limit. This is accomplished through the derivation of a Stieltjes integral representation, involving a positive measure of a self-adjoint operator, for the effective elasticity tensor of the ice water composite. We have also developed a simplified wave equation for waves in the ice-water composite.

Dedicated to my cousin and my friend Paul A. Zurn (1982-2017)

CONTENTS

CHAPTERS

LIST OF FIGURES

LIST OF TABLES

ACKNOWLEDGEMENTS

I would like to thank the entire University of Utah Mathematics Department where I have enjoyed my time as a student. I would also like to thank the National Science Foundation (NSF) for supporting me as an undergraduate through the Research for Undergraduates Experience (REU) grant which introduced me to the world of geophysical and applied mathematics. I would also like to thank the following particular people.

Distinguished Professor Kenneth M. Golden, for both being my Ph.D. adviser through graduate school and my mentor during my undergraduate years. I have been working with Professor Golden for 9 years in total and the experience has been invaluable for me. From him I received not just just mathematical training, but valuable life experience. He has also been the lead investigator on all of the projects I have worked on, is the principal author on many of the works here, has provided invaluable mathematical guidance direction, and is a constant source of ideas. I would especially like to thank him for giving me so many opportunities throughout the years, including travel to participate in field work in both the Arctic and Antarctic.

Professor Elena Cherkaev, for her invaluable guidance and wonderful classes throughout my time as a graduate student. She is an amazing teacher and mentor who will go out of her way to meet with her students. Much of the work in Chapter 8 is inspired by her earlier work.

Professor Jingyi Zhu, for his insights and enjoyable courses. He is a coauthor on many of the works in this thesis and the principal author of the paper presented in Chapter 5

Professor Nicholas Korevaar, for the amazing classes I took from him as an undergraduate as well as his guidance. His thoughtful teaching and homework assignments inspired me to love mathematics and always kept me thinking. I modeled my own teaching style after his and this has helped me to effectively share my love of mathematics with others.

Professor Andrej Cherkaev, for serving on my committee and the many wonderful classes I have taken from him. He always made an effort to make sure we saw the amazing applications mathematics has to the world around us.

Professor Courtney Strong, for serving on my committee and for his geophysical guidance. I especially appreciated his invaluable input on a recent NASA postdoc proposal I wrote while applying for jobs in anticipation of graduation.

Dr. Ben Murphy, for the many insightful conversations we have had as well as his friendship over the years.

Dr. Adam Gully, for his insights and advice throughout graduate school. Adam is also a coauthor on many of the works presented in this thesis. He is also responsible for taking much of the data used in the analysis made.

The mathematics department staff, past and present. In particular Paula Tooman for her help as Graduate Program Director, Sandy Hiskey for all of her help during her tenure in the department, and especially Della Rae Riker for her advice and for always going out of her way to help me when I needed it.

Dr. Joyce Lin, Joyce is a coauthor of the work presented in Chapter 3 and was a pleasure to work with in the Field. She ran the numerical simulations that established the Wenner 4 probe method as an accurate method for measuring the conductivity of sea ice presented in Chapter 2.

David Lubbers, for his wonderful friendship and hard working spirit. David is a coauthor on the works presented in Chapters 3 and 4. David also pioneered many of the methods we used to measure the fluid permeability in the Antarctic as well as new methods to measure the electrical permeability of sea ice. David was a special person who brought cheer to everyone he interacted with, he was a genuine person full of nothing but love for everyone he met, he will be missed by all who knew him.

Professor Hajo Eicken, for his geophysical guidance and the wonderful opportunity to participate in the 2013 sea ice field course in Barrow, AK. Professor Eicken is a coauthor on the work presented in Chapter 2. I have been lucky to work closely with Professor Eicken many times, and each has been an invaluable experience.

Professor Malcolm Ingham, Dr. Keleigh Jones, Professor James E. Reid and Professor Anthony Worby. They are all coauthors on the work presented in Chapter 2 and have provided invaluable guidance on that work. In particular, I would like to thank Professor Ingham for his instruction during the 2013 sea ice field course in Barrow AK and Professor Worby for his hard work involving both SIPEX I and SIPEX II. I would also like to acknowledge Professor Reid's work using Wenner Array's to thickness measurements of Antarctic sea ice, his methods were the basis of many of the measurements we have made.

Meenakshi Barjatia, Professor Tolga Tasdizn and Boya Song, they are coauthors on the material presented in Chapter 7 and led the development of the image processing algorithm used as well as the calculation of the conductance matrices. I was honored to be asked to participate in their work.

Professor Cynthia Furse, for her kind advice and guidance throughout my graduate career. I was also fortunate to spend time working with her in the field. Her tireless efforts always amazed me.

Professor Jean-Louis Tison for providing the crystallographic images displayed in Chapter 3 and his insights regarding the fluid transport processes of sea ice

All of my friends, especially Lizz and Dustin Kopta for their close friendship, and Dr. Danny Kopta for his kind friendship and advice.

My parents David and Mary-Michael Sampson. They have always been there for me whenever I have needed them and I could not have succeeded without their love and guidance.

My sister Laura, my best friend and confidante. She is a constant source of inspiration and someone I have always looked up to despite bring 5 years my junior.

My wife Donaji Lugo, her kind temperament and loving support has made me a better person and enabled me to complete my degree. I find I love her more with each passing day.

CHAPTER 1

INTRODUCTION

Sea ice is a critical component of the Earth's climate system and a sensitive indicator of climate change covering up to 10% of the Earth's oceans [27, 31]. The sea ice packs in both the Arctic and Antarctic serve as a habitat for diverse microbial communities that live in the brine laden porous microstructure of the ice. These algal and bacterial communities serve as primary producers for the complex food web of the polar regions [7, 15] and receive their nutrients from the ocean below the ice layer via fluid transport through the porous structure of the ice. Physically, sea ice is a boundary layer atop the ocean which mediates the transfer of momentum, heat, and moisture between the ocean and the atmosphere s[16, 31]. Sea ice also plays a major role in determining the Earth's overall albedo. With an albedo of $0.8 - 0.9$, depending on snow cover, sea ice reflects incoming shortwave solar radiation preventing it from becoming trapped in the Earth's atmosphere. However, at least since the beginning of the Earth observing satellite era, Arctic summer sea ice extent has been in decline with a more rapid decline over the last two decades [20]. One potential explanation for this rapid loss is the so called ice albedo feedback [21]. In a warmer climate, melt ponds, often fresh water ponds which form on the surface of the ice due to snow melt [4], may occur earlier in the melt season. This has the effect of lowering the overall albedo of the ice pack as these dark ponds absorb more incoming solar radiation. This melts more ice and snow, creating more melt ponds or exposing dark open ocean, which lowers the albedo further speeding up the process [20]. This is an important process to consider in any large scale climate model and one which is dependent on small scale processes. For example, melt ponds can drain into the ocean through the porous microstructure of sea ice when it is permeable enough [4]. It was observed in [8] that for brine volume fractions ϕ below about 5%, columnar sea ice is effectively impermeable. However, the ice becomes increasingly permeable for ϕ above

5%. In fact, for a typical bulk salinity of 5 ppt, the critical brine volume fraction $\phi_c = 5\%$ corresponds to a temperature of $T_c \approx -5°C$. As a result, this is often called the *rule of fives*. Interestingly, melt ponds will remain atop the sea ice when the ice is well above the 5% permeability threshold. This is primarily explained by the fact that a melt pond is comprised of fresh water. As its contents begin to percolate down through the ice the fresh water freezes and creates blockages in the pore space [23]. In addition the top layer of Arctic sea ice is typically granular which has a higher percolation threshold than that of columnar ice which is discussed in Chapter 3. There is mathematical evidence which suggests that the ice albedo feedback mechanism might allow for an extremely rapid and irreversible sea ice loss if the Arctic climate passes through a "Tipping point" [6, 1, 30]. Further, global climate models (GCM's) typically underestimate sea ice loss year to year [3, 29] suggesting the need for improvement of the parameterizations of these important processes. Melt ponds themselves display interesting mathematical behavior and undergo a transition in fractal geometry [11] when they begin to connect up at large scales. These connections allow the melt ponds to drain further as water from one may flow toward a large drainage point in a connected pond. We discuss a method to quantify this horizontal connectivity in Chapter 7.

Other parameters, such as sea ice extent and thickness, are important to obtaining accurate trajectories of the future of the ice pack. This is because accurate initial conditions can greatly improve predictions in chaotic systems such as the Earth's climate. Determining the thickness distribution is, however, a difficult problem. Ground measurements are impractical due to the vastness of the polar ice packs and as a result remote sensing becomes extremely important. Satellites operating at microwave frequencies are not capable of determining the thickness of the ice due to the extremely absorptive nature of sea ice at those frequencies. Other electromagnetic methods have been developed such as electromagnet induction (EMI) devices [9, 10, 25, 37] which can be mounted on ships, planes or helicopters. These methods rely on knowlege of the effective electrical properties of sea ice and how they vary with thickness, temperature, salinity, and ice type in order to obtain thickness information from the measurements.

Real time remote monitoring of the ice pack would also be of great use for data assimilation in GCM's. The electrical conductivity of sea ice is closely related to its fluid transport properties as well as its crystallographic structure. As mentioned, fluid flow through porous sea ice is a major controlling component in the evolution of melt ponds, which in turn, affects the ice pack albedo [4]. However, it also plays a major role in brine drainage and the evolution of salinity profiles [22, 36], snow ice formation, where sea water floods the ice surface and then freezes [17, 24], ocean-ice-atmosphere CO_2 exchanges [26], convection-enhanced thermal transport [16, 33], and biomass build-up fueled by nutrient fluxes [5, 7, 15, 31]. In Chapters 2 and 5 we discuss how the electrical properties of the ice can be connected to the microstructure as well as various aspects of the state of the ice. In Chapter 3 we discuss the differences in the critical brine volume fraction threshold for fluid permeability in granular and columnar ice, while in Chapter 4, we discuss the differences in the electrical properties of grannular and columnar ice.

Wave-ice interactions in the polar oceans comprise a complex but important set of processes influencing sea ice extent, ice pack albedo, and ice thickness [13, 28, 32]. The marginal ice zone (MIZ) is the region of sea ice cover that is close enough to the open ocean to be affected by its dynamics. Over the past several years there has been an increasing realization of the importance of wave-ice interactions in the growth and decay of the seasonal ice pack. Waves have always played an important role in shaping the MIZ, particularly in the Antarctic. Incoming waves from the southern ocean propagate into the ice pack, breaking and shaping the ice. In the Arctic, due to recent decrease in summer sea ice extent, wave propagation has become increasingly important to the dynamics of the ice pack. Because sea ice is an integral component of the Earth's climate system it is important to consider wave-ice interactions in any large scale sea ice model. This can be difficult due to the complexity of the processes at play as well as the numerical cost when modeling individual floes under wave action. There are also two scales at play here: on the small scale, for short wave length waves, wave scattering off of individual floes will heavily attenuate incoming waves along with some viscous effects. At the larger scale, long wave lengths, scattering plays a smaller role and longer waves typically attenuate much more slowly and propagate further into the ice pack [18, 14, 34, 13, 28]. Many studies of MIZ wave propagation focus on solitary floe models, where the scattering of an incoming wave is simplified to that of an isolated floe or multiple floes. Recently, however, continuum models have been proposed which treat the MIZ as a two-component composite of ice and slushy water atop an inviscid ocean. These models are particularly appropriate for longer wavelengths. The top layer has been taken to be purely elastic [2], purely viscous [12], and viscoelastic [35, 19]. At the heart of these models are effective parameters, namely, the effective elasticity, viscosity, and complex viscoelasticity. In practice, these effective parameters, which depend on the composite geometry and the physical properties of the constituents, are quite difficult to determine. To help overcome this limitation, we employ the methods of homogenization theory, in a quasi-static, fixed frequency regime, to find a Stieltjes integral representation for the complex viscoelasticity, discussed in Chapter 8. This integral representation involves the spectral measure of a self adjoint operator and provides bounds on the effective viscoelasticity. We are further able to develop simplified models of wave propagation and wave-ice breaking which capture many of the average properties of the MIZ.

1.1 Dissertation Outline

Here we present a breif over view of each subsequent chapter. This dissertation is a compilation of much of the work I have done and participated in as a graduate student with my colleagues. It is organized from the small scale to the large scale and is intended to highlight how the application of advanced mathematical techniques can be used to understand both sea ice and the polar regions, and their relation to Earth's climate.

In Chapter 2, *Electrical Signature of the Percolation Threshold in Sea Ice*, we explore the connection between the electrical properties of sea ice and the state of the ice itself and discuss application to remote sensing. In particular, we use percolation theory to connect the critical thresholds of fluid permeability and vertical conductivity in sea ice. Two different experiments conducted in the Arctic and Antarctic show that there is a strong electrical signature at the 5% critical brine volume fraction threshold. Further the data are accurately explained by percolation theory with the same critical exponent of 2 for fluid permeability. This enables us to connect specific electrical profiles to important fluid transport properties in the ice. Chapter 2 is a preprint with authors Kenneth M. Golden, Hajo Eicken, Adam Gully, Malcolm Ingham, Keleigh A. Jones, Joyce Lin, James E. Reid, Christian S. Sampson, and Anthony P. Worby.

In Chapter 3, *Critical Threshold Behavior of Fluid Transport in Granular Antarctic Sea Ice*, we explore the differences in the fluid transport properties between columnar and granular ice. As predicted by the compressed power model, we find that the percolation threshold for fluid permeability of granular sea ice is 10%, much higher than that of columnar sea ice. We present the results of measurements made during the Sea Ice Physics and Ecosystem Experiment II (SIPEX II) in 2012 off the east coast of Antarctica confirming the result. Chapter 3 is a preprint with authors Kenneth M. Golden, Christian S. Sampson, Adam Gully, David Lubbers, and Jean-Louis Tison. I would like to dedicate this chapter to David Lubbers.

In Chapter 4, *Variability in The Vertical Conductivity of Granular Sea Ice*, we explore the local variability in the vertical continuity of Antarctic granular sea ice as compared to columnar sea ice. We find that the vertical conductivity of columnar changes much more continuously for brine volume fractions above 5% than granular ice. We propose this difference as a possible way to electrically determine ice type in remote sensing applications. We further discuss the reasons for the differences. The data presented were taken during SIPEX II in 2012 off of the east coast of Antarctica. Chapter 4 is a preprint with authors Christian S. Sampson, Kenneth M. Golden, and David Lubbers.

In Chapter 5, *A Network Model for Electrical Transport in Sea Ice*, we explore a network model for electrical transport in sea ice based on statistical measurements of the brine microstructure. Particularly we consider a log-normal distribution describing the temperature dependence of the inclusion sizes, and connectivity information obtained from X-ray CT data. The numerical model agrees well with field data taken on SIPEX I in 2007 and could be use to aid in thickness measurements derived from electromagnetic measurements. Chapter 5 is a reprint originally published in *Physica B.*, **405** (2010) 3033-3036 with authors Jingyi Zhu, Kenneth M. Golden, Adam Gully, and Christian S. Sampson.

In Chapter 6 *Surface Impedance Tomography for Antarctic Sea Ice*, we explore the use of surface impedance tomography as it applies to determining ice thickness and composition. We explore n-layer inversions using data obtained with a Wenner array during SIPEX I in 2007. We show that accurate reconstructions of sea ice resistivity profiles can be done provided the proper regularization considerations are taken into account. Chapter 6 is a reprint originally published in *Deep-Sea Research II* **58** (2011) 1149-1157 with authors Christian S. Sampson, Kenneth M. Golden, Adam Gully, and Anthony P. Worby.

In Chapter 7, *Network Modeling of Arctic Melt Ponds*, We develop algorithmic techniques for mapping photographic images of melt ponds onto discrete conductance networks. We explore image processing methods which use mathematical morphology operations to produce conductance matrix representations of images of highly connected melt pond structures. Employing undirected graphs, we are able to map just the melt pond connections. The effective conductivity of these networks can be used to approximate lateral flow between connected ponds. This has relevance as connected ponds allow for the flow of melt water to large drainage features thus changing the albedo of the ice. Chapter 7 is a reprint originally published in *Cold Regions Science and Technology*, **124** (2016) 40-53 with authors Meenakshi Barjatia, Tolga Tasdizn, Boya Song, Christian S. Sampson, and Kenneth M. Golden.

In Chapter 8, *Wave-Ice Interaction in the Marginal Ice Zone*, we employ the tools of Homogenization Theory to develop the first bounds for the effective viscoelasticity of ice-water mix in the marginal ice zones of the Arctic and Antarctic. Wave-ice interaction is an important but difficult process to model, often numerically expensive. As a result continuum models have been developed which treat the ice-water mix as a single viscoelastic material atop an inviscid ocean. All of the models depend on knowledge of the effective rheological properties of the top layer and to date have only been guessed or estimated. However, we have developed a Stieltjes integral representation for the complex viscoelasticity involving the spectral measure of a self adjoint operator in the quasi-static limit. This produces rigorous bounds for the effective parameter which take into account the geometry of the ice floes. We further relate the effective parameter to a wave equation, valid in the quasi-static limit, which produces a simplified dispersion relation where the wave number and attenuation rate of plane-like waves propagating through the marginal ice zone are defined by the effective parameter itself. We are also able to use this relation in the reverse direction to extract data from in situ measurements of wave propagation made during SIPEX II in 2012. The data sit comfortably within the bounds. We also explore the use of this wave equation in capturing some of the average properties of the marginal ice zone such as the effect waves have on the floe size distribution and the extent of the marginal ice zone. Chapter 8 will be written up for publication and will include authors Christian Sampson, Elena Cherkaev, Ben Murphy, and Kenneth M. Golden.

1.2 References

[1] Dorian S. Abbot, Mary Silber, and Raymond T. Pierrehumbert. Bifurcations leading to summer Arctic sea ice loss. *Journal of Geophysical Research*, 116(D19), oct 2011.

[2] Howard F. Bates and Lewis H. Shapiro. Long-period gravity waves in ice-covered sea. *Journal of Geophysical Research*, 85(C2):1095, 1980.

[3] Julien Boé, Alex Hall, and Xin Qu. September sea-ice cover in the Arctic Ocean projected to vanish by 2100. *Nature Geoscience*, 2(5):341–343, mar 2009.

[4] H. Eicken, T. C. Grenfell, D. K. Perovich, J. A. Richter-Menge, and K. Frey. Hydraulic controls of summer Arctic pack ice albedo. *Journal of Geophysical Research: Oceans*, 109(C8):n/a–n/a, aug 2004.

[5] Hajo Eicken. The role of sea ice in structuring Antarctic ecosystems. *Polar Biology*, 12(1), apr 1992.

[6] I. Eisenman and J. S. Wettlaufer. Nonlinear threshold behavior during the loss of Arctic sea ice. *Proceedings of the National Academy of Sciences*, 106(1):28–32, dec 2008.

[7] C. H. Fritsen, V. I. Lytle, S. F. Ackley, and C. W. Sullivan. Autumn bloom of Antarctic pack-ice algae. *Science*, 266(5186):782–784, nov 1994.

[8] K. M. Golden, S. F. Ackley, and V. I. Lytle. The percolation phase transition in sea ice. *Science*, 282(5397):2238–2241, dec 1998.

[9] Christian Haas. Evaluation of ship-based electromagnetic-inductive thickness measurements of summer sea-ice in the Bellingshausen and Amundsen seas, Antarctica. *Cold Regions Science and Technology*, 27(1):1–16, feb 1998.

[10] Christian Haas, Sebastian Gerland, Hajo Eicken, and Heinz Miller. Comparison of sea-ice thickness measurements under summer and winter conditions in the Arctic using a small electromagnetic induction device. *GEOPHYSICS*, 62(3):749–757, may 1997.

[11] C. Hohenegger, B. Alali, K. R. Steffen, D. K. Perovich, and K. M. Golden. Transition in the fractal geometry of Arctic melt ponds. *The Cryosphere*, 6(5):1157–1162, oct 2012.

[12] Joseph B. Keller. Gravity waves on ice-covered water. *Journal of Geophysical Research: Oceans*, 103(C4):7663–7669, apr 1998.

[13] A. L. Kohout, M. J. M. Williams, S. M. Dean, and M. H. Meylan. Storm-induced sea-ice breakup and the implications for ice extent. *Nature*, 509(7502):604–607, may 2014.

[14] Alison L. Kohout, Michael H. Meylan, and David R. Plew. Wave attenuation in a marginal ice zone due to the bottom roughness of ice floes. *Annals of Glaciology*, 52(57):118–122, may 2011.

[15] P. Lizotte and R. Arrigo, editors. *Antarctic Sea Ice: Biological Processes, Interactions and Variability*. American Geophysical Union, 1998.

[16] V. I. Lytle and S. F. Ackley. Heat flux through sea ice in the western Weddell sea: Convective and conductive transfer processes. *Journal of Geophysical Research: Oceans*, 101(C4):8853–8868, apr 1996.

[17] Ted Maksym and Martin O. Jeffries. A one-dimensional percolation model of flooding and snow ice formation on Antarctic sea ice. *Journal of Geophysical Research: Oceans*, 105(C11):26313–26331, nov 2000.

[18] Michael H. Meylan, Luke G. Bennetts, and Alison L. Kohout. In situ measurements and analysis of ocean waves in the Antarctic marginal ice zone. *Geophysical Research Letters*, 41(14):5046–5051, jul 2014.

[19] Johannes E. M. Mosig, Fabien Montiel, and Vernon A. Squire. Comparison of viscoelastic-type models for ocean wave attenuation in ice-covered seas. *Journal of Geophysical Research: Oceans*, 120(9):6072–6090, sep 2015.

[20] Donald K. Perovich, Bonnie Light, Hajo Eicken, Kathleen F. Jones, Kay Runciman, and Son V. Nghiem. Increasing solar heating of the Arctic Ocean and adjacent seas, 1979–2005: Attribution and role in the ice-albedo feedback. *Geophysical Research Letters*, 34(19), oct 2007.

[21] Donald K. Perovich, Jacqueline A. Richter-Menge, Kathleen F. Jones, and Bonnie Light. Sunlight, water, and ice: Extreme Arctic sea ice melt during the summer of 2007. *Geophysical Research Letters*, 35(11), jun 2008.

[22] Chris Petrich and Hajo Eicken. Growth, structure and properties of sea ice. In *Sea Ice*, pages 23–77. Wiley-Blackwell.

[23] Chris Polashenski, Kenneth M. Golden, Donald K. Perovich, Eric Skyllingstad, Alexandra Arnsten, Carolyn Stwertka, and Nicholas Wright. Percolation blockage: A process that enables melt pond formation on first year Arctic sea ice. *Journal of Geophysical Research: Oceans*, 122(1):413–440, jan 2017.

[24] Dylan C. Powell. Effects of snow depth forcing on Southern Ocean sea ice simulations. *Journal of Geophysical Research*, 110(C6), 2005.

[25] J.E. Reid, A. Pfaffling, A.P. Worby, and J.R. Bishop. In situ measurements of the direct-current conductivity of Antarctic sea ice: Implications for airborne electromagnetic sounding of sea-ice thickness. *Annals of Glaciology*, 44(1):217–223, nov 2006.

[26] S. Rysgaard, J. Bendtsen, L. T. Pedersen, H. Ramløv, and R. N. Glud. Increased CO2 uptake due to sea ice growth and decay in the nordic seas. *Journal of Geophysical Research*, 114(C9), sep 2009.

[27] M. C. Serreze, M. M. Holland, and J. Stroeve. Perspectives on the Arctic's shrinking sea-ice cover. *Science*, 315(5818):1533–1536, mar 2007.

[28] V.A. Squire. Of ocean waves and sea-ice revisited. *Cold Regions Science and Technology*, 49(2):110–133, aug 2007.

[29] Julienne Stroeve, Marika M. Holland, Walt Meier, Ted Scambos, and Mark Serreze. Arctic sea ice decline: Faster than forecast. *Geophysical Research Letters*, 34(9), may 2007.

[30] I. Sudakov, S.A. Vakulenko, and K.M. Golden. Arctic melt ponds and bifurcations in the climate system. *Communications in Nonlinear Science and Numerical Simulation*, 22(1-3):70–81, may 2015.

[31] D.N. Thomas. *Sea Ice*. Wiley, 2016.

[32] Takenobu Toyota, Christian Haas, and Takeshi Tamura. Size distribution and shape properties of relatively small sea-ice floes in the Antarctic marginal ice zone in late winter. *Deep Sea Research Part II: Topical Studies in Oceanography*, 58(9-10):1182–1193, may 2011.

[33] H. J. Trodahl, M. J. McGuinness, P. J. Langhorne, K. Collins, A. E. Pantoja, I. J. Smith, and T. G. Haskell. Heat transport in McMurdo sound first-year fast ice. *Journal of Geophysical Research: Oceans*, 105(C5):11347–11358, may 2000.

[34] P. Wadhams. SAR imaging of wave dispersion in Antarctic pancake ice and its use in measuring ice thickness. *Geophysical Research Letters*, 31(15), 2004.

[35] Ruixue Wang and Hayley H. Shen. Gravity waves propagating into an ice-covered ocean: A viscoelastic model. *Journal of Geophysical Research*, 115(C6), June 2010.

[36] W. F. Weeks and S. F. Ackley. *The Growth, Structure, and Properties of Sea Ice*, pages 9–164. Springer US, Boston, MA, 1986.

[37] A.P Worby, P.W Griffin, V.I Lytle, and R.A Massom. On the use of electromagnetic induction sounding to determine winter and spring sea ice thickness in the Antarctic. *Cold Regions Science and Technology*, 29(1):49–58, apr 1999.

CHAPTER 2

ELECTRICAL SIGNATURE OF THE PERCOLATION THRESHOLD IN SEA ICE

In this chapter we explore the connection between the electrical properties of sea ice and the state of the ice itself and discuss application to remote sensing. In particular, we use percolation theory to connect the critical thresholds of fluid permeability and vertical conductivity in sea ice. Two different experiments conducted in the Arctic and Antarctic show that there is a strong electrical signature at the 5% critical brine volume fraction threshold. Further the data are accurately explained by percolation theory with the same critical exponent of 2 for fluid permeability. This enables us to connect specific electrical profiles to important fluid transport properties in the ice. Chapter 2 is a preprint with authors **Kenneth M. Golden, Hajo Eicken, Adam Gully, Malcolm Ingham, Keleigh A. Jones, Joyce Lin, James E. Reid, Christian S. Sampson, and Anthony P. Worby.**

2.1 Abstract

Fluid flow through sea ice governs a broad range of geophysical and biological processes in the polar marine environment. For example, the evolution of melt ponds and sea ice albedo, which is important in climate modeling, is constrained by drainage through the porous brine microstructure. However, for brine volume fractions below about 5%, columnar sea ice is effectively impermeable to fluid flow. In two different experiments conducted in the Arctic and Antarctic, we have found that this critical fluid transition exhibits a strong electrical signature, with sea ice resistivity rising sharply over three orders of magnitude near the brine connectivity threshold. The data are accurately explained by percolation theory, with the same universal critical exponent which captures fluid permeability. These results enable us to connect specific electrical profiles to important transport processes such as melt pond drainage, CO_2 pumping, and the flux of nutrients which

sustain biomass build-up.

2.2 Introduction

Polar sea ice is a key component of Earth's climate system, and a leading indicator of climate change [33, 30]. As a material sea ice is a composite of pure ice with brine and air inclusions. The brine phase hosts extensive microbial communities which sustain life in the polar oceans [33, 10]. Fluid flow through the porous microstructure mediates key processes impacting the climatology and biology of sea ice. Improving projections of the fate of Earth's sea ice cover and its ecosystems depends on a better understanding of these important processes and feedback mechanisms.

For example, the evolution of sea ice albedo represents a fundamental problem in climate modeling and a significant source of uncertainty in climate projections [7, 24]. The albedo of sea ice floes is determined by melt pond evolution [22, 24]. Drainage of the ponds, with a resulting increase in albedo, is largely controlled by the fluid permeability of the porous sea ice underlying the ponds [6, 14]. As ice recedes with melting, more water surface is exposed, which increases solar absorption, leading in turn to more melting, and so on. This *ice–albedo feedback* has played a significant role in the decline of the summer Arctic ice pack [23].

Fluid flow through sea ice governs the evolution of the salt budget and salinity profiles [33], convection-enhanced thermal transport [20], ocean-ice-atmosphere CO_2 exchanges [27], and the build-up of algal biomass fueled by nutrient fluxes [33, 10]. It also drives snow-ice formation, accounting for a significant portion of the ice produced in the Southern Ocean [21]. Sea water percolates upward through the porous microstructure, flooding the snow layer, and subsequently freezing.

While fluid flow is substantially restricted for brine volume fractions ϕ below about 5%, columnar sea ice is increasingly permeable for ϕ above 5% [13]. For a typical bulk salinity of 5 ppt, the critical porosity $\phi_c \approx 5\%$ corresponds to a temperature $T_c \approx -5^\circ$ C, which is known as the *rule of fives*. This critical behavior of the fluid permeability results from a connectivity or percolation threshold in the brine microstructure [13, 14, 25].

If the fluid transport properties of sea ice can be linked to its electrical properties, which is the aim of this paper, then new approaches can be brought to bear in monitoring the state of sea ice. For example, it could open the door to the development of sensors to enhance existing buoy networks, provide information on key ice processes, and improve integration with satellite data.

The electrical conductivity of sea ice has been studied over the past five decades [1, 3, 11, 17, 26, 34]. However, there have been no observations of critical behavior in electrical properties corresponding to the microstructural transition encapsulated in the rule of fives. Here we report on two types of experiments where electrical resistivity data clearly display critical behavior at the brine percolation threshold. The mathematical description we develop provides a rigorous link between fluid and electrical transport in sea ice, with both displaying the same type of universal critical behavior, thus laying the foundation for the techniques referred to above. In fact, we further develop this foundation by partitioning the range of resistivity values of our data into intervals which correspond to distinct regimes of fluid permeability characteristics and related process behavior, such as melt pond development, and fluxes of nutrients and CO_2.

One of the goals of this work is to obtain data on the linkages between electrical and hydraulic properties [35]. The value of such an approach lies in the potential to then extract information about other key variables describing the state of sea ice, e.g., pertaining to its rheology or potential to harbor microbial communities. Our results indicate that such information could potentially be obtained from measurements of electric properties via *in situ* drifting sensors that can monitor the evolution of sea ice nondestructively (Figure 2.1 d).

The findings presented here also have implications for measuring ice thickness, an important gauge of the impact of global warming. Not only are thickness data important in comparing climate model predictions to observed behavior, but in specifying the initial conditions necessary for long-term numerical simulations. Promising techniques for advanced airborne or surface-based measurements of ice thickness depend on the interaction of electromagnetic (EM) fields with sea ice. For example, there has been significant interest in the development of EM induction devices [15, 26] mounted on ships, planes and helicopters. These techniques, and the interpretation of the data to obtain thickness information, rely on knowledge of the electrical properties of sea ice, and how they vary with depth, temperature, salinity, and ice type. The results presented here shed significant light on such issues.

2.3 Measuring the Electrical Properties of Sea Ice

Sea ice is an anisotropic composite with vertically elongated brine inclusions and corresponding anisotropy in the effective fluid permeability and electrical conductivity tensors. Most methods for measuring sea ice conductivity involve indirect or inverse techniques, such as surface-based geoelectric profiling using a Wenner array of electrodes [3, 11, 17, 26, 29, 34]. Generally with these methods the vertical conductivity σ_v^* is inherently mixed with the horizontal components. Here we are most interested in σ_v^* due to its connection with vertical fluid flow.

During the Sea Ice Physics and Ecosystem Experiment (SIPEX) in September and October of 2007, we made *direct* measurements of σ_v^* in Antarctic pack ice by adapting a four probe Wenner array for use in cylindrical ice cores, as shown in Figure 2.1 a and b. The study area was located off the coast of East Antarctica, between 115° E and 130° E, and 64° S and 66° S. At 8 of the 15 ice stations along the cruise track of the Australian icebreaker *Aurora Australis*, we extracted vertical cores from thin first-year sea ice, with lengths ranging from 34 cm to 86 cm. Thermistor probes were inserted into small holes drilled every 5 cm. We used a Wenner electrode array along sections of the cores, connected to a YEW Earth Resistance Tester operating at 38 Hz. This set-up yields the resistance along the axis of the cylindrical ice core between probes P1 and P2, corresponding to the vertical direction *in situ*, with $a = L = 10$ cm (or $a = L = 5$ cm in some cases). We obtained 26 averaged data points from 67 raw measurements of the resistance between the inner probes. After the temperature and resistance measurements were taken, which took about 10 to 20 minutes, we cut each core into 10 cm sections which were later melted, so that we could obtain bulk salinity measurements for each section. The temperature and salinity measurements allowed us to calculate a brine volume fraction profile for each core [5].

In the Arctic, we used the technique of cross-borehole DC resistivity tomography [17, 18], as shown in Figure 2.1 c and d. The ice is probed in its natural state, utilizing two or four vertical strings of electrodes frozen into the ice. It has been shown that this method can be used to derive the horizontal component of the anisotropic resistivity profile. Moreover, it has been demonstrated that the vertical component of σ^* can be obtained as well [17, 18].

If a minimum of four electrode strings are used, the geometric mean of the vertical and horizontal components of σ^* can be derived, along with the horizontal component [17], yielding the vertical component.

Measurements of the temporal variation in the resistivity structure of first-year Arctic sea ice through spring warming have been made approximately 1 km off the coast of Barrow, Alaska at 71° 21′ 56.45″ N, 156° 32′ 39.01″ W. Electrode strings were installed in landfast first year ice in late January 2008. Cross-borehole measurements were made on 6 separate occasions between early April and mid June 2008, allowing both the horizontal and vertical components of the ice resistivity to be derived. A sea ice mass balance site and an ice core sampling program at the same location [4] provided ice temperature and salinity data, allowing the variation in resistivity structure to be correlated with brine volume fraction ϕ.

Plate electrodes in contact with the ends of a cylinder generate parallel field lines which make measuring the conductivity of the cylinder material relatively straightforward. To assess the accuracy of our four probe method, the commercial package Comsol 3.5a was used to create a finite element model of cylindrical sea ice cores 0.09 m in diameter and 0.5 m in length. Four metal probes of 0.004 m in diameter and 0.09 m in length were inserted approximately 0.07 m into the core, similar to Figure 2.1 b. When the current is injected through the outer probes instead of parallel plates, the nearby field lines show significant curvature. However, in a boxed measurement region where the inner probes are located, the field lines are relatively straight, thus minimizing the error between the actual conductivity of the material and what is measured by the array. Numerical simulations show that if the outer probes are 5 cm or more from the inner measurement region, this error is less than 8.5%, and is less than 1.5% if the distance is 10 cm or more, as for much of our data. This is illustrated in Figure 2.2.

When extracting a sea ice core to measure its properties, loss of brine is a principal concern. However, for our experiments we did not see any evidence of significant brine loss during the relatively short measurement periods with air temperatures ranging from about $-6°$ C to $-18°$ C (with most below $-9°$ C). Moreover, the probes are inserted deep into the core, minimizing contact with potential brine surface films. Our numerical simulations and these observations establish the Wenner array as a viable field method for *direct* resistivity measurements.

2.4 Modeling the Electrical Conductivity of Sea Ice

Lattice and continuum percolation theories [31] have been used to model a broad range of disordered materials where the connectedness of one phase dominates effective transport behavior. Consider the square ($d = 2$) or cubic ($d = 3$) network of bonds joining nearest neighbor sites on the integer lattice $\mathbb{Z}^d$. The bonds are assigned electrical conductivities $\sigma_0 > 0$ (open) or 0 (closed) with probabilities p and $1 - p$. Groups of connected open bonds are called open clusters, and the average cluster size grows as p increases. In this model there is a critical probability p_c, $0 < p_c < 1$, called the *percolation threshold*, where an infinite cluster of open bonds first appears. In $d = 2$, $p_c = \frac{1}{2}$, and in $d = 3$, $p_c \approx 0.25$. Typical configurations for the $d = 2$ square lattice above and below the threshold are shown in Figure 2.3. a and b.

Let $\sigma^*(p)$ be the effective conductivity of the network in the vertical direction [31]. For $p < p_c$, $\sigma^*(p) = 0$. For $p > p_c$ and near p_c, $\sigma^*(p)$ exhibits power law behavior,

$$\sigma^*(p) \sim \sigma_0(p - p_c)^t \ , \quad p \to p_c^+, \tag{2.1}$$

where t is the conductivity critical exponent. For lattices, t is believed to be universal, depending only on d. In $d = 2$, $t \approx 1.3$, and in $d = 3$, $t \approx 2.0$ [31]. There is also a rigorous bound [12] that $1 \leq t \leq 2$ in $d = 2$ and $d = 3$. Since $\sigma^*(p) \to 0$ as $p \to p_c^+$, the effective resistivity $\rho^*(p) = 1/\sigma^*(p)$ diverges as $p \to p_c^+$, with a vertical asympote at $p = p_c$. For two phase composites with finite component resistivities, like sea ice, the behavior only approximates the asymptote, and for $p < p_c$, ρ^* remains finite.

The fluid permeability $\kappa^*(p)$ corresponding to (2.1), where the open bonds are pipes of fluid conductivity $\kappa_0/\eta = r_0^2/8\eta$ and radius r_0, behaves like $\kappa^*(p) \sim \kappa_0(p - p_c)^e$ as $p \to p_c^+$, with e the fluid permeability exponent and η the fluid viscosity. For lattices, it is believed [31] that $e = t$. In the continuum, the exponents e and t can take non-universal values, and need not be equal, such as for the three dimensional Swiss cheese model [16, 31]. However, for lognormally distributed inclusions, as in sea ice, the behavior is *universal* [14, 2]. Thus for sea ice, $t = e \approx 2$.

In order to use percolation theory to quantitatively describe the vertical conductivity $\sigma_v^*(\phi)$, and to provide a link between fluid and electrical transport in sea ice, we recall our result [14] for the vertical fluid permeability

$$k_v^*(\phi) \sim 3\,(\phi - \phi_c)^2 \times 10^{-8}\ \mathrm{m}^2, \quad \phi \to \phi_c^+. \tag{2.2}$$

The scaling factor $k_0 = 3 \times 10^{-8}$ is estimated using critical path analysis [31, 9]. The effective behavior of media with a broad range of local conductances is dominated by a critical *bottleneck* conductance related to the minimal radius in a connected pathway of appropriate scale. To relate σ_v^* to k_v^*, we use the following relation from critical path analysis [9]. With r_c denoting the critical radius for our centimeter scale electrical experiments, then

$$k_v^* = \frac{r_c^2}{8}\,\frac{\sigma_v^*}{\sigma_b}\,, \tag{2.3}$$

where σ_b is the conductivity of brine, which depends [32] on temperature T. By measuring the radii of vertical pathways in X-ray tomography images [14, 25], we estimate a range in mm of $0.1 \le r_c \le 0.2$.

It is useful to consider the vertical conductivity formation factor $F = \sigma_v^*/\sigma_b$, which removes the dependence of the effective parameter on the changing conductivity of the brine, and depends only on the pore volume fraction and geometry. In view of (2.1) and (2.3), $F(\phi) \sim F_0\,(\phi - \phi_c)^2$ as $\phi \to \phi_c^+$, where $F_0 = 8k_0/r_c^2$. The estimates of 0.1 mm to 0.2 mm for r_c yield a range for F_0 of $6 \le F_0 \le 24$.

In order to compare our conductivity measurements with percolation theory, we must exclude data below $\phi_c \approx 0.05$ [14], since the theory is only valid for $\phi > \phi_c$. It is more illustrative to display the data in terms of the reciprocal $G = 1/F = \rho_v^*/\rho_b$, which is the vertical resistivity formation factor. In Figure 2.3 c and d we show the two data sets from the Antarctic and Arctic. By fixing the exponent $t = 2$ and the threshold value $\phi_c = 0.05$ in the above expression for $F(\phi)$, a statistical best fit of the data yields a value of $F_0 \approx 9$, which lies inside our predicted range, so that

$$F(\phi) \sim 9\,(\phi - 0.05)^2, \quad \phi \to \phi_c^+. \tag{2.4}$$

We see that the data agree well with the theory, and that they both exhibit divergent behavior with a vertical asymptote at the percolation threshold. Moreover, in the variables $x = \log(\phi - 0.05)$ and $y = \log F$, the line predicted by percolation theory in (2.4) is $y = 2x + \log F_0$, with $\log F_0 = 0.95, F_0 = 9$. Critical path analysis yields the bounds $0.8 \le$

$\log F_0 \leq 1.4$, and the best fit for the Antarctic data in f is $y = 1.99x + 0.93$, where 0.93 lies inside these bounds. In logarithmic variables, the error of the regression is 0.38 for the Arctic data and 0.22 for the Antarctic data (that is, approximately 68% of the Antarctic data are within 0.22 of the regression line). The increased scatter in the Arctic data is not surprising given the inverse computation required to obtain the formation factor data.

To model $\sigma_v^*(\phi)$ over all porosities, we consider features of the brine phase present over the full range $-$ some degree of small-scale connectivity, and self-similarity. Hierarchical models of spheres or other grains surrounded by smaller spheres, and so on, with brine in the pore spaces [14], were used to model $k_v^*(\phi)$. The simplest model yields a result of $k_v^*(\phi) = k_0\,\phi^3$. Via (2.3) we obtain an Archie's law result of $F(\phi) = F_0\,\phi^3$. A statistical best fit of our Antarctic data yields a value of $F_0 \approx 16$, which is in the estimated range. In Figure 2.4 a, our Antarctic data are shown along with fits derived from both models, and in b, Arctic permeability data [14] are shown relative to predictions from both models.

2.5 Discussion

Figure 2.5 illustrates how we can derive information about the permeability structure and relevant transport processes from resistivity soundings of Arctic sea ice with *in situ* electrode strings [18]. Thus, the different formation factor regimes shown correspond to different permeability classes, with the lowermost ice layers permeable enough to allow for gas and nutrient exchange conducive to biomass build-up and CO_2 pumping [19, 28], based on a critical permeability of 4×10^{-11} m^2, corresponding to a resistivity formation factor of 31.3 for $r_c = 0.1$ mm. This permeable base layer increases in vertical extent as the ice warms and thins due to bottom and surface melt. The ice interior is permeable enough to allow for meltwater flushing and reduction of ice salinity at surface ablation rates of 10 cm/d or less even prior to the onset of melt [8], corresponding to a resistivity formation factor of 625. High resistivity formation factors near the top in Figure 2.5 b are in part explained by such percolation of freshwater below accumulations of surface melt water.

Let us further examine how our results may be used to provide a better understanding of key processes like melt pond evolution. Incorporating such processes into climate models is critical to improving projections of climate change. Development and tuning of improved climate models could be significantly enhanced by ground truth information and monitoring of these key processes and the internal state of the sea ice.

For example, there is recent evidence from Arctic sea ice experiments (conducted by C. Polashenski and K. M. Golden in 2014) that percolation of freshwater from snowmelt into the upper layers of sea ice, and its subsequent freezing, could be fundamental to the very formation of melt ponds. This process reduces the permeability − thus increasing the electrical resisitivity, a process likely to have a recognizable electrical signature, as evidenced in Figure 2.5. Gauging the impact, for example, of changing Arctic snowfall on the availability of freshwater for melt pond formation could be made possible with methods based on our results. Melt pond drainage events, which can have a significant impact on sea ice albedo, often follow an increase in permeability through its percolation threshold, which has a strong electrical signature. Specific information on electrical and fluid transport profiles would enable estimates of drainage rates, duration of events, and in conjunction with a ponding model (e.g., [6, 7]) provide insight into albedo changes. The resulting input of fresh water into the upper ocean is also an important process which may be tracked through in-ice sensors.

In the Antarctic, snow-ice formation is a significant component of sea ice production. Knowledge of the time evolution of the conductivity−permeability profile in Antarctic sea ice can help delineate regions and time periods conducive to snow-ice formation, e.g., to estimate snow-ice production during storm-driven snowfall events. Like melt ponds in the Arctic, incorporating snow-ice formation into Antarctic sea ice and climate models is critical to improving projections.

Laboratory and field work [19, 36] have demonstrated the importance of permeability changes in spring in driving a key seasonal transition associated with disproportionate increases in gas transfer, nutrient exchange and biological activity in sea ice. In [36] it was demonstrated how this important transition enhances primary production within the ice and under the ice through seeding of under-ice waters. Since there is no clear surface expression of these processes, *in situ* measurement of electrical conductivity (e.g., through arrays sampling large volumes [18]) may serve as an important proxy and help track changes in the timing and magnitude of seasonal increases in gas, nutrient and biomass transfer.

2.6 Conclusions

It has been demonstrated in field experiments conducted in both the Arctic and Antarctic that sea ice exhibits critical behavior in its electrical transport properties at a percolation threshold. Such behavior provides the electrical signature of a key transition in fluid transport properties, known as the *rule of fives*, which determines whether or not fluid can flow through sea ice. This transition constrains a broad range of processes which are important in the geophysics and biology of the polar regions. The phenomenon is explained theoretically using percolation theory, which provides a universal power law describing the data from both poles, as well as a rigorous link between the fluid and electrical transport properties of sea ice. Our findings open the door to a new generation of techniques for *in situ* analysis and remote monitoring of transport processes, which can improve projections of the fate of Earth's ice packs and the response of polar ecosystems.

2.7 Acknowledgments

We are grateful for the support provided by the Division of Mathematical Sciences (DMS), the Arctic Natural Sciences (ARC) Program, and the Office of Polar Programs (OPP) at the US National Science Foundation (NSF) through grants DMS-0537015, DMS-0940249, and ARC-0934721. Joyce Lin was supported by an NSF Postdoctoral Fellowship through a VIGRE grant (DMS-0602219) to the Department of Mathematics at the University of Utah. Adam Gully and Christian Sampson were partially supported by the NSF Research Experiences for Undergraduates (REU) Program through the VIGRE grant, and graduate support through VIGRE. This work was also supported in part by the Australian Government through the Antarctic Climate and Ecosystems Cooperative Research Centre. Finally, we thank the crew of the *Aurora Australis* for their help and support during the SIPEX Antarctic expedition.

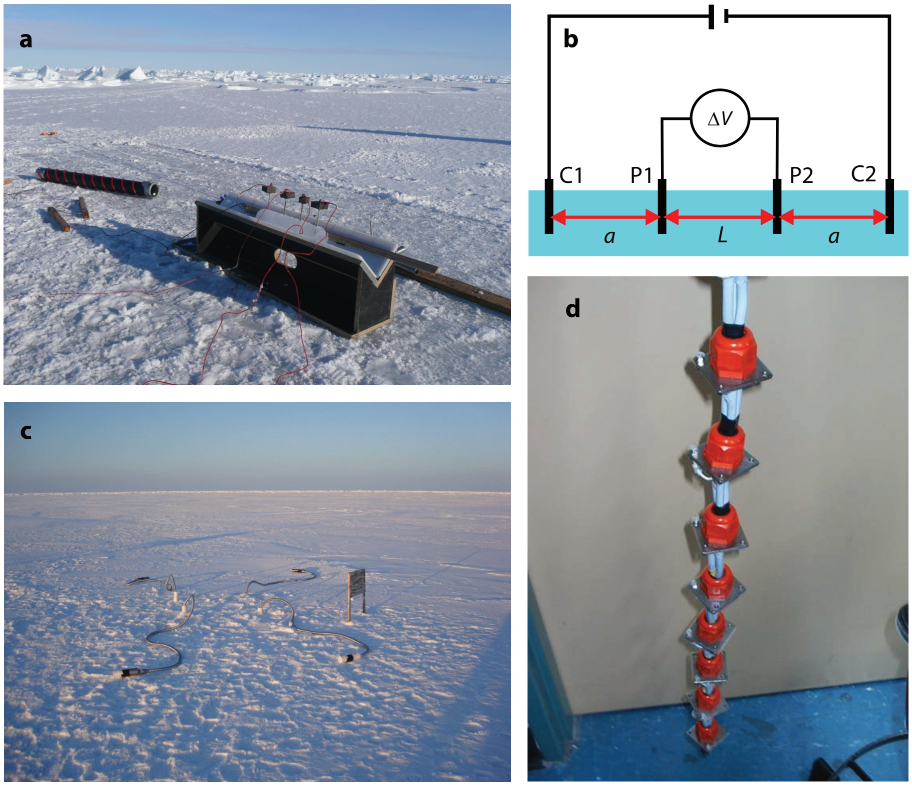

Figure 2.1: Examples of methods used to measure the conductivity the ice. (a) A Wenner electrode array is configured to measure the vertical conductivity of Antarctic sea ice, by inserting the four probes into an extracted ice core. (b) A current I is injected into the core through the outer electrodes C1 and C2. The potential difference ΔV resulting from the current flow is measured by the inner electrodes P1 and P2. The ratio $\Delta V / I$ is the resistance R in ohms. Here the electrode spacing is $L = 10$ cm and $a = 10$ cm. (c) A cross-borehole array is frozen into Arctic sea ice. The DC resistivity profile was tomographically reconstructed in the volume enclosed by the electrode strings. One of the strings, with 10 cm separation of the plates, is shown in (d).

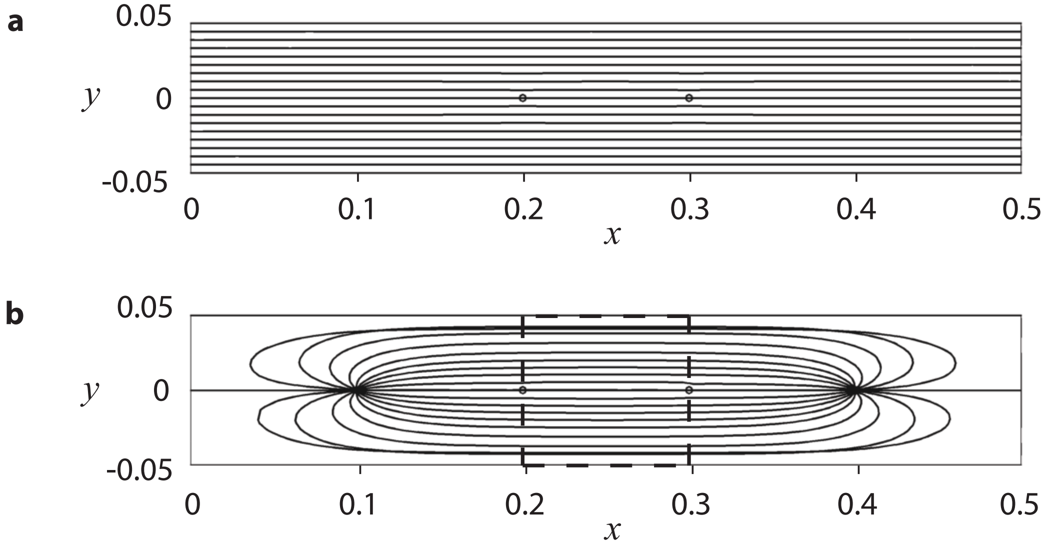

Figure 2.2: Comparing the field lines generated by parallel plates and a four probe Wenner array in sea ice. The field lines for a parallel plate configuration in (a) with those for a four probe Wenner array in vertically anisotropic ice (b).

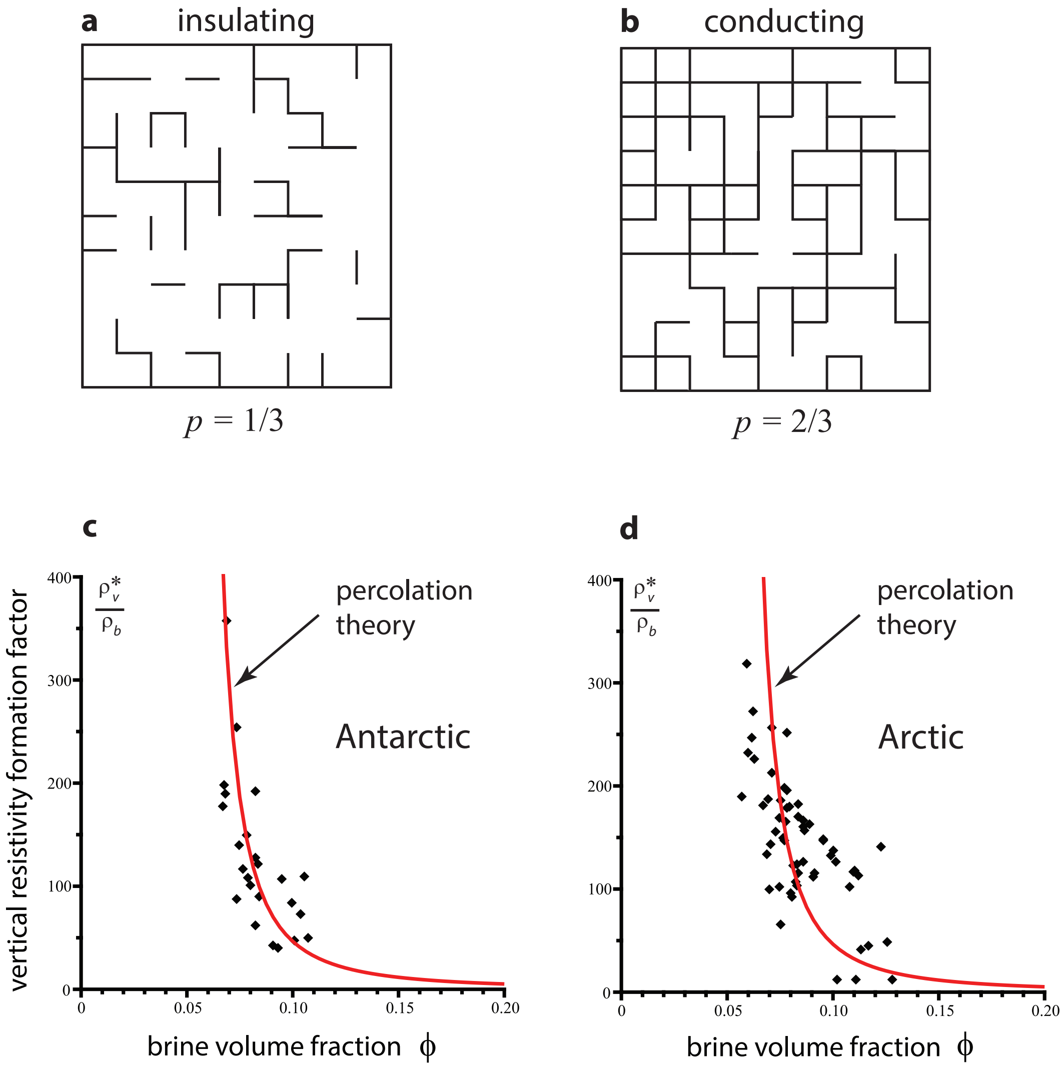

Figure 2.3: Examples of insulating and conducting two dimensional lattices and resistivity data from both the Arctic and Antarctic. The two dimensional square bond lattice below its percolation or connectivity threshold $p_c = 1/2$ in (a), and above in (b). We display the vertical resistivity formation factor data from the Antarctic in **(c)** and the Arctic in **(d)**, along with the same prediction from percolation theory in each. Both data and theory exhibit divergent behavior as ϕ approaches $\phi_c \approx 0.05$ from the right, with a vertical asymptote at $\phi = \phi_c$, electrically signaling the transition to relatively impermeable ice.

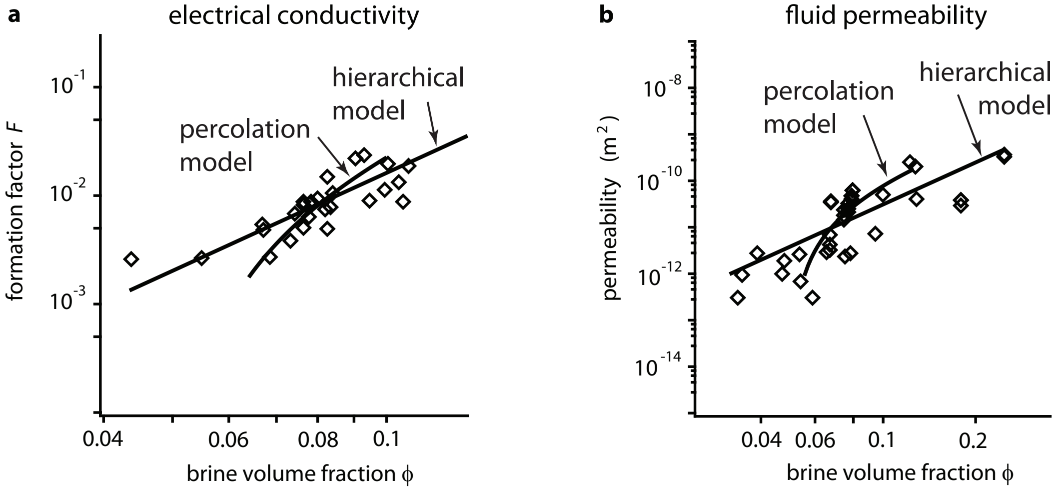

Figure 2.4: Antarctic conductivity data and Arctic fluid permeability data compared to percolation theory and the hierarchical model. (a) Antarctic field data on the vertical formation factor $F = \sigma_v^* / \sigma_b$ is compared with the hierarchical model $F(\phi) = F_0 \phi^3$. The prediction of percolation theory is also shown. (B) Comparison of Arctic fluid permeability data with the hierarchical model, along with percolation theory [14]. In both figures percolation theory captures the trend of the data in the percolation regime more closely than Archie's law.

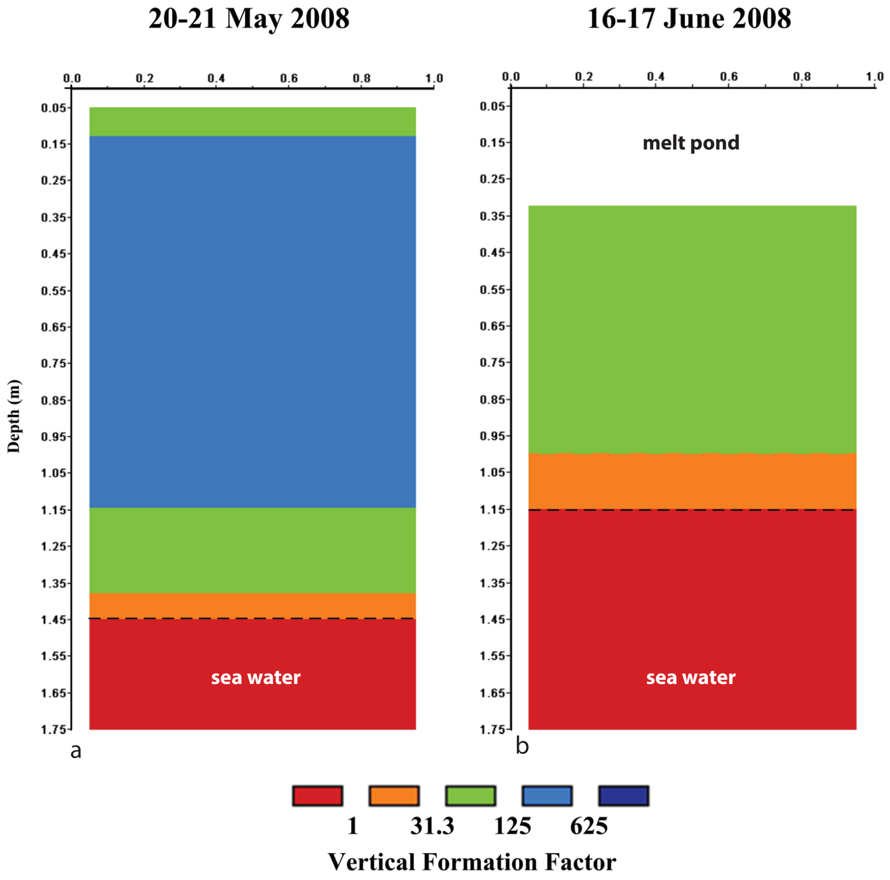

Figure 2.5: Cross-borehole tomographic reconstructions of the vertical resistivity formation factor for Arctic sea ice. We show in (a) the profile before melt pond formation, and (b) after. The evolution of resistivity structure is consistent with warming of the ice, thus increasing the fluid permeability and facilitating the infiltration of meltwater into the upper layer of sea ice from the surface. To connect the electrical properties of sea ice to its important processes, the range of the resistivity formation factor G is divided into five regimes: $G > 625$ (ice impermeable enough to allow ponds to grow for surface ablation rates 10 cm/d or larger for a critical pore radius of 0.1 mm); $125 < G \leq 625$, blue (ice impermeable enough to allow ponds to grow for surface ablation rates between 10 and 50 cm/d for a critical pore radius of 0.1 mm); $31.3 < G \leq 125$, green (at formation factors of 31.3 or larger ice is impermeable from the perspective of CO_2 exchange and build-up of nutrients and biomass in the ice [28], and sufficiently impermeable to drainage to support surface ponding); $1 < G \leq 31.3$, orange (highly permeable ice that allows for CO_2 pumping and build-up of nutrients and biomass); $G \leq 1$, red (assumed to be free water column). Only the most resistive ice $G > 625$ is not shown.

2.8 References

[1] J. Addison. Electrical properties of saline ice. *J. Appl. Phys.*, 40:3105–3114, 1969.

[2] B. Berkowitz and I. Balberg. Percolation approach to the problem of hydraulic conductvity in porous media. *Transport in Porous Media*, 9:275–286, 1992.

[3] R. G. Buckley, M. P. Staines, and W. H. Robinson. In situ measurements of the resistivity of Antarctic sea ice. *Cold Reg. Sci. Technol.*, 12(3):285–290, 1986.

[4] M. L. Druckenmiller, H. Eicken, M. A. Johnson, D. J. Pringle, and C. C. Williams. Towards an integrated coastal sea-ice observatory: System components and a case study at Barrow, Alaska. *Cold Reg. Sci. Technol.*, 56:61–72, 2009.

[5] H. Eicken. Growth, microstructure and properties of sea ice. In D. N. Thomas and G. S. Dieckmann, editors, *Sea Ice: An Introduction to its Physics, Chemistry, Biology and Geology*, pages 22–81. Blackwell, Oxford, 2003.

[6] H. Eicken, T. C. Grenfell, D. K. Perovich, J. A. Richter-Menge, and K. Frey. Hydraulic controls of summer Arctic pack ice albedo. *J. Geophys. Res. (Oceans)*, 109(C18):C08007.1–C08007.12, 2004.

[7] D. Flocco, D. L. Feltham, and A. K. Turner. Incorporation of a physically based melt pond scheme into the sea ice component of a climate model. *J. Geophys. Res.*, 115:C08012 (14 pp.), doi:10.1029/2009JC005568, 2010.

[8] J. Freitag and H. Eicken. Meltwater circulation and permeability of Arctic summer sea ice derived from hydrological field experiments. *J. Glaciol.*, 49:349–358, 2003.

[9] A. P. Friedman and N. A. Seaton. Critical path analysis of the relationship between permeability and electrical conductivity of three-dimensional pore networks. *Water Resources Res.*, 34(7):1703–1710, 1998.

[10] C. H. Fritsen, V. I. Lytle, S. F. Ackley, and C. W. Sullivan. Autumn bloom of Antarctic pack-ice algae. *Science*, 266:782–784, 1994.

[11] K. Fujino and Y. Suzuki. An attempt to estimate the thickness of sea ice by electrical resistivity method ii. *Low Temp. Sci.*, A21:151–157, 1963.

[12] K. Golden. Convexity and exponent inequalities for conduction near percolation. *Phys. Rev. Lett.*, 65(24):2923–2926, 1990.

[13] K. M. Golden, S. F. Ackley, and V. I. Lytle. The percolation phase transition in sea ice. *Science*, 282:2238–2241, 1998.

[14] K. M. Golden, H. Eicken, A. L. Heaton, J. Miner, D. Pringle, and J. Zhu. Thermal evolution of permeability and microstructure in sea ice. *Geophys. Res. Lett.*, 34:L16501 (6 pages and issue cover), doi:10.1029/2007GL030447, 2007.

[15] C. Haas. Late-summer sea ice thickness variability in the Arctic Transpolar Drift 1991-2001 derived from ground-based electromagnetic sounding. *Geophys. Res. Lett.*, 31:L09402, doi:10.1029/2007GL030447, 2004.

[16] B. I. Halperin, S. Feng, and P. N. Sen. Differences between lattice and continuum percolation transport exponents. *Phys. Rev. Lett.*, 54(22):2391–2394, 1985.

[17] M. Ingham, D. J. Pringle, and H. Eicken. Cross-borehole resistivity tomography of sea ice. *Cold Reg. Sci. Technol.*, 52:263–277, 10.1016/jcoldregions.2007.05.002, 2008.

[18] K. A. Jones, M. Ingham, D. J. Pringle, and H. Eicken. Temporal variations in sea ice resistivity: Resolving anisotropic microstructure through cross-borehole dc resistivity tomography. *J. Geophys. Res.*, 115:C11023, doi:10.1029/2009JC006049, 2010.

[19] Brice Loose, Lisa Miller, Scott Elliot, and Timothy Papakyriakou. Sea ice biogeochemistry and material transport across the frozen interface. *Oceanography*, 24(3):202–218, sep 2011.

[20] V. I. Lytle and S. F. Ackley. Heat flux through sea ice in the Western Weddell Sea: Convective and conductive transfer processes. *J. Geophys. Res.*, 101(C4):8853–8868, 1996.

[21] T. Maksym and T. Markus. Antarctic sea ice thickness and snow-to-ice conversion from atmospheric reanalysis and passive microwave snow depth. *J. Geophys. Res.*, 113:C02S12, doi:10.1029/2006JC004085, 2008.

[22] D. K. Perovich, T. C. Grenfell, B. Light, and P. V. Hobbs. Seasonal evolution of the albedo of multiyear Arctic sea ice. *J. Geophys. Res. (Oceans)*, 107(C10):8044, doi:10.1029/2000JC000438, 2002.

[23] D. K. Perovich, B. Light, H. Eicken, K. F. Jones, K. Runciman, and S. V. Nghiem. Increasing solar heating of the Arctic Ocean and adjacent seas, 1979-2005: Attribution and role in the ice-albedo feedback. *Geophys. Res. Lett.*, 34:L19505, doi:10.1029/2007GL031480, 2007.

[24] C. Polashenski, D. Perovich, and Z. Courville. The mechanisms of sea ice melt pond formation and evolution. *J. Geophys. Res. C (Oceans)*, 117:C01001 (23 pp.), doi:10.1029/2011JC007231, 2012.

[25] D. J. Pringle, J. E. Miner, H. Eicken, and K. M. Golden. Pore-space percolation in sea ice single crystals. *J. Geophys. Res. (Oceans)*, 114:C12017, 12 pp., doi:10.1029/2008JC005145, 2009.

[26] J. E. Reid, A. Pfaffling, A. P. Worby, and J. R. Bishop. In situ measurements of the direct-current conductivity of Antarctic sea ice: Implications for airborne electromagnetic sounding of sea-ice thickness. *Ann. Glaciol.*, 44:217–223, 2006.

[27] S. Rysgaard, J. Bendtsen, L. T. Pedersen, H. Ramløv, and R. N. Glud. Increased CO_2 uptake due to sea ice growth and decay in the Nordic Seas. *J. Geophys. Res.*, 114:C09011, doi:10.1029/2008JC005088, 2009.

[28] S. Rysgaard, R. N. Glud, M. K. Sejr, J. Bendtsen, and P. B. Christensen. Inorganic carbon transport during sea ice growth and decay: A carbon pump in polar seas. *J. Geophys. Res.*, 112:C03016, doi:10.1029/ 2006JC003572, 2007.

[29] C. Sampson, K. M. Golden, A. Gully, and A. P. Worby. Surface impedance tomography for Antarctic sea ice. *Deep Sea Res. II*, 58:1149–1157, 2011.

[30] M. C. Serreze, M. M. Holland, and J. Stroeve. Perspectives on the Arctic's shrinking sea-ice cover. *Science*, 315:1533–1536, 2007.

[31] D. Stauffer and A. Aharony. *Introduction to Percolation Theory, Second Edition*. Taylor and Francis Ltd., London, 1992.

[32] A. Stogryn and G. J. Desargant. The dielectric properties of brine in sea ice at microwave frequencies. *IEEE Trans. Antennas Propagat.*, AP-33(5):523–532, 1985.

[33] D. N. Thomas and G. S. Dieckmann, editors. *Sea Ice, 2nd Edition*. Wiley-Blackwell, Oxford, 2009.

[34] F. Thyssen, H. Kohnen, M. V. Cowan, and G. W. Timco. DC resistivity measurements on the sea ice near pond inlet. *Polarforschung*, 44:117–126, 1974.

[35] P. Wong. The statistical physics of sedimentary rocks. *Physics Today*, 41(12):24–32, 1988.

[36] Jiayun Zhou, Bruno Delille, Hajo Eicken, Martin Vancoppenolle, Frédéric Brabant, Gauthier Carnat, Nicolas-Xavier Geilfus, Tim Papakyriakou, Bernard Heinesch, and Jean-Louis Tison. Physical and biogeochemical properties in landfast sea ice (Barrow, Alaska): Insights on brine and gas dynamics across seasons. *Journal of Geophysical Research: Oceans*, 118(6):3172–3189, 2013.

CHAPTER 3

CRITICAL THRESHOLD BEHAVIOR OF FLUID TRANSPORT IN GRANULAR ANTARCTIC SEA ICE

In this chapter we explore the differences in the fluid transport properties between columnar and granular ice. As predicted by the compressed power model, we find that the percolation threshold for fluid permeability of granular sea ice is 10%, much higher than that of columnar sea ice. We present the results of measurements made during the Sea Ice Physics and Ecosystem Experiment II (SIPEX II) in 2012 off the east coast of Antarctica confirming the result. Chapter 3 is a preprint with authors **Kenneth M. Golden, Christian S. Sampson, Adam Gully, David Lubbers, and Jean-Louis Tison.** I would like to dedicate this chapter to David Lubbers.

3.1 Abstract

The fluid permeability of sea ice governs a broad range of physical and biological processes in the polar marine environment. For example, in the Arctic, melt pond drainage is largely controlled by the fluid permeability of the ice. Melt ponds in turn have a significant effect on ice albedo, a critical parameter in climate models. Algae in the ice depend on nutrients from the ocean transported through the porous microstructure of sea ice when it is permeable. Columnar sea ice is effectively impermeable for brine volume fractions below about 5%, while above this threshold fluid can flow through the ice. In the Antarctic, granular ice, with a much different crystallographic structure, makes up a significant portion of the ice pack. Data gathered during SIPEX II in 2012, as well as mathematical models, indicate that the percolation threshold for the fluid permeability of granular sea ice is around 10%. This is significantly higher than for columnar ice. These findings are significant, as both ecological models involving nutrient transport and physical process models must take this into account, for example, modeling snow-ice

formation, an important component of ice production in the Southern Ocean.

3.2 Introduction

The polar sea ice packs are a key component of the global climate system and are sensitive indicators of climate change. They also host extensive algal and bacterial communities that sustain life in the polar oceans. In addition, they play a major role in regulating gas exchanges in the polar regions and are an important factor in the Earth's overall albedo, all of which are important parameters in global and polar climate models. Fluid flow through the porous structure of sea ice is an integral component of these important processes and properties of the ice. It also serves as the mechanism for the nutrient replenishment necessary to sustain the algal and bacterial communities which live in the ice. The ability of fluid to flow in the ice depends heavily on its microstructure and exhibits critical behavior in relation to both its crystallographic structure and brine volume fraction. Previously it was believed that granular ice was permeable for brine volume fractions above 5%, a value used in many current sea ice models. While this is the critical threshold for columnar ice, we find that it is not so for granular ice. Along with a theoretical prediction of the critical threshold, we present the first measurements of the permeability of Antarctic sea ice and show that for granular sea ice, which makes up nearly 40% of Antarctic sea ice, the critical threshold is much higher at 10%. This new result must be considered for any model in which fluid flow through sea ice is a factor.

Our focus here is on key sea ice processes that must be better understood to improve the predictions of climate models and the future of the polar icepacks, as well as the microbial communities that live there. In particular, fluid flow through porous sea ice is a major controlling component in the evolution of melt ponds which in turn affects the ice pack albedo [5], brine drainage and the evolution of salinity profiles [4, 34], snow ice formation, where sea water floods the ice surface and then freezes [22, 27], ocean-ice-atmosphere CO_2 exchanges [29], convection-enhanced thermal transport [21, 33], and biomass build-up fueled by nutrient fluxes [3, 9, 20, 30]. For example, it is believed that ice albedo feedback has played a significant role in the declines observed in the Arctic [26]. Snow-ice formation, on the other hand, may have played a part in thickening the Antarctic sea ice pack [22, 27], and may become more important in the Arctic with increased precipitation and thinning ice, making the ice more susceptible to flooding.

The fluid permeability of sea ice plays a key role in understanding such processes, and in parameterizing them in large-scale models. To date, columnar microstructures have received disproportionate attention, mostly due to their prevalence in Arctic sea ice and their importance in undisturbed ice growth [4, 19, 34]. However, granular microstructures, which lack intragranular inclusions and exhibit a film of brine enveloping individual grains, are particularly important for processes which are relevant to climate studies. For example, granular ice is common in surface layers in the Arctic [24, 25], which directly underlie the melt ponds controlling ice albedo. Examination of the crystalline structure in sea ice from a recent trans-Arctic survey [25] showed a striking increase in overall granular ice fraction, of just over 40% compared to previous observations of around 10% [15]. In the Antarctic it has long been observed that granular ice [6, 22, 16, 35] accounts for up to 40% of the sea ice pack. Snow-ice in particular, with a granular microstructure itself, accounts for over a quarter of the ice found in the Southern Ocean, with much higher fraction in some regions [23]. An accurate accounting of sea ice processes involving fluid flow in climate, biological, and biogeochemical models thusly relies on knowledge of fluid permeability of granular ice.

Golden et al. have observed that for brine volume fractions ϕ below approximately 5%, columnar sea ice is effectively impermeable to fluid flow, yet increasingly permeable for ϕ above 5% [11]. For a typical bulk salinity of 5ppt this critical brine volume fraction $\phi_c \approx 5\%$ corresponds to a critical temperature $T_c \approx -5^\circ$ C, which is known as the *rule of fives*. The critical brine volume fraction was explained in terms of the *percolation threshold* in a continuum model for compressed powders which has been used to understand the behavior of stealthy or radar absorbing materials. A comprehensive theory for the vertical fluid permeability $k(\phi)$ of columnar sea ice was developed, and validated experimentally with laboratory and Arctic field data in [12]. Microscale imaging methods based on X-ray computed tomography (CT) and pore structure analysis methods were also developed to provide detailed pictures of the brine microstructure and the evolution of its connectivity with temperature [12, 28].

During September and October of 2012, we measured the fluid permeability of first year Antarctic pack ice as participants in the Australian Sea Ice Physics and Ecosystem Experiment II (SIPEXII) aboard the ice breaker *Aurora Australis* off the east coast of Antarctica. Over 100 measurements of the fluid permeability of the ice were made covering a range of depths, temperatures and ice types. Full crystallographic cores were also taken at each site in order to correlate ice type to specific permeability measurements. The measurements corresponding to granular ice were then separated out. We found that the critical threshold for fluid flow in granular ice was around $\phi_c \approx 10\%$. For a typical salinity of around 5ppt, the corresponding critical temperature is around $T_c \approx -2.5°\text{C}$ [7]. Moreover as predicted by our percolation theoretic analysis in [12], we find here that the *universal* lattice critical exponent of about 2 for columnar ice in the Arctic still accurately describes the take-off of $k(\phi)$ above the threshold ϕ_c.

The behavior we find in the percolation threshold for fluid transport in granular ice is explained by the compressed power model [17, 18]. By measuring the relative dimensions of the ice grains and the fluid inclusions in photomicrographs of granular sea ice, we obtain a percolation threshold of around 10% with the possibility of even higher thresholds for more finely grained microstructures.

In conjunction with our measurements from SIPEX II in 2012 the same critical threshold can be observed in tracer experiments from SIPEX I (September-October 2007). In the tracer experiments blocks of sea ice were extracted with a chain saw then turned upside down and dyes poured into shallow channels cut into sea ice bottom. Thin vertical slices were then cut from the blocks exposing the fluid fronts and layers of different microstructures and brine channels. The tracers easily penetrated the highly permeable bottom layer but stopped at a depth characterized by a brine volume fraction of about 10% shown in Figure 3.1.

3.3 Theory

In previous work [12, 13] we found rigorous upper bounds for k based on an observed lognormal distribution for the horizontal cross-sectional areas A of the brine inclusions [24]. In this case $Z = \ln A$ has a normal probability density with mean μ and variance σ^2,

$$P(Z) = \frac{1}{\sqrt{2\pi\sigma^2}}\, e^{-(Z-\mu)^2/2\sigma^2}. \tag{3.1}$$

The cross-sectional radius $a(\phi) = 7 \times 10^{-5} + (1.6 \times 10^{-4})\phi$ (m) increases according to measurements of pore sizes with temperature and is given by [2, 24]. The bound is a special case of optimal void bounds [31, 32], and takes the form

$$k(\phi) \leq \frac{\phi}{8\pi} \, \langle A(\phi) \rangle \, e^{\sigma^2}. \tag{3.2}$$

With variance $\sigma^2 \approx 1$ and $\langle A(\phi) \rangle = \pi a^2(\phi)$ as above [24], the *lognormal pipe bound* in equation (3.2) captures all our field data, as shown in Figure 3.2.

Percolation theory [10, 14, 31] can used to model transport in disordered materials where the connectedness of one phase, like brine in sea ice, dominates the effective behavior. Consider the square ($d = 2$) or cubic ($d = 3$) network of bonds joining nearest neighbor sites on the integer lattice $\mathbb{Z}^d$. The bonds are assigned fluid conductivities $\kappa_0 > 0$ (open) or 0 (closed) with probabilities p and $1 - p$. There is a critical probability p_c, $0 < p_c < 1$, called the *percolation threshold*, where an infinite, connected set of open bonds first appears. In $d = 2$, $p_c = \frac{1}{2}$, and in $d = 3$, $p_c \approx 0.25$. Let $\kappa(p)$ be the permeability of this random network in the vertical direction. For $p < p_c$, $\kappa(p) = 0$. For $p > p_c$, near the threshold $\kappa(p)$ exhibits power law behavior, $\kappa(p) \sim \kappa_0 (p - p_c)^e$ as $p \to p_c^+$, where e is the permeability critical exponent. For lattices, e is believed to be *universal*, depending only on d, and is equal to t, the lattice electrical conductivity exponent [1, 11, 14, 31]. In $d = 3$, it is believed [31] that $t \approx 2.0$, and there is a rigorous bound [10] that $t \leq 2$.

Although e can take non-universal values in the continuum, it was shown [14, 31] that for lognormally distributed inclusions the behavior is universal, with $e \approx 2$. The scaling factor k_0 is estimated using critical path analysis and microstructural observations [12]. Thus

$$k(\phi) \;\sim\; 3 \, (\phi - \phi_c)^2 \; \times 10^{-8} \;\; \mathrm{m}^2, \quad \phi \to \phi_c^+, \tag{3.3}$$

with $\phi_c \approx 0.1$ for granular ice.

3.4 Methods

We consider low Reynolds number flow of brine of viscosity η through sea ice. The volume fractions of brine and ice are ϕ and $1 - \phi$, respectively. The velocity and pressure fields in the brine satisfy the Stokes equations for incompressible fluids. Under appropriate assumptions [31], the homogenized velocity $\mathbf{v}(\mathbf{x})$ and pressure $p(\mathbf{x})$ satisfy Darcy's law and the incompressibility condition for the velocity,

$$\mathbf{v} = -\frac{1}{\eta} \, \mathbf{k} \, \nabla p, \qquad \nabla \cdot \mathbf{v} = 0, \tag{3.4}$$

where **k** is the permeability tensor, with vertical permeability $\mathrm{k}_{zz} = k$ in units of m^2.

The *in situ* permeability data were collected using a hydrological bail test [8], where partial cylindrical holes were drilled vertically into the sea ice, and the cores removed. Once the cores are removed, a tight fitting plastic pipe wrapped in foam (a packer) is inserted into the partial hole to block any horizontal inflow from the exposed edges. Pressure transducers were then placed at the bottom of the hole to measure the height $h(t)$ of the rising water column in meters as a function of time t in seconds. The bottom 2 cm of each partial core was used for a temperature and salinity measurement giving the brine volume fraction at the interface. The permeability of the ice underneath the borehole can be accurately estimated using the equation

$$h(t) = h(t_0)e^{-k_{exp}t(g\rho/\eta L)}, \tag{3.5}$$

with measured permeability k_{exp} (m^2), ice thickness beneath the borehole L (m), density ρ (kg m^{-3}), gravitational constant g (m s^{-2}), and initial time t_0. The vertical component of the permeability k can then be found using the calculations in [8] which are based on simulations of the pressure field in the ice and verified by measurement.

In order to correlate the permeability measurement with the ice type a full crystallographic core was taken at each measurement site. This core was immediately taken on board the *Aurora Australis* and a standard crystallographic analysis done in a $-20°$ c freezer using thin sections and cross polarizing film. We then matched the depths of our permeability measurements to the corresponding depths of the crystallographic core for the site to determine the ice type. For each site permeability measurements were kept to with in 3 meters of the crystallographic core to ensure close correspondence. The data were then separated out by crystal type.

The elementary analysis of the compressed powder model [17] we used to explain the rule of fives [11] shows that granular microstructures should display higher thresholds than columnar ice.

An image of the polycrystalline microstructure of Antarctic columnar ice under cross-polarization is shown in Figure 3.3 (A), and an image of granular ice is shown in (B). These samples were taken in the Bellingshausen Sea in October 2007 during the Sea Ice Mass Balance in the Antarctic (SIMBA) experiment.

In order to estimate the percolation threshold ϕ_c for fluid transport in Antarctic granular ice, we use a compressed powder model [11, 17]. In this model, large polymer spheres of radius R_p are mixed with much smaller metal spheres of radius R_m, and then the mixture is compressed. The main parameter controlling the threshold is the ratio $\xi = R_p/R_m$. An approximate formula for the critical volume fraction for percolation of the small metal spheres is given by $\phi_c = (1 + \xi\theta/(4X_c))^{-1}$, where θ is a reciprocal planar packing factor, and X_c is a critical surface area fraction of the larger particles which must be covered for percolation by the smaller particles [17]. Values based on microstructural analysis giving good agreement with experiments are $X_c = 0.42$ and $\theta = 1.27$. This mixture geometry is roughly similar to the ice-brine microstructure of sea ice, where the ice grains have radius R_i and the brine inclusions have radius R_b (or half the thickness of a brine film enveloping an ice grain), with $\xi = R_i/R_b$ in this case. We have estimated a range of ξ values from photomicrographs of granular microstructures, and obtained a representative value of around $\xi \approx 12$, leading to a threshold value of around $\phi_c \approx 10\%$, as illustrated in Figure 3.3 (C). We remark that fine-grained columnar ice which displays geometric similarity to classic granular ice can also exhibit these higher percolation threshold values, and that even finer grained frazil microstructures will likely have even higher thresholds.

3.5 Results and Implications

Using the full crystallographic cores taken at each site, all with in 2-3 meters of each permeability measurement, we can match the vertical permeability measurement to ice type based on depth. In Figure 3.4 (A) we display the granular permeability data along with the curve in equation (3.3). In Figure 3.4 (B) we show in logarithmic variables the percolation theory prediction along with a statistical best fit and the percolation theory curve showing close agreement. There is a clear take off in permeability values for brine volume fractions above 10% while below the threshold the ice is effectively impermeable. When plotting the data in logarithmic variables it is clear that for brine volume fractions above 10% percolation theory captures the data. In fact, a statical best fit of the data produces a curve $y = 1.97x + 17.5$ while percolation theory predicts a curve of $y = 2x + 17.5$.

In Figure 3.1 the results of our tracer experiments are shown, where we poured fluid tracers into inverted sea ice blocks. In each case the fluid descended through a layer of highly permeable sea ice, and stopped when it reached colder, impermeable granular ice (or fine-grained columnar ice) of brine volume fraction around 10%. These experiments vividly demonstrate that the critical threshold for fluid transport in Antarctic sea ice can be much higher than the 5% brine volume fraction of classic columnar sea ice.

This work demonstrates the applicability of percolation theory to fluid flow through sea ice for ice types beyond just columnar ice and shows that consideration of the microstructure of the ice is important when modeling any process in which fluid flow through the ice is relevant. Many processes such as nutrient replenishment, gas exchange and melt pond evolution depend heavily on fluid flow through the ice and are important factors in understanding the global climate system. In order to facilitate accuracy in models for both small-scale processes and large-scale climate models the higher than 5% threshold must be considered. This is particularly true in the Antarctic where up to 40% of the ice pack is comprised of granular sea ice.

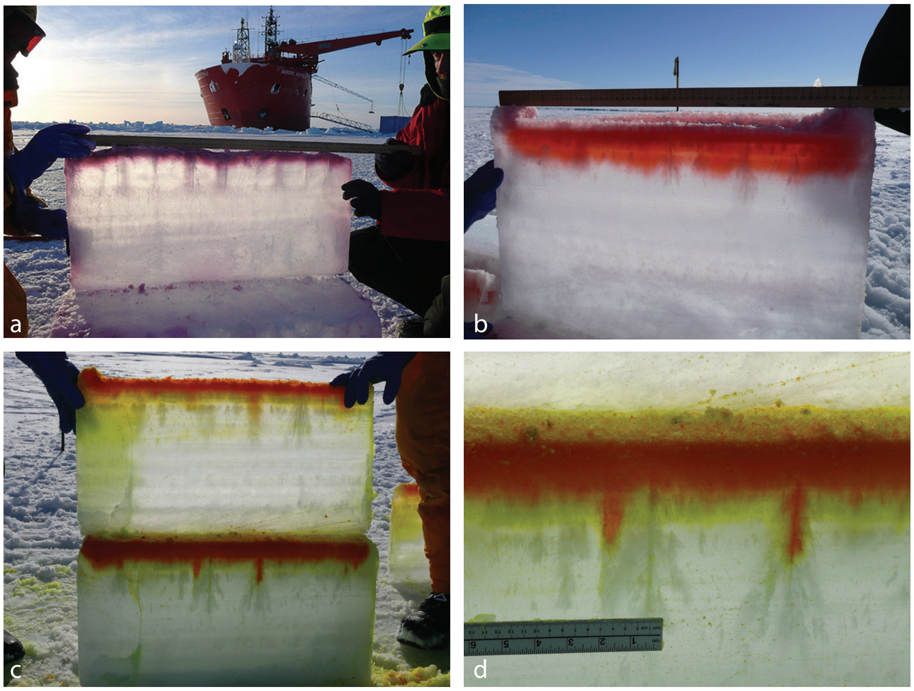

Figure 3.1: Penetration of tracers into inverted blocks of sea ice. The fluid penetrated about 5 cm into the ice in (a), about 10 cm in (b), and about 9 cm in (c) and (d). In each case the descending fluid passed through an initial layer a few centimeters deep of highly permeable ice of average brine volume fraction in the range 18.5% - 21.5%, until reaching relatively impermeable ice with brine volume fraction of about 10%, where it stopped flowing. In (a), the temperature and brine volume decreased more rapidly, and the tracer stopped after 5 cm. In (b) and (c) the 10% brine volume threshold was located about 10 cm down, and in (d) a tracer plume was also able to descend deeper through a large brine channel.

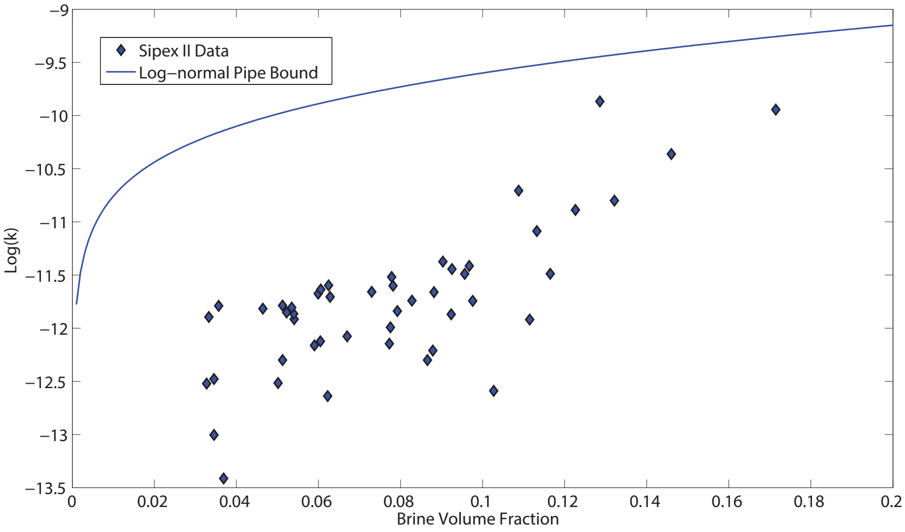

Figure 3.2: A comparison of *in situ* data on the vertical fluid permeability k (m^2) of Antarctic sea ice with a rigorous upper bound.

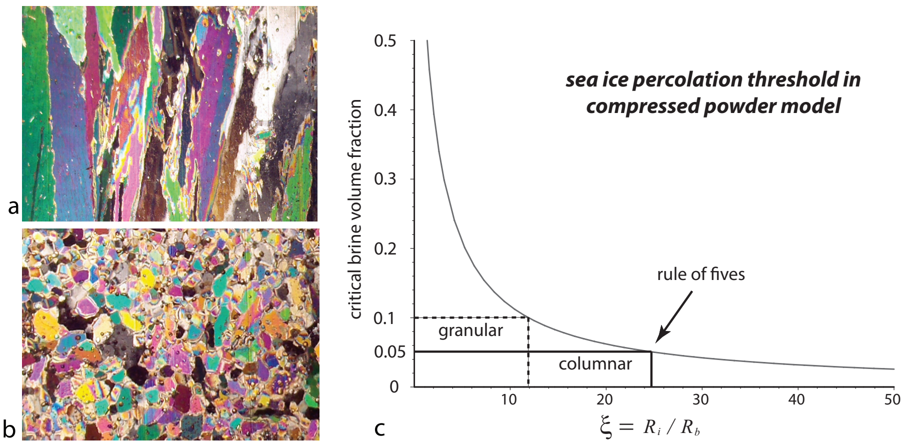

Figure 3.3: Examples of the different crystallographic structures of columnar and granular ice and their different permeability thresholds. Microstructures of columnar ice in (a) and granular ice in (b). In (c) we display the percolation threshold in the compressed powder model as a function of the ratio of the particle radii.

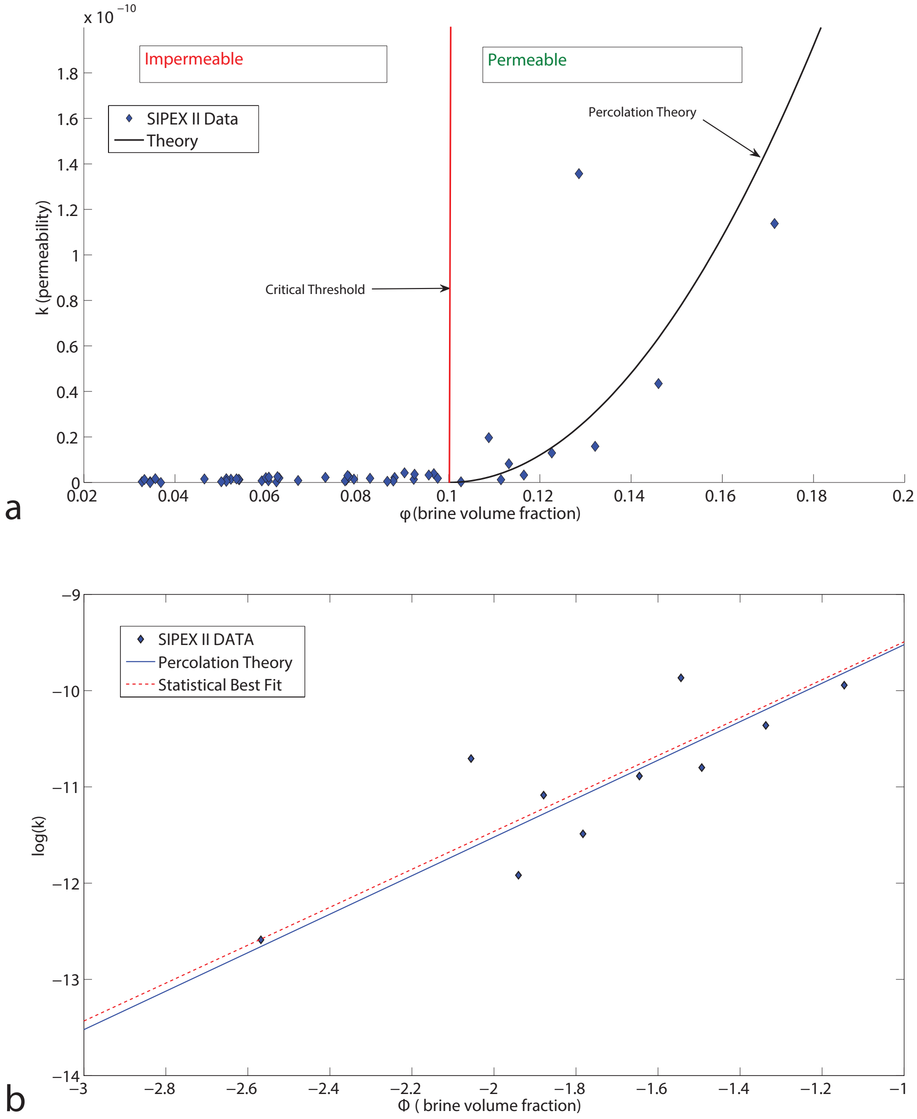

Figure 3.4: Comparison of *in situ* permeability data on k (m^2) for Antarctic sea ice with percolation theory. The data are displayed on a linear scale in (a) and on a logarithmic scale in (b), where a statistical best fit (dotted line) of the data is shown along with the prediction of percolation theory with $\phi_c \approx 0.1$.

3.6 References

[1] B. Berkowitz and I. Balberg. Percolation approach to the problem of hydraulic conductvity in porous media. *Transport in Porous Media*, 9:275–286, 1992.

[2] C. Bock and H. Eicken. A magnetic resonance study of temperature-dependent microstructural evolution and self-diffusion of water in Arctic first-year sea ice. *Ann. Glaciol.*, 40:179–184, 2005.

[3] H. Eicken. The role of sea ice in structuring Antarctic ecosystems. *Polar Biol.*, 12:3–13, 1992.

[4] H. Eicken. Growth, microstructure and properties of sea ice. In D. N. Thomas and G. S. Dieckmann, editors, *Sea Ice: An Introduction to its Physics, Chemistry, Biology and Geology*, pages 22–81. Blackwell, Oxford, 2003.

[5] H. Eicken, T. C. Grenfell, D. K. Perovich, J. A. Richter-Menge, and K. Frey. Hydraulic controls of summer Arctic pack ice albedo. *J. Geophys. Res. (Oceans)*, 109(C18):C08007.1–C08007.12, 2004.

[6] Hajo Eicken. *Deriving Modes and Rates of Ice Growth in the Weddell Sea from Microstructural, Salinity and Stable-Isotope Data*, pages 89–122. American Geophysical Union, 2013.

[7] G. Frankenstein and R. Garner. Equations for determing the brine volume of sea ice from -0.5^o to -22.9^o C. *J. Glaciol.*, 6(48):943–944, 1967.

[8] J. Freitag and H. Eicken. Meltwater circulation and permeability of Arctic summer sea ice derived from hydrological field experiments. *J. Glaciol.*, 49:349–358, 2003.

[9] C. H. Fritsen, V. I. Lytle, S. F. Ackley, and C. W. Sullivan. Autumn bloom of Antarctic pack-ice algae. *Science*, 266:782–784, 1994.

[10] K. Golden. Convexity and exponent inequalities for conduction near percolation. *Phys. Rev. Lett.*, 65(24):2923–2926, 1990.

[11] K. M. Golden, S. F. Ackley, and V. I. Lytle. The percolation phase transition in sea ice. *Science*, 282:2238–2241, 1998.

[12] K. M. Golden, H. Eicken, A. L. Heaton, J. Miner, D. Pringle, and J. Zhu. Thermal evolution of permeability and microstructure in sea ice. *Geophys. Res. Lett.*, 34:L16501 (6 pages and issue cover), doi:10.1029/2007GL030447, 2007.

[13] K. M. Golden, A. L. Heaton, H. Eicken, and V. I. Lytle. Void bounds for fluid transport in sea ice. *Mechanics of Materials*, 38:801–817, 2006.

[14] B. I. Halperin, S. Feng, and P. N. Sen. Differences between lattice and continuum percolation transport exponents. *Phys. Rev. Lett.*, 54(22):2391–2394, 1985.

[15] W. B. Tucker III, A. J. Gow, D. A. Meese, H. W. Bosworth, and E. Reimnitz. Physical characteristics of summer sea ice across the Arctic Ocean. *J. Geophys. Res.*, 104:1489 1504, doi:10.1029/98JC02607, 1999.

[16] M. O. Jeffries, R. A. Shaw, K. Morris, A. L. Veazey, and H. R. Krouse. Crystal structure, stable isotopes (d180), and development of sea ice in the Ross, Amundsen, and Bellingshausen Seas, Antarctica. *J. Geophys. Res.*, 99:985–995, 1994.

[17] R. P. Kusy. Influence of particle size ratio on the continuity of aggregates. *J. Appl. Phys.*, 48(12):5301–5303, 1977.

[18] R. P. Kusy and D. T. Turner. Electrical resistivity of a polymeric insulator containing segregated metallic particles. *Nature*, 229:58–59, 1971.

[19] B. Light, G. A. Maykut, , and T. C. Grenfell. Effects of temperature on the microstructure of first-year Arctic sea ice. *J. Geophys. Res.*, 108(C2):3051, 2003.

[20] M. P. Lizotte and K. R. Arrigo, editors. *Antarctic Sea Ice: Biological Processes, Interactions and Variability*. American Geophysical Union, Washington D.C., 1998.

[21] V. I. Lytle and S. F. Ackley. Heat flux through sea ice in the Western Weddell Sea: Convective and conductive transfer processes. *J. Geophys. Res.*, 101(C4):8853–8868, 1996.

[22] T. Maksym and M. O. Jeffries. A one-dimensional percolation model of flooding and snow ice formation on Antarctic sea ice. *J. Geophys. Res.*, 105(C11):26,313–26,331, 2000.

[23] T. Maksym and T. Markus. Antarctic sea ice thickness and snow-to-ice conversion from atmospheric reanalysis and passive microwave snow depth. *J. Geophys. Res.*, 113:C02S12, doi:10.1029/2006JC004085, 2008.

[24] D. K. Perovich and A. J. Gow. A quantitative description of sea ice inclusions. *J. Geophys. Res.*, 101(C8):18,327–18,343, 1996.

[25] D. K. Perovich, T. C. Grenfell, B. Light, B. C. Elder, J. Harbeck, C. Polashenski, W. B. Tucker III, and C. Stelmach. Transpolar observations of the morphological properties of Arctic sea ice. *J. Geophys. Res.*, 114:C00A04, doi:10.1029/2008JC004892, 2009.

[26] D. K. Perovich, J. A. Richter-Menge, K. F. Jones, and B. Light. Sunlight, water, and ice: Extreme Arctic sea ice melt during the summer of 2007. *Geophys. Res. Lett.*, 35:L11501, doi:10.1029/2008GL034007, 2008.

[27] D. C. Powell and T. Markus. Effects of snow depth forcing on Southern Ocean sea ice simulations. *J. Geophys. Res. C (Oceans)*, 110:C06001, doi:10.1029/2003JC002212, 2005.

[28] D. J. Pringle, J. E. Miner, H. Eicken, and K. M. Golden. Pore-space percolation in sea ice single crystals. *J. Geophys. Res. (Oceans)*, 114:C12017, 12 pp., doi:10.1029/2008JC005145, 2009.

[29] S. Rysgaard, J. Bendtsen, L. T. Pedersen, H. Ramløv, and R. N. Glud. Increased CO_2 uptake due to sea ice growth and decay in the Nordic Seas. *J. Geophys. Res.*, 114:C09011, doi:10.1029/2008JC005088, 2009.

[30] D. N. Thomas and G. S. Dieckmann, editors. *Sea Ice, 2nd Edition*. Wiley-Blackwell, Oxford, 2009.

[31] S. Torquato. *Random Heterogeneous Materials: Microstructure and Macroscopic Properties*. Springer-Verlag, New York, 2002.

[32] S. Torquato and D. C. Pham. Optimal bounds on the trapping constant and permeability of porous media. *Phys. Rev. Lett.*, 92:255505:1–4, 2004.

[33] H. J. Trodahl, M. J. McGuiness, P. J. Langhorne, K. Collins, A. E. Pantoja, I. J. Smith, and T. G. Haskell. Heat transport in McMurdo Sound first-year fast ice. *J. Geophys. Res.*, 105(C5):11347–11358, 2000.

[34] W. F. Weeks and S. F. Ackley. The growth, structure and properties of sea ice. *CRREL Monograph 82-1*, page 130 pp., 1982.

[35] A. P. Worby, Robert. Massom, and Antarctic CRC. *The Structure and Properties of Sea Ice and Snow Cover in East Antarctic Pack Ice / A.P. Worby, R.A. Massom*. Antarctic CRC Hobart, Tas, 1995.

CHAPTER 4

VARIABILITY IN THE VERTICAL CONDUCTIVITY OF GRANULAR SEA ICE

In this chapter we explore the local variability in the vertical continuity of Antarctic granular sea ice as compared to columnar sea ice. We find that the vertical conductivity of columnar changes much more continuously for brine volume fractions above 5% than granular ice. We propose this difference as a possible way to electrically determine ice type in remote sensing applications. We further discuss the reasons for the differences. The data presented were taken during SIPEX II in 2012 off of the east coast of Antarctica. Chapter 4 is a preprint with authors **Christian S. Sampson, Kenneth M. Golden, and David Lubbers.**

4.1 Abstract

The crystallographic structure of sea ice influences many of the key physical processes in the polar regions which play a major role in the Earth's climate system. There has been recent interest in using electrical methods to remotely monitor temporal variations in the ice pack to aid in improving models of these key processes. Important to these models is the crystallographic structure of the ice which is difficult to determine electrically. In September-October 2012, in conjunction with crystallographic analyses, we made direct measurements of the vertical component of the bulk conductivity of first year Antarctic sea ice as participants in the Sea Ice Physics and Ecosystem Experiment II (SIPEX II). We found higher levels of local variability in the vertical DC conductivity of granular sea ice than that of columnar sea ice. This variability is related to the differences in the way vertical connections grow in the two ice types. This work suggests that the vertical component of conductivity may be used as an aid in electrically determining the crystallographic structure of sea ice.

4.2 Introduction

The polar sea ice packs play a critical role in regulating the Earth's climate system and serve as sensitive indicators of climate change. In particular they play a major role in regulating gas exchange in the polar regions and are an important factor in determining the Earth's overall albedo. These important large scale processes depend on small scale processes with in the ice. For example, fluid flow through the porous sea ice is a major controlling component in the evolution of melt ponds, which, in turn, affects the ice pack albedo [9]. It also plays a role in brine drainage and the evolution of salinity profiles [8, 37], snow ice formation, where sea water floods the ice surface and then freezes [23], ocean ice-atmosphere CO_2 exchanges [29], convection enhanced thermal transport [21, 36], and biomass build up fueled by nutrient fluxes [6, 10, 20, 32]. Important properties such as fluid flow exhibit critical behavior which depends on the crystallographic structure of the ice. For example in columnar ice it has been shown that the ice is effectively impermeable below brine volume fractions of 5% [13] while granular ice is impermeable for brine volume fractions below about 10%, which is discussed in Chapter 3. When using small scale models to understand these processes the importance of knowing the crystallographic structure becomes paramount. Recently investigations into using DC resistivity to remotely monitor the growth and evolution of sea ice throughout a season have shown promising results [16, 19, 28]. However, most of the studies focus on columnar ice and fail to resolve ice type, with the exception of the detection of increased horizontal conductivity at the skeletal/platelet layer at the bottom of fast ice [18]. While columnar ice is the most prevalent ice type in the Arctic, although the upper 10 cm of Arctic ice is typically granular, the situation in the Antarctic is drastically different. Nearly 40% of the Antarctic ice pack is made up of granular ice, of which nearly a quarter is fine grained granular snow ice [7, 17, 23, 38], with even higher fractions is some regions [24]. Given the importance of ice type in relation to many important physical processes in the ice, it is thus important to include a method to detect ice type in any remote sensing scheme.

We view sea ice as a two phase polycrystalline composite material made up of ice and brine, with the brine phase conducting and the ice phase insulating. In this way, the conductivity of the ice depends on the connectivity the brine phase throughout the ice column and exhibits critical behavior similar to fluid flow at the 5% threshold as discussed in Chapter 2. In studies of polycrystalline composites the crystal orientation plays a major role in the properties of the given material such as electrical permittivity and conductivity [5, 14, 25]. Columnar sea ice crystals are typically oriented together with a horizontal c-axis while granular sea ice crystals are randomly oriented [2, 8, 27]. The crystal morphology has an impact on the way in which vertical connections in the pore space of sea ice form and connect. This leads to a higher variability of the electrical properties in the vertical direction for granular sea ice on small local scales. It is this variability that can be exploited to electrically detect ice type.

During September through November of 2012, we made measurements of the vertical conductivity of first year columnar and granular sea ice off the east coast of Antarctica as participants in the Australian Sea Ice Physics and Ecosystem Experiment (SIPEXII) aboard the ice breaker *Aurora Australis*. In this paper we compare those data to some established results as well as present an analysis of local scale variability of the electrical properties of granular ice which differ from that of first year columnar ice.

4.3 Methods and Measurement

In order to directly measure the vertical conductivity of the ice we employed a Wenner electrode array along 10 cm sections of our ice cores, as illustrated in Fig 4.1. This method is similar to that outlined in Chapter 2. To make the measurement we used a AEMC DC resistivity meter. To facilitate the measurement, full length ice cores were extracted and holes were first drilled into the cores at 10 cm intervals and temperature probes inserted along the core. Next, slightly larger diameter holes were drilled into the previous temperature probe holes with tight fitting nails inserted and used as electrodes for the Wenner array. The nails were slightly larger then the holes to ensure a good electrical connection with the ice. With a 10 cm spacing between electrodes, current was injected by the outer probes and the potential difference measured at the inner two. This gave the resistance for the 10 cm section of the ice between the innermost probes. The cores were then bagged and rushed into a $-22C^{\circ}$ crystallography lab on board the *Aurora* for later analysis. In the lab the cores were cut into 10 cm sections at the measurement holes. Vertical thin sections were then cut from the center of those sections and placed between two cross-polarizing films showing the crystal structures of the corresponding to the resistance measurements. The outer halves of the sections were bagged and melted for bulk salinity measurements. The crystallography lab was cold enough to completely freeze the cores to minimize brine leakage. The temperature$(T)C^{\circ}$ and bulk salinity $(S)PSU$ can then be used to calculate the brine volume fraction ϕ corresponding to the resistance measurement using the Frankenstein-Garner relation shown in equation 4.1.

$$\phi = \frac{S}{1000}\left(\frac{49.185}{|T|} + 0.532\right) \tag{4.1}$$

The vertical conductivity of a 10 cm section can be found using the measured resistance R. The vertical resistivity ρ_v and corresponding conductivity σ_v are obtained via $\rho_v = AR/L$, $\sigma_v = 1/\rho_v$ where A is the cross sectional area and L the length.

4.4 Theory

Here we review some theory on the growth of granular and columnar sea ice as well as percolation theory and Archie's law, which can be used to model the conductivity of porous materials as a function of brine volume fraction.

4.4.1 Conductivity in Columnar and Granular Ice

As sea water begins to freeze the first ice crystals to form create a slush referred to as frazil ice. As this slush freezes granular ice forms which has crystals with random c-axis orientations that trap brine in between them. As further growth progresses, crystals which have their c-axes aligned in the horizontal plane grow downward leading to the formation of vertical columns of ice, dubbed columnar ice. An example of this ice can be seen in Figure 4.1a. In this type of ice, brine inclusions form between the subgrains of the ice aligned with the growth directions of the crystals [8]. At low temperatures the brine inclusions are smaller and isolated from each other. As the sea ice warms they begin to connect up forming long vertical pathways within the ice [8, 13]. This vertical alignment leads to anisotropy in the conductivities of the ice as current flows preferentially along the elongated brine inclusions yielding an increased vertical conductivity. In addition, sea ice is typically transversely isotropic [28, 30] yielding the same conductivities in all horizontal directions. The electrical anisotropy in transversely isotropic materials like sea ice can be quantified using the factor of anisotropy defined as $f = \sqrt{\sigma_h/\sigma_v}$ [22, 28]. One can quantify the level of crystallographic anisotropy using the crystal anisotropy factor. This is defined as $A = \Sigma C_v/\Sigma C_h$, where C_v and C_h are the size of the vertical and horizontal projections of each individual c-axis measurement from a thin section. For both parameters a value of 1 indicates isotropy while $A = 0$ indicates that all c -axes lie in the horizontal plane. Examples of values of A are $A = 0.23$ and 0.14 for columnar ice and $A = 0.67$ for platelet ice [18]. Typical values of f range from 0.2 to 0.7 with the higher values possibly indicating granular ice [28, 30].

In contrast to columnar ice, granular frazil and granular snow ice are comprised of crystals with isotropically distributed c-axes which trap the conductive brine between them. Given its structure one might expect granular ice to have an isotropic bulk conductivity. However this is not the case. The conductivity in the vertical direction remains larger and does not differ much from that of columnar ice. This may suggest that anisotropic secondary pores (such as brine tubes and channels which form as the ice warms and gravity pulls the brine down) control the resistivity structure rather then the isotropic primary pore space [19]. This is consistent with our findings as well as we see no clear difference in the over all vertical conductivities of our granular and columnar measurements as a whole. However, the horizontal conductivity of granular ice is typically higher. This has been observed in [18] using cross-borehole tomography to measure the horizontal and vertical conductivities of first year Antarctic sea ice. They found increased horizontal conductivities near the upper granular layer of the ice as well as near the bottom platelet layers. This was attributed to a larger number of horizontal connections that result from the more random crystal structure of the ice [18]. They were also able to show that as crystallographic anisotropy A increased, the factor of electrical anisotropy f increased as well. This implies that as the crystal structure of the ice becomes more isotropic, the bulk conductivity does too.

4.4.2 Thermal Evolution of Columnar and Granular Ice

Given the electrical anisotropy of sea ice, and the apparent control of its resistivity structure by the connectivity of the brine inclusions, it is important to understand how these structures evolve with increases in temperature and porosity. In particular, we are interested in the how vertical connectivity of the pore space changes as it is the controlling factor in the vertical conductivity of sea ice.

The evolution of connectivity in columnar ice has received more attention than that of granular ice [8, 13]. However, it is clear in these studies that as the temperature of columnar sea ice increases, and thus porosity, the pore space connections that form are oriented primarily in the vertical direction and reside between the vertically aligned columnar ice crystals. It is only at high brine volume fractions that more complicated geometry is observed. In an NMR study [3] of the thermal evolution of pore space connectivity of samples of winter columnar and granular sea ice taken near Barrow Alaska, it was observed that the connections which formed in the granular samples, as temperature was increased, had a more complex morphology with a combination of horizontal and vertical connections. Those of the columnar sea ice were primarily vertical and constrained within the lamaller plane of the columnar ice crystals. This difference in the evolution of connectivity has implications for the behavior of the vertical conductivity of a localized region of granular or columnar sea ice. We see evidence of this in our thin sections as well, illustrated in Figure 4.2. The two granular sections in the figure are from core 99 and have brine volume fractions of $\phi = 0.834$ and $\phi = 0.836$ but differ with vertical formation factors, defined as the ratio of the conductivity of the ice to that the brine, of $F_v = 0.02$ and $F_v = 0.011$, respectively. The higher vertical conductivity corresponds to the sample with the elongated vertical connection. In [13] it was observed that the fractional connectivity, defined as the proportion of inclusions at the upper surface which are also connected to the lower surface, for a cylindrical sample of lab grown columnar sea ice increased linearly with increasing porosity for brine volume fractions above $\phi_c = 5\%$. While no similar data for granular ice were found, we would expect different behavior. Due to the random distribution of the c-axes of the ice crystals in granular ice, there is less to constrain the direction of the pore space expansion with an increase temperature. This would imply a variety of levels of vertical connectivity for a given brine volume fraction in granular ice and thus a wider variation in values of vertical conductivity.

4.4.3 Percolation Theory and Critical Behavior

Percolation theory for both lattice and continuum models applies to materials where the connectedness of one phase dominates the effective behavior of the material as a whole.

In sea ice it is the connectedness of the brine phase which dominates the effective electrical properties of the ice as a whole.

Consider the infinite square ($d = 2$) or cubic ($d = 3$) network of bonds joining nearest neighbor sites on the integer lattice $\mathbb{Z}^d$. The bonds are assigned conductivities of $\sigma_0 > 0$ (open) or 0 (closed) with probabilities p and $1 - p$, respectively. There is a critical probability p_c called the *percolation threshold* where an infinite, connected set of open bonds first appears. In $d = 2$ $p_c = 1/2$ and in $d = 3$ $p_c \approx 1/4$. Let $\sigma(p)$ be the conductivity of this random network of bonds in the vertical direction. For $p < p_c$, $\sigma(p) = 0$. For $p > p_c$, near the threshold $\sigma(p)$ exhibits power law behavior,

$$\sigma(p) \sim \sigma_0 (p - p_c)^t \quad as \quad p \to p_c^+, \tag{4.2}$$

where t is the conductivity critical exponent. In $d = 3$, it is believed that $t \approx 2$ [34, 35] and there is a rigorous bound [11] that $t \leq 2$.

In Chapter 2 it was shown that the vertical conductivity of columnar sea ice exhibits critical behavior at a critical brine volume fraction $\phi_c \approx 5\%$. This corresponds to the volume fraction in the *rule of fives* [12] where the brine channels first begin to connect on large scales. Below this percolation threshold the vertical conductivity, while not zero, shows slow growth while after this threshold, when the brine phase begins to connect on a large scale, the conductivity increases very rapidly and can be modeled with percolation theory according to the equation

$$F_v(\phi) = F_0(\phi - 0.05)^2 = 9(\phi - 0.05)^2, \tag{4.3}$$

where $F_v(\phi) = \frac{\sigma_v}{\sigma_b}$ is the vertical formation factor defined as the ratio of the vertical conductivity σ_v and the conductivity of the brine σ_b. The conductivity of the brine can be calculated from the temperature T via [31]

$$\sigma_b = -T \exp(0.5193 + .08755T) \;\; \Omega^{-1} m^{-1}, \quad T \geq -22.9°C. \tag{4.4}$$

The scaling factor F_0 is estimated in Chapter 2 and falls in a range of $6 \leq F_0 \leq 24$ for columnar ice via critical path analysis. The factor $F_0 = 9$ comes from a statistical best fit of vertical conductivity data from the SIPEX I cruse in 2007.

4.4.4 Archie's Law

Archie's law [1] is an empirical equation relating the bulk conductivity σ^* of a porous medium to its porosity and the conductivity σ_f of the fluid occupying the pore space,

$$\sigma^* = a\sigma_f\phi^m. \tag{4.5}$$

In this relation ϕ is the relative volume fraction of the fluid volume, or porosity, and a is a scaling factor often taken to be 1, which yields the correct limiting behavior as $\phi \to 1$. The exponent m depends on the geometry of the solid phase of the porous medium, such as the shape of the grains in porous rock or sand.

While percolation theory describes conductivities well for $\phi > 5\%$, Archie's Law is useful as it can describe the conductivity for systems with connectivity all the way down to $\phi = 0$. For our purpose we take $\sigma^* = \sigma_v$, $\sigma_w = \sigma_b$ and ϕ to be the brine volume fraction of the ice. We can then look at the vertical formation factor

$$F_v = \frac{\sigma_v}{\sigma_b} = a\phi^m, \tag{4.6}$$

where σ_b depends on temperature via equation 4.4. Arcie's law has been employed to model the conductivity of ice successfully by many others [4, 19, 28, 33]. These previous results find a relatively wide range of exponents $m = 1.5 - 2.88$ for the conductivity of the ice and were measured indirectly. In [28] it was found that $m = 1.75$ was appropriate for the vertical component of the conductivity σ_v. When analyzing our data set as a whole we find good agreement with the exponent $m = 1.75$ using statistical best fits and enforcing a condition of $a = 1$. However when a is allowed to be determined by the data we obtain $F_v = .36\phi^{1.38}$; the values for a and m remain close for both the granular and columnar sets when analyzed separately.

One of the underlying assumptions in Archie's Law is that porosity and connectivity vary continuously together. If we wish to apply Archie's Law to the vertical conductivity of sea ice, we must assume that small changes in porosity will give rise to small changes in vertical connectivity. This is certainly true in columnar ice, for $\phi > 0.05$, due to the preferential alignment of the crystals and linear growth of fractional connectivity mentioned above. However, in granular ice, in particular fine grained granular ice, where the crystal c-axes are isotropically distributed, small changes in porosity may lead to increases in horizontal connectivity rather then simply vertical connectivity. Depending on how the crystals are distributed one would expect a larger variation in the vertical formation factor of granular ice at a given brine volume fraction. Indeed, when considering the vertical fluid permeability of granular ice in Chapter 3, we see that the ice is effectively impermeable for brine volume fraction below $\phi_c \approx 10\%$. In contrast, in [13] it is shown that columnar ice becomes vertically permeable at a lower critical volume fraction of $\phi_c \approx 5\%$. This illustrates that vertical connections grow more slowly in granular ice than columnar as brine volume increases. That is to say, there is only a large enough number of vertical connections for fluid flow at highly connected states. For these reasons, we expect that granular ice will show more variation in F_v with brine volume fraction on the local scale than columnar ice. We also expect to see less of a power law behavior at the local scale.

4.5 Comparison to Established Results

In this section we will simply compare our data to established results. In relation to Archie's Law for the vertical formation factor $F_v = \phi^m$, we performed statistical best fits on our data sets separated by ice type as well as the combined data set. We performed fits forcing the scaling parameter $a = 1$ and obtained $m = 1.76$ for our granular ice and $m = 1.71$ for columnar ice. When combining the data sets we obtain $m = 1.75$. These results are in close agreement with the value of $m = 1.75$ measured for the vertical conductivity and assumed by others [15, 26, 28].

When considering percolation theory, it is useful to instead look at the vertical resistivity factor, $R_v = 1/F_v$. With our formula in equation (4.3) we obtain

$$R_v = \frac{1}{F_0(\phi - 0.05)^2}. \tag{4.7}$$

As a result, we would expect to see divergent behavior at $\phi \approx 0.05$, and indeed we do for both crystal structures as illustrated in Figure 4.3. Both ice types appear to have the same critical threshold for vertical DC conductivity at $\phi \approx 0.05$, which does not allow us to use the critical behavior to determine the ice type. It should be noted that we see a slower rate of divergence at the critical threshold of $\phi \approx 0.05$ in our data from SIPEX II than that compared to SIPEX I. While the reason for this is not clear, the columnar ice during SIPEX I was young, thin (30-60cm), and much less disturbed from its initial formation. In contrast, the columnar ice measured during SIPEX II came from much thicker (1.2-2.5m), relatively older ice, often a part of rafted ice. As a result small deformations in the columnar structure may lead to *average* electrical behavior more like that of granular ice as vertical connections between ice crystals would not be as disjoint as in undeformed columnar sea ice.

4.5.1 Local Variability

As discussed above, we expect to see larger variability in the vertical formation factor F_v on local scales in granular ice than in columnar ice. In fact this is what see when comparing F_v vs ϕ on a core by core basis. Examples of these data are summarized in Figure 4.4. For samples of columnar ice it is apparent that F_v varies continuously with ϕ with the exception of 1 data point in cores 50 and 51, which incidentally occurs at the cusp of the typical c-curve of salinity vs depth. For the samples of granular ice, no clear relationship is immediately apparent. In core 98, for example, there are 5 data points with $\phi \approx 8\%$ which take on different values of F_v, between $F_v = 0.01$ and $F_v = 0.024$, more than doubling the conductivity. This is presumed to be a result of differences in vertical connectivity at the same brine volume fraction in granular ice.

In order to quantify the variabilities we assume a power law behavior in accordance with Archie's Law (equation 4.6) and perform linear best fits of the linearized log-log data. In the first set of fits we do not assume $a = 1$ as a way to test for local linear dependence. The results are summarized in Table 4.1. When comparing the R^2 statistics for the columnar vs granular samples, we see higher values for columnar ice than for granular ice, indicating a higher likelihood of linear correlation. In the columnar samples R^2 ranges from $R^2 = 0.43$ to $R^2 = 0.92$ while the range for the granular samples is $R^2 = 0.014$ to $R^2 = 0.28$ with only 3 of the 7 above $R^2 = 0.05$. Core 54 was a mix of mostly columnar and some large grain granular ice and also shows strong correlation with an R^2 value of 0.74. We would expect columnar ice to be the controlling factor in a mixed sample as it should be the vertical connections which dominate the behavior of F_v.

When comparing the P-values for slope of columnar vs granular ice, we see much lower P-values for columnar ice than for granular ice. In this case a low P-value implies a rejection of the null hypothesis of no correlation, while a high P-value implies a lack of linear correlation. Typically, a P-value above $P = 0.5$ is considered grounds to accept the null hypothesis of no correlation. In the columnar samples all of the P-values fall below this threshold with values ranging from $P = 0.008$ to $P = 0.15$ for the slopes while in the granular ice 4 of the 7 cores have P-values above 0.7, with the other 3 ranging from $P = 0.21$ to $P = 0.35$. When comparing the standard errors of the slope for the two data sets, we find that the columnar samples vary less from the model than granular samples with standard errors varying from $S = 0.30$ to $S = 0.88$. The range for granular samples is $S = .87$ to $S = 2.12$. All of these statistics point to a higher variation in the vertical conductivity of granular sea ice in a local region.

Assuming Archie's Law with $m = 1.75$ and $a = 1$ is a good model for the vertical conductivity, we would expect to obtain a linear fit with a slope close to the exponent 1.75 and intercept close to zero. For our columnar ice samples we obtain Archie exponents ranging from $m = 1.56$ to $m = 1.90$ and y intercepts ranging from $b = -0.24$ to $b = 0.25$ corresponding to range of scaling factors of $a = 0.60$ to $a = 1.80$. In the granular ice samples we see drastically different results with exponents ranging from $m = 0.43$ to $m = 2.99$ with 5 of the 7 all less than 1. The y intercepts range from $b = -2.60$ to $b = 1.57$ with 6 of the 7 having magnitude larger than 1. This corresponds to a range of scaling factors of $a = 0.003$ to $a = 37.2$. However, as shown in Figure 4.3 we find that for the data set as a whole, both columnar and granular ice are well represented by the model $F_v = \phi^{1.75}$ for $\phi > 0.05$. It is thus useful to repeat our analysis of the log-log linearized data forcing the scaling factor to be $a = 1$. The results are summarized in Table 4.2. When we do this, we see excellent agreement with the model for both ice types suggesting that, on average, Archie's Law is indeed applicable.

4.6 Conclusion

In all, over 81 direct measurements of the DC vertical conductivity of Antarctic sea ice were made and matched to their crystallographic structure. The measurements compare well to a number of established results [18, 19, 28] . While no detectable difference in the vertical conductivity was found between the ice types on average, a higher degree of local variability of the vertical formation factor F_v was found in granular ice. This is most likely related to the effect the crystallographic structure has on the way in which vertical connections form in the pore spaces of the two ice types. This implies that measurements of F_v could be used to distinguish between ice types. This is paramount when considering the remote monitoring of sea ice throughout a season. The vertical fluid permeability in particular is sensitive to crystallographic structure and exhibits different critical behavior depending on the ice type. Columnar ice is effectively impermeable for brine volume fractions below $\phi_c \approx 5\%$ [13] while for granular ice there is a critical threshold of closer to $\phi_c \approx 10\%$. This has severe implications for the biological and physical processes in the ice and thus any models used to understand them. This makes a determination of the crystal structure extremely important. This work demonstrates that that the vertical component of the bulk conductivity could be used to aid in the determination of crystallographic structure of sea ice using electrical methods.

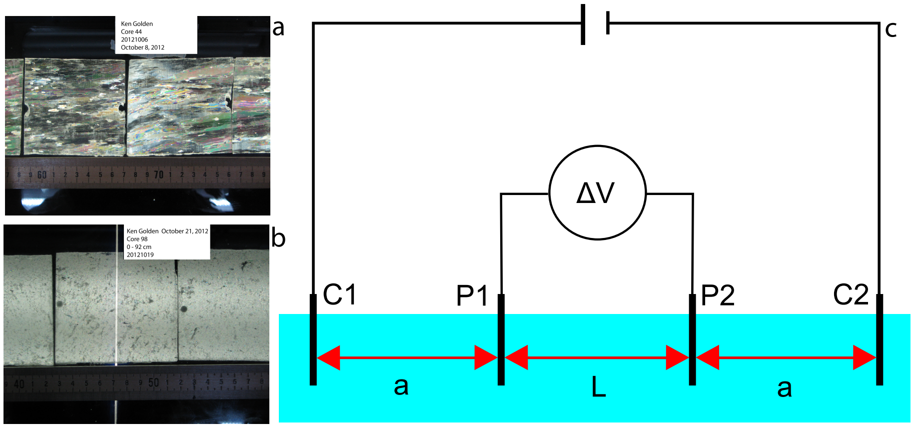

Figure 4.1: Images of columnar and granular crystallographic samples corresponding to the 10 cm measured sections and a diagram of our measurement method. In (a) we show columnar ice and in (b) we show granular. Resistivity measurements were made between the holes in the thin sections. In (c) we show a schematic of the Wenner array setup used to measure the vertical component of the ice core. The measurement corresponds to the length L between P1 and P2.

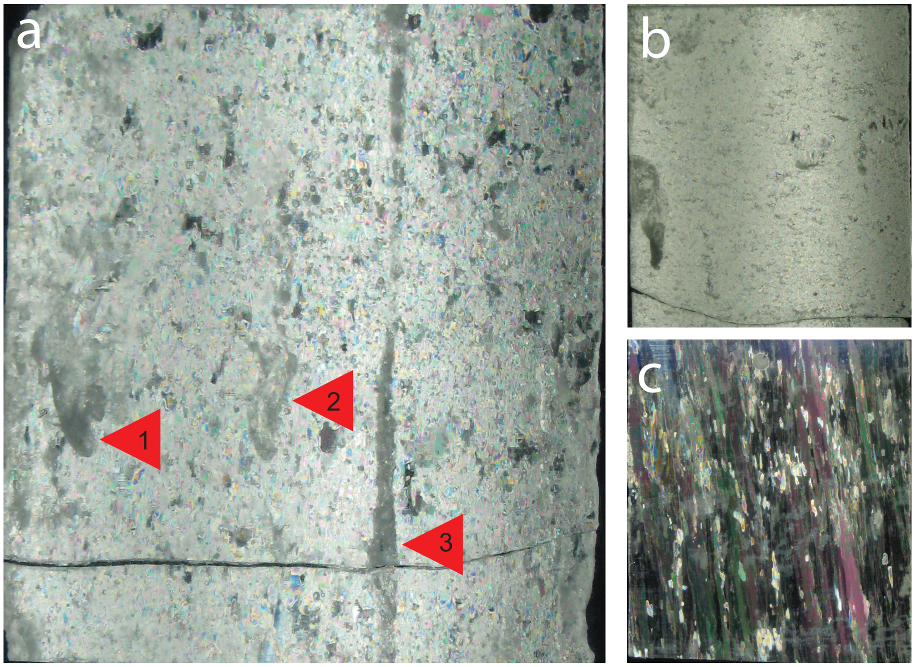

Figure 4.2: A comparison of the morphologies of columnar and granular sea ice. (a) 10 cm section of granular ice from Core 99. Arrows 1 and 2 indicate pore spaces with complex morphology while arrow 3 shows a vertical connection which acts as the primary control of the resistivity structure. A 10 cm section of granular ice (b) from core 99 with a similar brine volume fraction to the section shown in A, but with little to no vertical connectivity. A 10 cm section of columnar ice (c) from Core 44 showing the vertical alignment of the pore spaces between columnar crystals.

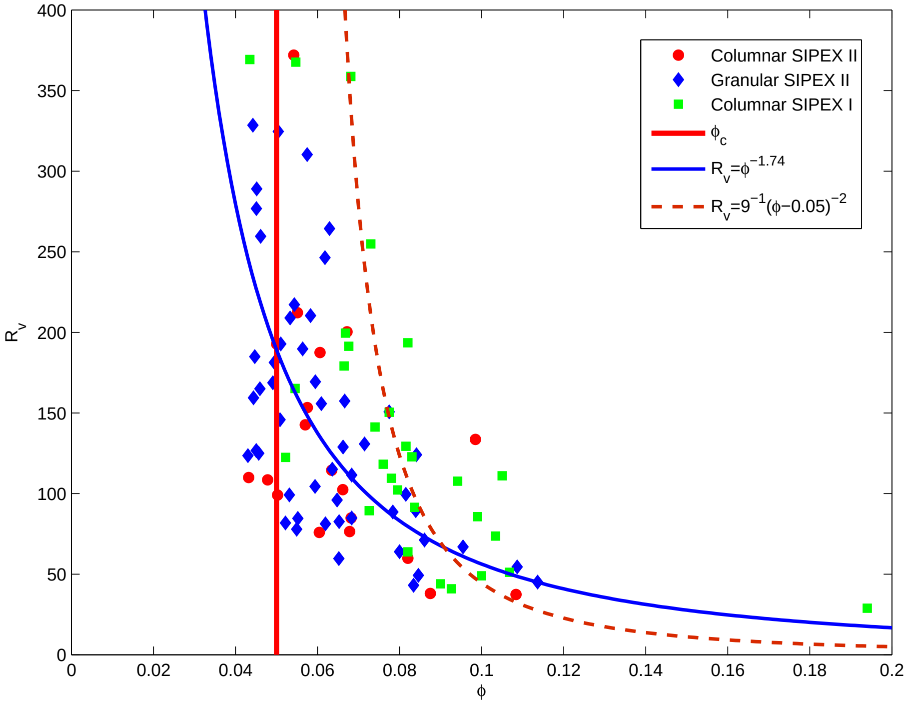

Figure 4.3: Here we display all of our granular and columnar data in comparison with predictions of the vertical resistivity factor R_v coming from Archie's law with $m = 1.75$ (solid curve) and Percolation Theory (dashed curve). Diamonds represent granular ice, circles columnar ice from SIPEX II and squares columnar ice from SIPEX I in 2007. We note divergent behavior at $\phi \approx 0.05$ where we see departure from Archie's law.

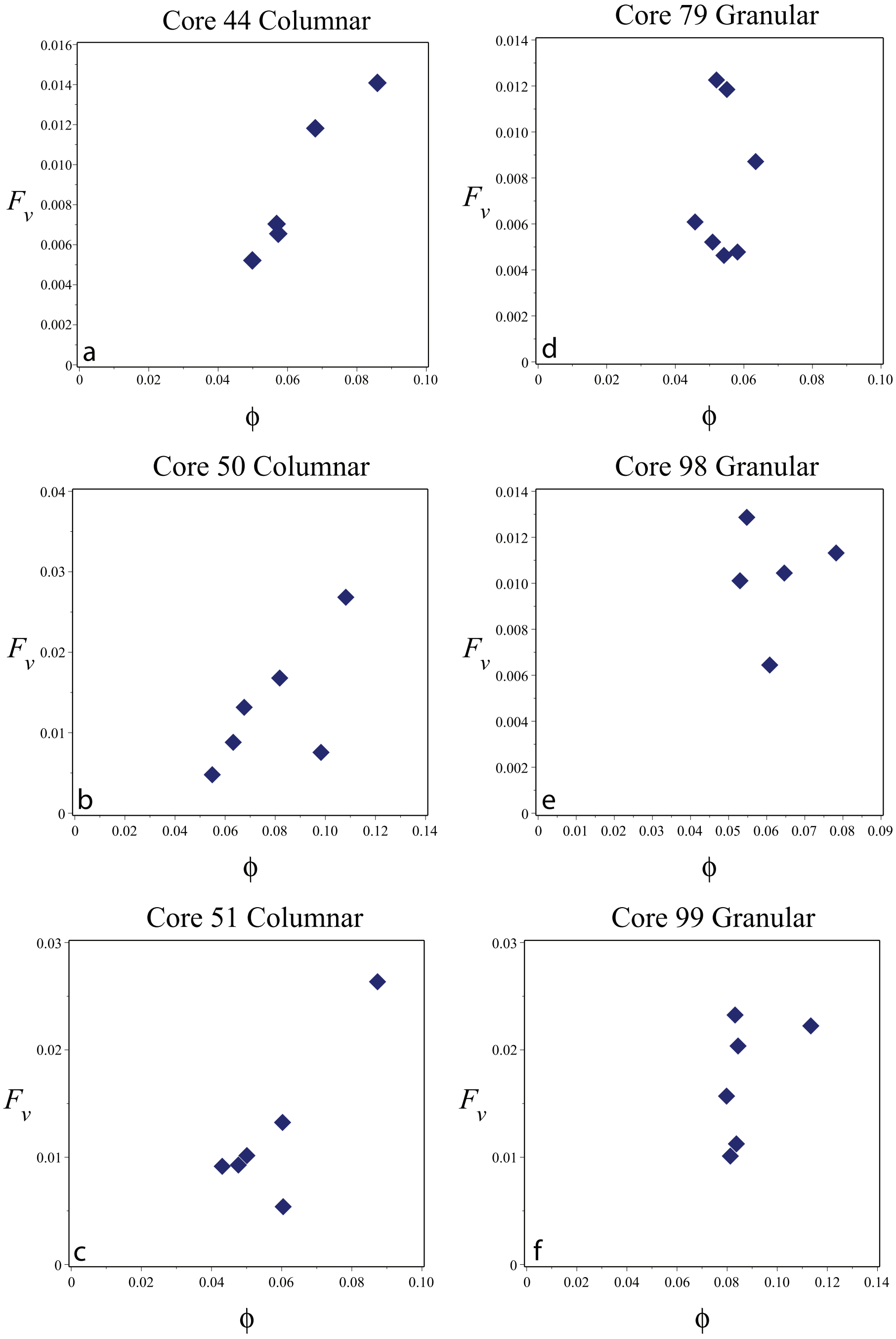

Figure 4.4: Several examples of the differences in the behavior of the conductivity of sea ice as a function of brine volume fraction between columnar and granular sea ice. In (a),(b), and (c) we show three plots from Cores 44, 50, 51 of F_v vs ϕ for columnar ice displaying continuous behavior. In (d),(e), and (f) we show three plots of Cores 77, 79, 99 displaying high variability for similar brine volume fractions

Table 4.1: Here we present the results of the linear regression analysis where the scaling factor *a* in Archie's Law was allowed to be chosen by the data. We see strong linear correlation and less variability in columnar ice than in granular ice.

Core	Ice Type	R^2	Slope	Std. Error	P-value	Intercept	Std. Error	P-Value
44	Col	0.92	1.90	0.3	0.008	0.25	0.37	0.54
50	Col	0.44	1.56	0.88	0.14	-0.21	0.98	0.83
51	Col	0.43	1.38	0.8	0.15	-0.24	0.99	0.82
54	Mix	0.74	2.41	0.58	0.006	0.65	0.72	0.39
69	Gra	0.02	0.43	1.42	0.71	-1.65	1.12	0.28
75	Gra	0.05	-0.36	0.96	0.78	-2.60	1.26	0.18
77	Gra	0.28	2.99	2.12	0.21	1.57	2.60	0.57
79	Gra	0.018	0.55	1.81	0.77	1.40	2.30	0.50
98	Gra	0.014	0.07	0.97	0.95	-1.90	1.19	0.20
99	Gra	0.22	01.20	1.28	0.35	-0.44	1.28	0.70
108	Gra	0.17	0.96	0.87	0.31	-1.02	1.10	0.39

Table 4.2: Here we present the results of the linear regression analysis with the scaling factor $a = 1$ for Archie's law. In this case we see strong correlation in both columnar and granular data.

Core	Ice Type	R^2	Slope	Std. Error	P-value
44	Col	0.999	1.73	0.02	9×10^{-8}
50	Col	0.995	1.75	0.07	2×10^{-6}
51	Col	0.990	1.57	0.06	1×10^{-6}
54	Col	0.990	1.88	0.02	4×10^{-11}
69	Gra	0.990	1.75	0.06	2×10^{-8}
75	Gra	0.997	1.69	0.05	6×10^{-5}
79	Gra	0.993	1.69	0.06	8×10^{-8}
98	Gra	0.995	1.65	0.06	8×10^{-6}
99	Gra	0.994	1.68	0.05	6×10^{-7}
108	Gra	0.996	1.76	0.06	6×10^{-9}

4.7 References

[1] G. E. Archie. The electrical resistivity log as an aid in determining some reservoir characteristics. *Trans. Am. Inst. Min. Metal. Petrol. Eng.*, 146:54–64, 1942.

[2] U. Bleil and J. Thiede. *Geological History of the Polar Oceans: Arctic vs Antarctic*. Kluwer Academic Publishers, P.O Box 17, 3330 AA Dordrecht, The Netherlands, 1990.

[3] C. Bock and H. Eicken. A magnetic resonance study of temperature-dependent microstructural evolution and self-diffusion of water in Arctic first-year sea ice. *Ann. Glaciol.*, 40:179–184, 2005.

[4] R. G. Buckley, M. P. Staines, and W. H. Robinson. In situ measurements of the resistivity of Antarctic sea ice. *Cold Reg. Sci. Technol.*, 12(3):285–290, 1986.

[5] A. Cherkaev. *Variational Methods for Structural Optimization*. New York: Springer-Verlag, Cambridge, 2000.

[6] H. Eicken. The role of sea ice in structuring Antarctic ecosystems. *Polar Biol.*, 12:3–13, 1992.

[7] H. Eicken. Factors determining microstructure, salinity and stable-isotope composition of antarctic sea ice: Deriving modes and rates of ice growth in the Weddell Sea. *AGU Antarctic Research Series*, 74, 1998.

[8] H. Eicken. Growth, microstructure and properties of sea ice. In D. N. Thomas and G. S. Dieckmann, editors, *Sea Ice: An Introduction to its Physics, Chemistry, Biology and Geology*, pages 22–81. Blackwell, Oxford, 2003.

[9] H. Eicken, T. C. Grenfell, D. K. Perovich, J. A. Richter-Menge, and K. Frey. Hydraulic controls of summer Arctic pack ice albedo. *J. Geophys. Res. (Oceans)*, 109(C18):C08007.1–C08007.12, 2004.

[10] C. H. Fritsen, V. I. Lytle, S. F. Ackley, and C. W. Sullivan. Autumn bloom of Antarctic pack-ice algae. *Science*, 266:782–784, 1994.

[11] K. Golden. Convexity and exponent inequalities for conduction near percolation. *Phys. Rev. Lett.*, 65(24):2923–2926, 1990.

[12] K. M. Golden, S. F. Ackley, and V. I. Lytle. The percolation phase transition in sea ice. *Science*, 282:2238–2241, 1998.

[13] K. M. Golden, H. Eicken, A. L. Heaton, J. Miner, D. Pringle, and J. Zhu. Thermal evolution of permeability and microstructure in sea ice. *Geophys. Res. Lett.*, 34:L16501 (6 pages and issue cover), doi:10.1029/2007GL030447, 2007.

[14] A. Gully, J. Lin, E. Cherkaev, and K.M. Golden. Bounds on the complex permittivity of polycrystalline composites by analytic continuation. *Proceedings of The Royal Society A*, 2014.

[15] C. Haas, S. Gerland, H. Eicken, and H. Miller. Comparison of sea-ice thickness measurements under summer and winter conditions in the Arctic using a small electromagnetic induction device. *Geophysics*, 62:749–757, 1997.

[16] C. Haas, M. Nicolaus, S. Willmes, A. Worby, and D. Flinspach. Sea ice and snow thickness and physical properties of an ice floe in the western Weddell Sea and their changes during spring warming. *Deep Sea Research II*, 55:936–974, 2008.

[17] M. O. Jeffries, R.A. Shaw, K. Morris, A. L. V., and H.R. Krouse. Crystal structure, stable isotopes (d18o), and development of sea ice in the Ross, Amundsen, and Bellingshausen Seas, Antarctica. *Cold Regions Science and Technology*, 99, 1994.

[18] K. A. Jones, A. J. Gough, M. Ingham, A.M. Mahoney, P.J. Langhorne, and T. G. Haskell. Detection of differences in sea ice crystal structure using cross-borehole dc resistivity tomography. *Cold Regions Science and Technology*, 78:40–45, 2012.

[19] K. A. Jones, M. Ingham, D. J. Pringle, and H. Eicken. Temporal variations in sea ice resistivity: Resolving anisotropic microstructure through cross-borehole dc resistivity tomography. *J. Geophys. Res.*, 115:C11023, doi:10.1029/2009JC006049, 2010.

[20] M. P. Lizotte and K. R. Arrigo, editors. *Antarctic Sea Ice: Biological Processes, Interactions and Variability*. American Geophysical Union, Washington D.C., 1998.

[21] V. I. Lytle and S. F. Ackley. Heat flux through sea ice in the Western Weddell Sea: Convective and conductive transfer processes. *J. Geophys. Res.*, 101(C4):8853–8868, 1996.

[22] R. Maillet. The fundamental equations of the electrical prospecting. *Geophysics*, 12(4):529–556, 1947.

[23] T. Maksym and M. O. Jeffries. A one-dimensional percolation model of flooding and snow ice formation on Antarctic sea ice. *J. Geophys. Res.*, 105(C11):26,313–26,331, 2000.

[24] T. Maksym and T. Markus. Antarctic sea ice thickness and snow-to-ice conversion from atmospheric reanalysis and passive microwave snow depth. *J. Geophys. Res.*, 113:C02S12, doi:10.1029/2006JC004085, 2008.

[25] G. W. Milton. *Theory of Composites*. Cambridge University Press, Cambridge, 2002.

[26] R. M. Morey, A. Kovacs, and G.F.N Cox. Electromagnetic properties of sea ice. *Cold Reg. Sci. Technol.*, 9:53–75, 1984.

[27] A. Omstedt. An investigation of the crystal structure of sea ice in the Bothnian Bay. Technical Report, Swedish Administration of Shipping and Navigation, 1985.

[28] J.E. Reid, A. Pfaffling, A.P. Worby, and J.R. Bishop. In situ measurements of the direct-current conductivity of antarctic sea ice: Implications for airborne electromagnetic sounding of sea-ice thickness. *Annals of Glaciology*, 54:217–223, 2006.

[29] S. Rysgaard, J. Bendtsen, L. T. Pedersen, H. Ramløv, and R. N. Glud. Increased CO_2 uptake due to sea ice growth and decay in the Nordic Seas. *J. Geophys. Res.*, 114:C09011, doi:10.1029/2008JC005088, 2009.

[30] C. Sampson, K. M. Golden, A. Gully, and A. P. Worby. Surface impedance tomography for Antarctic sea ice. *Deep Sea Res. II*, 58:1149–1157, 2011.

[31] A. Stogryn and G. J. Desargant. The dielectric properties of brine in sea ice at microwave frequencies. *IEEE Trans. Antennas Propagat.*, AP-33(5):523–532, 1985.

[32] D. N. Thomas and G. S. Dieckmann, editors. *Sea Ice, Second Edition*. Wiley-Blackwell, Oxford, 2009.

[33] F. Thyssen, H. Kohnen, M.V. Cowan, and G. W. Timco. Dc resistivity measurements on the sea ice near Point Inlet, n.w.t. (Baffin Island). *Polarforschung*, 44:117–126, 1974.

[34] S. Torquato. *Random Heterogeneous Materials: Microstructure and Macroscopic Properties*. Springer-Verlag, New York, 2002.

[35] S. Torquato and D. C. Pham. Optimal bounds on the trapping constant and permeability of porous media. *Phys. Rev. Lett.*, 92:255505:1–4, 2004.

[36] H. J. Trodahl, M. J. McGuiness, P. J. Langhorne, K. Collins, A. E. Pantoja, I. J. Smith, and T. G. Haskell. Heat transport in McMurdo Sound first-year fast ice. *J. Geophys. Res.*, 105(C5):11347–11358, 2000.

[37] W. F. Weeks and S. F. Ackley. The growth, structure and properties of sea ice. *CRREL Monograph 82-1*, page 130 pp., 1982.

[38] A. P. Worby and R. A. Massom. The structure and properties of sea ice and snow cover in east antarctic pack ice. *Res. Rep*, 1995.

CHAPTER 5

A NETWORK MODEL FOR ELECTRICAL TRANSPORT IN SEA ICE

In this chapter we explore a network model for electrical transport in sea ice based on statistical measurements of the brine microstructure. Particularly we consider a log-normal distribution describing the temperature dependence of the inclusion sizes, and connectivity information obtained from X-ray CT data. The numerical model agrees well with field data taken on SIPEX I in 2007 and could be use to aid in thickness measurements derived from electromagnetic measurements. Chapter 5 is a reprint originally published in *Physica B.*, **405** (2010) 3033-3036 with authors **Jingyi Zhu, Kenneth M. Golden, Adam Gully, and Christian S. Sampson.** It is reproduced here with permission of the publisher.

Physica B 405 (2010) 3033–3036

Contents lists available at ScienceDirect

Physica B

journal homepage: www.elsevier.com/locate/physb

A network model for electrical transport in sea ice

J. Zhu, K.M. Golden *, A. Gully, C. Sampson

University of Utah, Department of Mathematics, 155 S 1400 E RM 233, Salt Lake City, UT 84112-0090, USA

ARTICLE INFO

Keywords:
Sea ice
Electrical conductivity
Network model
Sea ice thickness

ABSTRACT

Monitoring the thickness of sea ice is an important tool in assessing the impact of global warming on Earth's polar regions, and most methods of measuring ice thickness depend on detailed knowledge of its electrical properties. We develop a network model for the electrical conductivity of sea ice, which incorporates statistical measurements of the brine microstructure. The numerical simulations are in close agreement with direct measurements we made in Antarctica on the vertical conductivity of first year sea ice.

1. Introduction

Sea ice is a critical component of Earth's climate system as well as a sensitive indicator of climate change. Determining the thickness distribution of the polar sea ice packs is a central problem in monitoring the impact of global warming. However, there is significant uncertainty in our knowledge of the ice thickness distribution and how it is changing. Not only does this uncertainty affect assessments of how the changing climate is impacting the polar regions, but it also affects predictions of global climate models, where accurate knowledge of sea ice initial conditions is essential for long term simulations.

Most methods of measuring sea ice thickness, and interpretation of the data obtained, depend on detailed knowledge of the electrical properties of the ice. Since sea ice is a composite of pure ice with brine inclusions [21,3], whose volume fraction and geometry depend strongly on temperature, understanding its electrical properties is a challenging problem in the theory of inhomogeneous materials. While the electrical conductivity of pure ice is negligible for most purposes, the electrical conductivity of brine can be substantial. Here we develop a network model for the electrical conductivity of sea ice, and compare the results with direct measurements of the vertical conductivity of first year sea ice we made during the 2007 Sea Ice Physics and Ecosystem eXperiment (SIPEX) expedition off the coast of East Antarctica, from the Australian icebreaker *Aurora Australis* [9].

Early DC resistivity measurements on sea ice were aimed at determining ice thickness [5,19,20]. Initially all these studies employed surface soundings using 4 electrodes in either the Wenner or Schlumberger configurations, although Thyssen et al. [19] later used vertically arranged electrodes in the side of an ice pit. Later measurements in the Antarctic were also reported [2]. The anisotropic nature of the resistivity of sea ice, due to the preferential vertical alignment and connectivity of brine pores, leads to such measurements significantly underestimating the ice thickness.

More promising determinations of sea ice thickness have been achieved using low frequency electromagnetic (EM) techniques [14,11,13,22,17]. The technique relies on a time varying primary magnetic field (generated by a transmitter coil) inducing eddy currents in the seawater beneath the comparatively resistive ice. The secondary magnetic field produced is sensed by a receiver coil, determining an apparent conductivity which results essentially from an integration over the vertical distance between the instrument and induced currents. The thickness is found using empirical relationships [12], with good results for smooth ice and underestimates near ridges [12]. The technique is adaptable to continuous measurements being made either from a helicopter or ship [11].

Previous measurements of the conductivity of sea ice relied almost exclusively on indirect methods which mix the horizontal and vertical components. Moreover, these indirect means make it difficult to accurately recover the dependence of the conductivity on the properties of the brine microstructure, namely, its brine volume fraction ϕ, which depends on the temperature T and salinity S of the ice [4,21,3]. During the 2007 Australian SIPEX expedition, Golden and Gully extracted cylindrical cores of sea ice and made vertical conductivity measurements along these cores using metal probes attached to a Yew Earth Resistance Tester, as described in Ref. [9]. We also measured salinity and temperature along each core in order to relate the electrical measurements to microstructural data [15,7,8,16], such as the brine volume fraction.

Part of our motivation for focusing on the vertical component of the electrical conductivity is that it is closely related to the vertical component of the fluid permeability of sea ice. Fluid

---

* Corresponding author.
E-mail addresses: zhu@math.utah.edu (J. Zhu), golden@math.utah.edu (K.M. Golden), gully@math.utah.edu (A. Gully), christian.sampson@gmail.com (C. Sampson).

0921-4526/$ - see front matter © 2010 Elsevier B.V. All rights reserved.
doi:10.1016/j.physb.2010.01.043

transport in sea ice mediates a broad range of processes such as the growth and decay of seasonal ice, the evolution of melt ponds which determine ice pack albedo, and biomass build-up [8,6]. Our work here will help lay the foundation for electrically monitoring fluid transport in sea ice. In fact, the random resistor network model we develop here is based on the random pipe network we used previously to model the fluid permeability of sea ice [23]. Statistical information about the brine microstructure [15,7,8,16] is used to determine the statistical distributions of the resistors in the electrical network.

2. The network model for the effective conductivity of sea ice

In this model, we consider a piece of sea ice with brine inclusions specified by a brine volume fraction ϕ and other statistical assumptions, and focus on the effect of the brine structure on electrical conduction in the material. More specifically, we study the behavior of the effective vertical conductivity and its dependence on the brine inclusions. Let Φ be the electric potential, and $\boldsymbol{\sigma}$ the local conductivity tensor, which depends on the brine volume fraction. Since the current density J is related to the electric potential through $J=-\boldsymbol{\sigma}\nabla\Phi$, and assuming the material is free of electric charge, the equation for electrical conduction is

$$\nabla\cdot\boldsymbol{\sigma}\nabla\Phi=0. \tag{1}$$

This is similar to the incompressible fluid permeability equation for the pressure from Darcy's law,

$$\nabla\cdot\mathbf{k}\nabla p=0, \tag{2}$$

where p is the incompressible fluid pressure and $\mathbf{k}$ is the permeability tensor.

Here we define the effective conductivity σ_v^* of the sea ice structure in the vertical direction through

$$J_z=-\sigma_v^*\frac{\Delta\Phi}{\Delta z} \tag{3}$$

for the current density J_z in z direction, and the potential difference $\Delta\Phi$ over a thickness Δz.

To simulate the electric field through the conducting microstructure of sea ice, consider an ice sheet of depth D, similar to the structure used in Ref. [23]. Take a thin vertical slice of horizontal thickness h and length span L. We model this ice sheet by a two dimensional lattice of nodes connected by conducting tubes, as shown in Fig. 1. The slice has a rectangular $L\times D$ vertical cross section, which is divided into a grid with m equally spaced sections in the horizontal direction and n equally spaced sections in the vertical direction, so that $L/m=D/n=h$, for some large integers m and n. The model parameter h can be viewed as the dimension of a cell in which a typical brine inclusion is contained. In this network model, h will be chosen according to the sea ice we simulate, its brine volume fraction, and our computing capacities. The tubes are assumed to have circular shapes with different radii, and the current through the medium is induced by an electric potential drop $\Delta\Phi=\Phi_t-\Phi_b$, where Φ_b and Φ_t are the potentials at the bottom and the top of the sea ice sample, with the assumption that $\Phi_b>\Phi_t$ so there is an upward current flow in the medium. The cross sectional areas of the tubes chosen below generate fluid pores comparable to the brine inclusions found in young sea ice. The lattice nodes are the vertices (i,j), $0\le i\le m, 0\le j\le n$, of a rectangular grid, as in Fig. 1(a). Nearest neighbors are connected by vertical and horizontal tubes, with a potential $\Phi_{i,j}$ defined at each node (i,j). To each node (i,j) with $0\le i\le m-1, 0\le j\le n-1$, the horizontal tube to the right of (i,j) has radius $R=R_{i,j}^h$, and the vertical tube on top of (i,j) has radius $R=R_{i,j}^v$, as shown in Fig. 1(b).

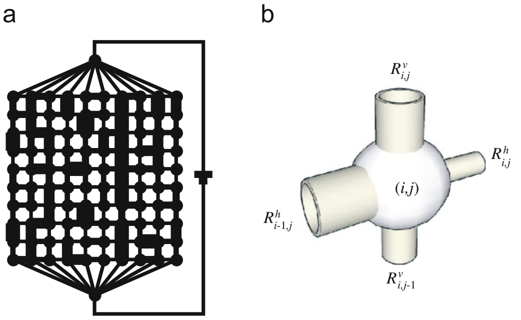

Fig. 1. (a) Random resistor network and (b) close-up of a node and adjoining conducting elements.

Since the brine conductivity is substantially higher than the conductivity of the surrounding ice (on the order of 10^8), we can assume that electrical conduction takes place mostly through the brine tubes. The effect of negligible conduction through pure ice will be modeled by adding a simple conducting component to the system. Unlike the permeability model, where the fluid flux depends only on the brine geometry, electrical conduction in the microstructure includes a temperature dependent local conductivity. For each tube of radius R connecting two nodes with a uniform conductivity σ_{tube}, the electric current through the tube can be established based on the voltage drop and the cross sectional area A as follows:

$$I=\sigma_{tube}AE=-\sigma_{tube}\pi R^2\nabla\Phi, \tag{4}$$

where Φ is the electric potential, E is the electric field and R is the radius of the tube. For each tube connecting two neighboring nodes, the potential gradient can be well approximated by the potential drop divided by the spacing h. Given the potentials at neighboring nodes, different currents converging to the node (i,j) can be easily computed, and they must balance due to Kirkoff's law. Let $\sigma_{i,j}^h$ and $\sigma_{i,j}^v$ denote the brine conductivity for the tubes to the right and on the top of node (i,j), respectively. This leads to the following equations,

$$\begin{aligned}&\sigma_{i,j}^v(R_{i,j}^v)^2(\Phi_{i,j+1}-\Phi_{i,j})+\sigma_{i,j-1}^v(R_{i,j-1}^v)^2(\Phi_{i,j-1}-\Phi_{i,j})\\&\quad+\sigma_{i,j}^h(R_{i,j}^h)^2(\Phi_{i+1,j}-\Phi_{i,j})+\sigma_{i-1,j}^h(R_{i-1,j}^h)^2(\Phi_{i-1,j}-\Phi_{i,j})=0,\end{aligned} \tag{5}$$

for $i=1,\ldots,m-1$, and $j=1,\ldots,n-1$, with appropriate modifications on the edges of the lattice. Notice that this equation is similar to the equation derived for the fluid permeability model [23]:

$$\begin{aligned}&(R_{i,j}^v)^4(p_{i,j+1}-p_{i,j})+(R_{i,j-1}^v)^4(p_{i,j-1}-p_{i,j})\\&\quad+(R_{i,j}^h)^4(p_{i+1,j}-p_{i,j})+(R_{i-1,j}^h)^4(p_{i-1,j}-p_{i,j})=0,\end{aligned} \tag{6}$$

where $p_{i,j}$ is the pressure at node (i,j). We remark that in the conductivity model the coefficients depend on the radius $(\sim R^2)$ not as strongly as in the permeability case $(\sim R^4)$. On the other hand, here the local brine conductivity depends on temperature and salinity, and it could have spatial variations once we allow the temperature and salinity to be spatially non-uniform.

The boundary conditions for Φ are prescribed so that Φ is periodic in the horizontal direction with period L, and it satisfies Dirichlet conditions at the top and bottom of the region as

$$\Phi_{i,n}=\Phi_t,\quad \Phi_{i,0}=\Phi_b. \tag{7}$$

The total current through the brine network system can be obtained by adding currents through all the branches of the top layer,

$$I_{brine} = \pi \sum_{i=0}^{m} \sigma_{i,n-1}^{v} (R_{i,n-1}^{v})^2 \frac{\Phi_{i,n-1} - \Phi_t}{h}. \tag{8}$$

The small effect of additional conduction through pure ice can be modeled as a current flow through another medium in parallel to the brine network,

$$I_{pure\ ice} = \sigma_{ice} Lh(1-\beta) \frac{\Phi_b - \Phi_t}{D}. \tag{9}$$

Here we introduce a coefficient β that models the loss of ice surface/volume for conduction due to the brine inclusions. It should be pointed out that due to the small ratio σ_{ice}/σ_b and the fact that σ_{ice} has a non-negligible temperature dependence, modifications due to β can be ignored in our study of the effective vertical conductivity.

With the introduction of the effective vertical conductivity for this composite in Eq. (3), and the relation between the current and current density,

$$J_z = \sigma_v^* \frac{\Phi_b - \Phi_t}{D} = \frac{I_{brine} + I_{pure\ ice}}{Lh}, \tag{10}$$

we have the effective conductivity

$$\sigma_v^* = \frac{\pi D}{Lh^2} \sum_{i=0}^{m} \sigma_{i,n-1}^{v} (R_{i,n-1}^{v})^2 \frac{\Phi_{i,n-1} - \Phi_t}{\Phi_b - \Phi_t} + (1-\beta)\sigma_{ice}. \tag{11}$$

The effect of β is ignored by setting it to zero in this study.

The multigrid algorithm to solve the system of equations (6) can be modified to solve the system of equations (5), and the numerical convergence is faster due to the coefficient dependence change from R^4 to R^2.

3. Sea ice microstructure and numerical results

In this work, the microstructure of the sea ice slice is described as a collection of tubes with cross sectional areas sampled from a lognormal distribution that subsequently lead to a specified average brine volume fraction ϕ, with parameters based on measurements of brine inclusions in first year sea ice [15,1]. Specifically, we sample the radius R so that $\log A = \log(\pi R^2)$ is normally distributed with mean μ and variance α^2. We also assume that all the random radii are independent from each other. Given a particular sample of the tube radii, the brine volume fraction ϕ of the slice can be readily computed by

$$\phi = \frac{\pi}{LD} \left(\sum_{i=0,j=0}^{m-1,n} (R_{i,j}^{h})^2 + \sum_{i=0,j=0}^{m,n-1} (R_{i,j}^{v})^2 \right). \tag{12}$$

The brine conductivity for each tube is determined by the temperature and the salinity of the sample under consideration, and it is assumed to remain the same value σ_b for all tubes in the sample for this model. The goal of this study is to investigate the dependence of the effective vertical conductivity σ_v^*, and the form factor σ_v^*/σ_b, on the porosity ϕ, which is connected to the microstructure through Eq. (12). For consistency, it is necessary to choose the parameters μ and α such that the desired volume fraction is obtained, and that the statistical properties of the actual sea ice are reasonably matched. To this end, we first notice that given our assumption about the distribution of $\log A$, the expected value of the cross sectional area

$$E[A] = e^{\mu + 1/2\alpha^2}. \tag{13}$$

This should be matched to an interpolation of measured averages for the cross sectional area A as a function of brine volume fraction ϕ [10],

$$\langle A \rangle = \theta(\phi) = \pi(7 \times 10^{-5} + 1.6 \times 10^{-4}\phi)^2 \quad \mathrm{m}^2. \tag{14}$$

This function approximates the dependence of the mean cross sectional area on the brine volume fraction ϕ observed by Perovich and Gow [15] in horizontal thin sections of young, primarily columnar sea ice. It is also observed that $\alpha = 1$ gives a good fit for the range of volume fractions covered here, and consequently we use this value for all the numerical calculations in this work. Once α is determined, the other parameter μ is solved by the matching condition $E[A] = \langle A \rangle$ as above. Throughout this study $n = m = 1024$.

Also as observed in Refs. [7,8,16], brine inclusions in columnar sea ice become connected on macroscopic scales only when the brine volume fraction exceeds around 5%. To reflect this behavior, we allow some randomly selected tubes to be disconnected from the system in an effort to simulate the disconnection of brine inclusions. Since the dominant conduction direction is the vertical direction, we introduce a probability of disconnection for vertical tubes only, consistent with the X-ray tomographic data and pore structure analysis in Refs. [8,16], and this constitutes an additional input to the model.

We proceed to perform numerical simulations for σ_v^* with several situations described by the brine volume fraction, and the corresponding microstructure summarized from our data. For each value of ϕ, we choose an appropriate probability of disconnection to differentiate the microstructure from the others. The brine conductivity σ_b in fact depends on the temperature and the salinity of the sea ice, which characterize the state of the sea ice at the particular level of brine volume fraction. For this study, in order to focus on the effects of the brine volume fraction, we assume a fixed value for the salinity $S = 7$ ppt. We then invert the Frankenstein–Garner relation [4] to obtain

$$T = -\frac{49.185}{\dfrac{1000\phi}{S} - 0.532}, \tag{15}$$

which is then substituted in the Stogryn–Desargant relation [18]

$$\sigma_b = -T \cdot e^{0.5193 + 0.08755T}, \quad T \geq -22.9\,^{\circ}\mathrm{C}, \tag{16}$$

to determine the brine conductivity for the sea ice at a particular brine volume fraction ϕ. The values of temperature and brine conductivity, as well as the probabilities of disconnection that describe one important aspect of the microstructure, are listed in Table 1 for selected values of the brine volume fraction for which we perform numerical simulations in this work. We also use an average pure ice conductivity value of $\sigma_{ice} = 1.1 \times 10^{-8}$ at a temperature $T = -10\,^{\circ}\mathrm{C}$. Here all the conductivity quantities have the unit $\mathrm{Ohm}^{-1}\,\mathrm{m}^{-1}$.

In Fig. 2, we plot the values of the effective vertical conductivity σ_v^* and form factor σ_v^*/σ_b from our measured data sets and compare with the results of the network model. First we note that our assumption $\sigma_{i,j}^{v} = \sigma_{i,j}^{h} = \sigma_b$ simplifies Eq. (5) such that the solution Φ is independent of σ_b. This allows us to separate the effects of decreasing σ_b and increasing σ_v^* as ϕ increases. As we see from the graphs for both the effective vertical conductivity and the form factor, our results show close agreement with the measurements. In Fig. 2(a), the simulated curve is consistent with

Table 1
Numerical parameters used in simulation.

ϕ (%)	2.5	5.0	7.5	10.0	12.5
$P_{\mathrm{disconnect}}$	0.9	0.7	0.5	0.25	0
T (°C)	−16.18	−7.44	−4.83	−3.58	−2.84
σ_b ($\mathrm{Ohm}^{-1}\,\mathrm{m}^{-1}$)	6.596	6.519	5.319	4.395	3.722

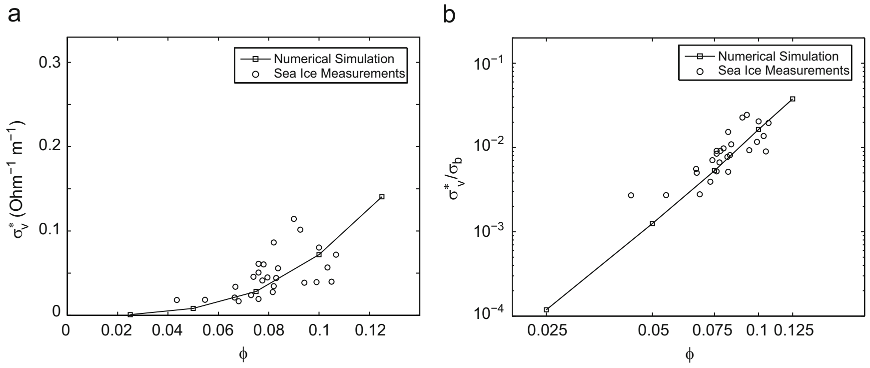

Fig. 2. (a) Data on the vertical conductivity of first year Antarctic sea ice is compared with the results of numerical simulations and (b) data on the form factor is compared with numerical results from the network model, and displayed on a logarithmic scale.

critical behavior in a finite volume. For the form factor comparison in Fig. 2(b), we choose a log–log scale to detect any linear behavior, which would suggest Archie's law behavior. As demonstrated in this log–log graph, such a power law could also be developed from this network model. These results are consistent with the behavior found for the fluid permeability in Ref. [8]. In Ref. [9] we use percolation theory and other methods to analyze our vertical conductivity data.

4. Conclusions

We have developed a network model for the vertical conductivity of sea ice. The model incorporates statistical information about the brine microstructure, through a lognormal distribution describing the temperature dependence of the inclusion sizes, and connectivity information obtained from X-ray CT data. The model agrees well with field data for Antarctic sea ice. Our work will aid in measurements of sea ice thickness which depend on knowledge of its electrical properties.

Acknowledgements

We are grateful for the support provided by the Division of Mathematical Sciences, the Division of Atmospheric Sciences, and the Arctic Natural Sciences Program at the US National Science Foundation (NSF). We also thank T. Worby, J. Reid, the Australian Antarctic Division and the crew of the *Aurora Australis* for their support of our work during the SIPEX Antarctic expedition. Adam Gully gratefully acknowledges the support of the NSF Research Experiences for Undergraduates (REU) Program and an NSF VIGRE graduate fellowship, and Christian Sampson gratefully acknowledges support from the NSF REU Program.

References

[1] C. Bock, H. Eicken, Ann. Glaciol. 40 (2005) 179.
[2] R.G. Buckley, M.P. Staines, W.H. Robinson, Cold Reg. Sci. Tech. 12 (1986) 285.
[3] H. Eicken, Growth, microstructure and properties of sea ice, in: D.N. Thomas, G.S. Dieckmann (Eds.), Sea Ice: An Introduction to its Physics, Chemistry, Biology and Geology, Blackwell, Oxford, 2003, pp. 22–81.
[4] G. Frankenstein, R. Garner, J. Glaciol. 6 (48) (1967) 943.
[5] K. Fujino, Y. Suzuki, Low Temp. Sci. A 21 (1963) 151.
[6] K.M. Golden, Not. Amer. Math. Soc. 56 (5) (2009) 562.
[7] K.M. Golden, S.F. Ackley, V.I. Lytle, Science 282 (1998) 2238.
[8] K.M. Golden, H. Eicken, A.L. Heaton, J. Miner, D. Pringle, J. Zhu, Geophys. Res. Lett. 34 (2007) L16501 (6 pages and issue cover), doi:10.1029/2007GL030447.
[9] K.M. Golden, A. Gully, C. Sampson, J. Zhu, A.P. Worby, J. Reid, Theory and measurements of electrical conductivity in Antarctic sea ice, Deep Sea Res. (2009), submitted.
[10] K.M. Golden, A.L. Heaton, H. Eicken, V.I. Lytle, Mech. Mat. 38 (2006) 801.
[11] C. Haas, Cold Reg. Sci. Tech. 27 (1998) 1.
[12] C. Haas, Dynamics versus thermodynamics: the sea ice thickness distribution, in: D.N. Thomas, G.S. Dieckmann (Eds.), Sea Ice: An Introduction to its Physics, Chemistry, Biology and Geology, Blackwell, Oxford, 2003, pp. 82–111.
[13] C. Haas, Geophys. Res. Lett. 31 (2004) L09402, doi: 10.1029/2007GL030447.
[14] C. Haas, S. Gerland, H. Eicken, H. Miller, Geophysics 62 (1997) 749.
[15] D.K. Perovich, A.J. Gow, J. Geophys. Res. 101 (C8) (1996) 18,327.
[16] D.J. Pringle, J.E. Miner, H. Eicken, K.M. Golden, J. Geophys. Res. C 114 (2009) C12017 (14 pages), doi:10.1029/2008JC005145.
[17] J.E. Reid, A. Pfaffling, A.P. Worby, J.R. Bishop, Ann. Glaciol. 44 (2006) 217.
[18] A. Stogryn, G.J. Desargant, IEEE Trans. Antennas Propagat. AP-33 (5) (1985) 523.
[19] F. Thyssen, H. Kohnen, M.V. Cowan, G.W. Timco, Polarforschung 44 (1974) 117.
[20] G.W. Timco, J. Glaciol. 22 (1979) 461.
[21] W.F. Weeks, S.F. Ackley, The growth, structure and properties of sea ice, in: N. Untersteiner (Ed.), The Geophysics of Sea Ice, Plenum Press, New York, 1986, pp. 9–164.
[22] A.P. Worby, P.W. Griffin, V.I. Lytle, R.A. Massom, Cold Reg. Sci. Tech. 29 (1999) 49.
[23] J. Zhu, A. Jabini, K.M. Golden, H. Eicken, M. Morris, Ann. Glaciol. 44 (2006) 129.

CHAPTER 6

SURFACE IMPEDANCE TOMOGRAPHY FOR ANTARCTIC SEA ICE

In this chapter we explore the use of surface impedance tomography as it applies to determining ice thickness and composition. We explore n-layer inversions using data obtained with a Wenner array during SIPEX I in 2007. We show that accurate reconstructions of sea ice resistivity profiles can be done provided the proper regularization considerations are taken into account. Chapter 6 is a reprint originally published in *Deep-Sea Research II* with authors **Christian S. Sampson, Kenneth M. golden, Adam Gully, and Anthony P. Worby.** It is reproduced here with permission of the publisher.

Deep-Sea Research II 58 (2011) 1149–1157

Contents lists available at ScienceDirect

Deep-Sea Research II

journal homepage: www.elsevier.com/locate/dsr2

Surface impedance tomography for Antarctic sea ice

C. Sampson [a], K.M. Golden [a,*], A. Gully [a], A.P. Worby [b]

[a] University of Utah, Department of Mathematics, 155 S 1400 E RM 233, Salt Lake City, UT 84112-0090, USA
[b] Australian Antarctic Division and ACE CRC, University of Tasmania, Private Bag 80, Hobart 7001, Australia

ARTICLE INFO

Article history:
Received 9 December 2010
Accepted 9 December 2010
Available online 15 December 2010

Keywords:
Sea ice
Electrical conductivity
Wenner array
Surface impedance tomography

ABSTRACT

During the 2007 SIPEX expedition in pack ice off the coast of East Antarctica, we measured the electrical conductivity of sea ice via surface impedance tomography. Resistance data from classical four-probe Wenner arrays on the surfaces of ice floes were used to indirectly reconstruct the conductivity profiles with depth, involving both the horizontal and vertical components. A common problem with these reconstructions is the lack of uniqueness of the inversions, which worsens as the number of layers in the model increases. In the past, three layer inversions have been used to help avoid non-uniqueness. However, this approach assumes that the conductivity profile of sea ice does not change very much with depth. In order to investigate the conductivity profiles one needs to use more layers in the reconstruction. A reasonable starting model is a useful tool that can be used to regularize the inverse problem, allowing a reconstruction that not only matches the Wenner impedance data but the actual profile. Using measurements of brine volume fraction for 10 cm sections of ice cores taken at the Wenner array site, and various models relating brine volume fraction to conductivity, we compare the predicted conductivity profiles based on the models to the reconstructions from the tomographic measurements. We note the close agreement with the actual data for some models and the inadequacy of others. Such models could be useful in finding a reasonable starting point for regularizing inversions, and using *n*-layer models to reconstruct accurate conductivity profiles. Our results help to provide a rigorous basis for electromagnetic methods of obtaining sea ice thickness data, a key gauge of the impact of climate change in the polar regions.

1. Introduction

The polar sea ice packs play a fundamental role in Earth's climate system, and are leading indicators of climate change (Thomas and Dieckmann, 2003; Serreze et al., 2007). They also host extensive algal and bacterial communities which sustain life in the polar oceans (Thomas and Dieckmann, 2003; Fritsen et al., 1994). Refining predictions of climate change and the future trajectory of the polar ice packs depends on accurate knowledge of their thickness distribution. Not only is this knowledge important in comparing model predictions to observed behavior, but in specifying the initial conditions necessary to study the time evolution of these nonlinear systems. Determining the thickness distribution, however, remains an elusive problem. Due to the vast extent of the polar sea ice packs, it is impractical of course to drill the millions of holes or more that would be needed to accurately assess the thickness distribution over a particular region or time period. Thus, other methods have been and are being developed, many of which use electromagnetic techniques, such as electromagnetic induction (EMI) devices (Haas et al., 1997; Haas, 1998, 2004; Worby et al., 1999; Reid et al., 2006) mounted on ships, planes or helicopters. Electromagnetic techniques, in general, rely on some knowledge of the effective electrical properties of sea ice and how they vary with depth, temperature, salinity, ice type, etc. in the analysis of the data to obtain thickness information.

The electrical conductivity of sea ice is also closely related to its fluid transport properties. Fluid flow through sea ice mediates a broad range of processes which are important in climatological and biological studies. These include the evolution of melt ponds in the Arctic, surface flooding and snow-ice formation in the Antarctic, the evolution of salinity profiles, convection-enhanced thermal transport, CO_2 fluxes, and nutrient replenishment for microbial communities. In (Golden et al., in preparation) we found the electrical signature of the *rule of fives* (Golden et al., 1998a, 2007; Pringle et al., 2009), where columnar sea ice is effectively impermeable for brine volume fractions below about 5% and increasingly permeable above this threshold. Relating fluid and electrical transport properties in this way lays the foundation for electromagnetic monitoring of the above processes.

Early DC resistivity measurements of sea ice were aimed at determining ice thickness (Fujino and Suzuki, 1963;

---

[*] Corresponding author. Tel.: +1 801 581 6176; fax: +1 801 581 4148.
E-mail address: golden@math.utah.edu (K.M. Golden).

0967-0645/$ - see front matter © 2010 Elsevier Ltd. All rights reserved.
doi:10.1016/j.dsr2.2010.12.003

Thyssen et al., 1974; Timco, 1979). These studies employed surface soundings using 4 electrodes in either the Wenner or Schlumberger configurations. Thyssen et al. (1974) also made *in situ* measurements of sea ice resistivity using electrodes inserted into the vertical face of a pit that was dug in the unrafted ice near one of their sites. The apparent resistivity was measured perpendicular and parallel to the ice surface, and this data was analyzed further by Timco (1979). He attempted to interpret sounding results in terms of the sea ice microstructure, and it was also possible to see changes in the resistivity structure during spring warming. Nevertheless, such measurements have been somewhat unfruitful as a means of investigating either ice thickness or microstructural detail. Later measurements in the Antarctic were also reported (Buckley et al., 1986). The anisotropic nature of the resistivity of sea ice leads to measurements significantly underestimating the ice thickness (Reid et al., 2006) by a factor $\sqrt{\rho_v^*/\rho_h^*}$, where ρ_v^* and ρ_h^* are, respectively, the vertical and horizontal components of the bulk resistivity (Bhattacharya and Patra, 1968), with $\sigma_v^* = 1/\rho_v^*$ and $\sigma_h^* = 1/\rho_h^*$, the vertical and horizontal components of the bulk conductivity. Surface measurements also lead only to an estimate of the geometric mean resistivity $\sqrt{\rho_v^*\rho_h^*}$.

More promising determinations of sea ice thickness have been achieved using low frequency electromagnetic induction (EMI) techniques (Haas et al., 1997; Haas, 1998, 2004; Worby et al., 1999; Reid et al., 2006). The technique relies on a time varying primary magnetic field generated by a transmitter coil. The measured secondary magnetic fields are due to the currents induced within a volume of the subsurface (i.e., the footprint) by the EMI system. The measured secondary fields at the receiver are a weighted average of the response due to all the currents within the footprint. The thickness has been found using empirical relationships (Haas, 2003), with good results for smooth ice and underestimates near ridges (Haas, 2003). However, theoretical approaches (Kovacs and Holladay, 1990; Prinsenberg et al., 2002) have also been used, where the measured secondary fields are inverted for sea ice thickness (and hopefully, the sea water conductivity and horizontal sea ice conductivity). The inversion approach assumes very accurate calibration of the EMI system. The EMI technique is adaptable to continuous measurements being made either from a helicopter or ship (Haas, 1998; Reid et al., 2006; Kovacs and Holladay, 1990; Prinsenberg et al., 2002). Theoretical modeling of electromagnetic measurements suggests a sea ice resistivity of some 10's of Ω m (Haas et al., 1997; Reid et al., 2006) — in broad agreement with DC resistivity determinations of $\sqrt{\rho_v^*\rho_h^*}$, although electromagnetic measurements as yet have been unable to provide any microstructural information. Moreover, theoretical results which accurately relate effective electrical properties of sea ice to key parameters characterizing the brine phase have been lacking.

As a step toward providing a deeper understanding of the electrical properties of sea ice, and in particular how they depend on the brine microstructure and vary with depth, we made measurements of these properties in the Antarctic. During September and October of 2007, two of us (K.M.G. and A.G.) measured the electrical conductivity of first year Antarctic pack ice as participants in the Australian Sea Ice Physics and Ecosystem eXperiment (SIPEX), aboard the icebreaker *Aurora Australis*. The study area was located off the coast of East Antarctica, between 115° E and 130° E, and 64° S and 66° S. At 12 of the 15 ice stations along the cruise track of the *Aurora*, we conducted electrical soundings using a Wenner array with probes inserted into the surface of the ice over a range of spacings (Fig. 1). The separation of the probes ranged from 5 cm to 5 m. We also extracted full ice cores at each site and took temperature and salinity profiles for each core in order to obtain a brine volume profile for the ice where we measured electrical properties. Using an inversion scheme, we reconstructed information about the conductivity profile with depth. In (Golden et al., in preparation) we report on direct measurements of the vertical conductivity of the ice, and theoretical models relating sea ice electrical properties to the characteristics of the brine microstructure. We use the theoretical results here to help constrain the inversion scheme.

Fig. 1. A Wenner electrode array along the surface of Antarctic sea ice, with the *Aurora Australis* in the background. A current I is injected through the outer electrodes C1 and C2. The potential difference ΔV resulting from the current flow is measured at the inner electrodes P1 and P2.

2. The bulk conductivity of sea ice

Sea ice is a complex, high contrast composite material of pure ice with brine and air inclusions. What determines the response of an ice floe in a Wenner sounding is the effective or bulk conductivity of the sea ice and its variation with depth. Predicting the effective electromagnetic properties of sea ice, such as its electrical conductivity, is a challenging theoretical problem. While pure ice and air are essentially electrical insulators, the brine phase is highly conducting. The relative volume fraction ϕ of brine, the geometry of the inclusions, and in particular their connectivity, are all highly dependent on temperature (Perovich and Gow, 1996; Golden et al., 1998a, 2007; Pringle et al., 2009). The brine inclusions in general display a preferred elongation in the vertical direction, as does the brine connectivity (Golden et al., 2007; Pringle et al., 2009). The conductivity tensor of sea ice is thus anisotropic.

Let us briefly formulate the problem of finding the effective or bulk conductivity of a two phase composite material (Golden and Papanicolaou, 1983; Golden et al., 1998b; Gully et al., 2007). For these considerations we ignore the air phase in sea ice. Let the local conductivity $\sigma(x)$ be a spatially stationary random field in $x \in \mathbb{R}^3$, for an appropriate probability space representing the set of realizations of the random medium. While sea ice may exhibit significant variations in microstructural properties over its entire depth, relatively thin layers such as 5 or 10 cm often display only small variations in these properties. It is then reasonable to assume that in typical sample sizes on this scale, the statistics describing the brine microstructure in such a region are represented by a stationary random function throughout all of $\mathbb{R}^3$. We assume $\sigma(x)$ takes the value $\sigma_1 = \sigma_b$ in the brine phase, which depends on temperature T via (Stogryn and Desargant, 1985)

$$\sigma_b = -T\exp(0.5193 + 0.08755T) \quad \Omega^{-1}\,\mathrm{m}^{-1},$$

$$T \geq -22.9\,^\circ\mathrm{C}. \tag{1}$$

In the ice phase, $\sigma(x)$ takes the value $\sigma_2 = \sigma_i = 1.1 \times 10^{-8}\ \Omega^{-1}\ \mathrm{m}^{-1}$, which is the value at $T = -10\ ^\circ\mathrm{C}$ (Hobbs, 1974). The value in ice is effectively 0 compared to the values of σ_b in brine, which lie between about 3 and $7\ \Omega^{-1}\ \mathrm{m}^{-1}$. We write $\sigma = \sigma_1\chi + \sigma_2(1-\chi)$, where $\chi(x)$ is the characteristic function of the brine phase, with $\chi(x) = 1$ for x in the brine and $\chi(x) = 0$ for x in the ice. The brine volume fraction ϕ is given by $\phi = \langle \chi \rangle$, where $\langle \cdot \rangle$ means an ensemble average or spatial average over all of $\mathbb{R}^3$, and depends on temperature T (°C) and salinity S parts per thousand (ppt) through the Frankenstein–Garner relation (Frankenstein and Garner, 1967),

$$\phi = \frac{S}{1000}\left(\frac{49.185}{|T|} + 0.532\right). \tag{2}$$

Let $E(x)$ and $J(x)$ be the stationary random electric and current fields satisfying the constitutive law $J(x) = \sigma(x)E(x)$ and the equations

$$\nabla \times E(x) = 0, \quad \nabla \cdot J(x) = 0, \tag{3}$$

with $\langle E(x) \rangle = e_k$, where e_k is a unit vector in the kth direction for some $k = 1, 2, 3$. The effective conductivity tensor $\boldsymbol{\sigma}^*$ is defined by (Golden and Papanicolaou, 1983)

$$\langle J \rangle = \boldsymbol{\sigma}^* \langle E \rangle. \tag{4}$$

For convenience, we focus on one diagonal coefficient $\sigma^* = \sigma^*_{kk}$. Due to the homogeneity of effective parameters, $\sigma^*(\lambda\sigma_1, \lambda\sigma_2) = \lambda\sigma^*(\sigma_1, \sigma_2)$, where λ is any scalar, σ^* depends only on the ratio $h = \sigma_1/\sigma_2$, and we define $m(h) = \sigma^*/\sigma_2$. The two main properties of $m(h)$ are that it is analytic off $(-\infty, 0]$ in the h-plane, and that it maps the upper half plane to the upper half plane, so that it is an example of a Herglotz, or Stieltjes function.

An integral representation (Bergman, 1978; Milton, 1980; Golden and Papanicolaou, 1983; Golden, 1986; Milton and Golden, 1990) for $m(h)$ which provides an important relationship between microstructural information and the effective conductivity is

$$\mathcal{F}(s) = 1 - m(h) = \int_0^1 \frac{d\mu(z)}{s - z}, \tag{5}$$

$$s = 1/(1-h), \quad s \notin [0,1],$$

where $\mathcal{F}(s)$ is analytic off [0,1], and μ is a positive measure on [0,1]. Formula (5) separates the parameter s from information about the mixture geometry contained in μ, which is a spectral measure of the operator $\Gamma\chi$, where $\Gamma = \nabla(-\Delta)^{-1}\nabla$. Statistical assumptions about the random medium (via the correlation functions) are incorporated through the moments μ_n of μ. For example, $\mu_0 = \int_0^1 d\mu(z) = \langle \chi \rangle = \phi$, the porosity. Rigorous bounds on σ^* can be obtained from (5) (Bergman, 1978; Milton, 1980; Golden and Papanicolaou, 1983; Golden, 1986). Comparisons of conductivity data with these bounds will be presented elsewhere.

Archie's law (Archie, 1942) is an empirical equation relating the bulk conductivity σ^* of a porous medium to its porosity and the conductivity σ_f of the fluid occupying the pore space,

$$\sigma^* = a\sigma_f\phi^m. \tag{6}$$

In this relation, ϕ is the relative volume fraction of the fluid, or porosity, and a is an empirical scaling parameter often taken to be 1, which yields the correct limiting behavior as $\phi \to 1$. In sea ice, where we expect somewhat different behavior in different volume fraction regimes, there is no particular reason for a to be taken to be 1. The exponent m depends on the geometry of the solid phase of the porous medium, such as the shapes of the grains in porous rock or sand.

The conductivity σ_b of brine depends on its temperature through equation (1). In studying how the vertical conductivity σ^*_v depends on brine volume fraction ϕ, we note that the brine conductivity σ_b changes as a function of temperature, as does brine volume fraction via equation (2). It is then useful to consider the vertical formation factor

$$F = \frac{\sigma^*_v}{\sigma_b}, \tag{7}$$

which removes the dependence of the effective parameter on the changing conductivity of the brine itself, and depends only on the pore volume fraction and geometry. This parameter is commonly used in the analysis of other porous media such as brine-filled rocks and marine sands (Sahimi, 1995; Sen et al., 1981; Jackson et al., 1978), although the more standard definition is in terms of resistivity, ρ^*_v/ρ_b. Archie's law in (6) for the vertical formation factor is then

$$F(\phi) = a\phi^m. \tag{8}$$

In (Golden et al., in preparation) we use percolation theory to closely capture vertical conductivity data for Antarctic sea ice, with a critical threshold of about 5%. From a rigorous standpoint, the two approaches are inconsistent, in that Archie's law can be viewed as describing systems with connectivity all the way down to $\phi = 0$. It is nevertheless still useful to analyze the conductivity of sea ice using Archie's law, particularly to compare our findings with previous works (Thyssen et al., 1974; Reid et al., 2006; Ingham et al., 2008), as well as with previous work on fluid permeability (Golden et al., 2007). Moreover, Archie's law provides a formula for the conductivity below the threshold brine volume fraction, whereas percolation theory predicts a value of zero in this regime. By combining critical path analysis, relations between the electrical conductivity and fluid permeability, and statistical best fits, in (Golden et al., in preparation) we find the following model for the formation factor, which also closely captures vertical conductivity data,

$$F(\phi) = 8.6\phi^{2.75}. \tag{9}$$

We will use this formula here in our inversion analysis of the Wenner array data. For comparison, we will also use $F(\phi) = \phi^{1.9}$, where a is forced to be 1, and the exponent comes from a statistical best fit, although it is close to the value of 2 arising from theoretical considerations. This second model underestimates the conductivity above the threshold more than (9), which provides a better approximation to percolation theory, and is discussed elsewhere.

3. Surface impedance tomography

3.1. Formulation of the method for the Wenner array

In addition to the direct measurements of the vertical conductivity, Wenner soundings were conducted at 12 of the ice stations during SIPEX. A Wenner array consists of 4 electrodes spaced evenly apart, which are inserted into the surface of the sea ice. Current flows between the two outer electrodes C1 and C2 in Fig. 2, and a potential difference is measured between the two inner electrodes P1 and P2. Resistance measurements for the Wenner electrode array were taken with a Yokogawa Electric Works (YEW) Specific Earth Resistance Tester operating at 38 Hz.

From the measured potential difference we can obtain an estimate for the apparent resistivity ρ^*_a via the following equation, where a is the separation distance (Parasnis, 1986),

$$\rho^*_a = 2\pi a\frac{\Delta V}{I} = 2\pi aR. \tag{10}$$

The basic features of the Wenner soundings are as follows: (1) As the separation distance a is increased, the current penetrates deeper into the ice. (2) The apparent resistivity ρ^*_a changes for

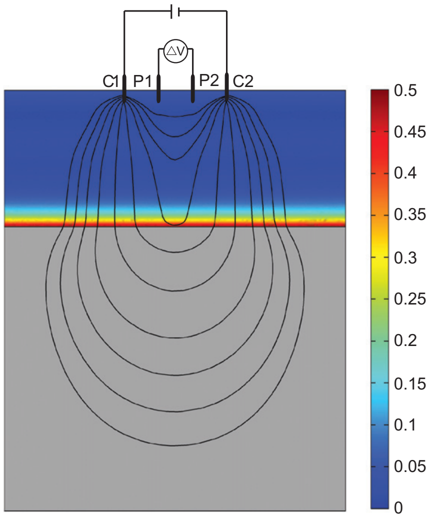

Fig. 2. A Wenner array with four evenly spaced electrodes, probing a sea ice floe of thickness 0.8 m, on top of sea water. The color scale indicates the value of the vertical conductivity of the sea ice in $(\Omega\,\text{m})^{-1}$, calculated from a brine volume profile we measured in Antarctica, using $F(\phi)=8.6\phi^{2.75}$. The horizontal conductivity is assumed to be 1/4 the value in the vertical direction. Comsol 3.5a was used to calculate the electric current streamlines. The conductivity of the sea water is 4.8 $(\Omega\,\text{m})^{-1}$.

each measurement. (3) A curve of the apparent ice resistivities can be constructed from the measurements. (4) The sounding curve data can then be inverted to obtain a layered model of resistivities.

It can be shown (Bhattacharya and Patra, 1968) that for a given Wenner array spacing a, the apparent resistivity measured at the surface is

$$\rho_a^* = \rho_1^*(1+4G(a)-4G(2a)), \tag{11}$$

where

$$G(x) = 1+2x\int_0^\infty K(\lambda)J_0(\lambda x)\,d\lambda, \tag{12}$$

J_0 is the Bessel function of order zero and $K(\lambda)$ is a function depending on the resistivities and thicknesses of all the layers. An example of $K(\lambda)$ comes from a two layered earth model,

$$K(\lambda) = \frac{-k_1e^{-2\lambda h_1}}{1+k_1e^{-2\lambda h_1}}, \quad k_1 = \frac{\rho_1^*-\rho_2^*}{\rho_1^*+\rho_2^*}, \tag{13}$$

where ρ_1^* and ρ_2^* are the apparent resistivities of the first and second layer, respectively, h_1 is the depth of the first layer, and the second layer is a homogeneous half-space.

For our measurements the spacing value a ranged initially from 0.05 m to 20 m with the midpoint of the array at a fixed position. Above a 5 m spacing, however, the instrument could no longer give a reading. The lack of a reading at large a is probably because the potential difference between the receiver electrodes becomes very small over conductive sea water, and the voltage resolution limit of the meter has been reached. This behavior was observed at each ice station. The data from 5 ice stations are presented in Table 1.

We analyze our Wenner data in two ways. First, we do preliminary three layer inversions closely following the method used by Reid et al. (2006). This allows us to get an idea of the factor of anisotropy. Second, we compare the Wenner data to the conductivity models discussed above, namely, Archie's law with $a=1$, $m=1.9$ and with $a=8.6$, $m=2.75$ (which is closer to percolation theory) by building an n-layer model yielding a theoretical sounding curve. We compare this to the measured curve. This comparison is useful, because we will see that for different ranges of ϕ the differences between percolation theory *vs.* Archie's Law are reflected in the Wenner analysis as well.

Table 1
Five sets of Wenner array data.

a (m)	ρ_a^* (Ω m)				
	Station 5	Station 6	Station 8	Station 13	Station 14
0.05	62.83	7.85	4.62	5.91	5.03
0.08	60.32	9.30	5.83	7.29	6.03
0.125	113.88	11.78	8.01	10.45	6.52
0.2	113.1	15.71	10.3	11.81	8.29
0.32	114.1	20.11	12.87	11.26	10.05
0.5	71	20.42	13.19	8.64	10.68
0.8	25.13	16.08	8.65	4.12	9.7
1.25	5.5	8.64	6.28	1.34	5.97
2.0	0.94	2.58	1.52	0.53	2.34
3.2	0.2	0.8	0.2	0.42	0.92
5.0	0	0	0	0	0

3.2. Preliminary three layer inversions

We now present the results of simple three layer inversions of the Wenner array data obtained during the SIPEX 2007 expedition. These 3-layer models will become important in the following sections and shed light on the anisotropic nature of sea ice through an estimation of the factor of anisotropy. These results will allow us to relate our models for the vertical conductivity to the type of data obtained through Wenner arrays, where vertical and horizontal components of the electrical properties are mixed.

Since sea ice is horizontally isotropic when there is no preferred long term current direction (Golden and Ackley, 1981), as was the case during SIPEX, and the vertical conductivity is higher than the horizontal component, it is "transversely isotropic." In fact, at ice station 5 we made Wenner array measurements in two orthogonal directions, and found no evidence of anisotropy in the horizontal plane. Maillet (1947) has shown that a transversely isotropic layer of actual thickness t_{act} with conductivities σ_h^* and σ_v^* yields an identical DC sounding response to an isotropic layer of thickness

$$t = \sqrt{\frac{\sigma_h^*}{\sigma_v^*}}\,t_{act} \tag{14}$$

and conductivity $\sigma_m^* = \sqrt{\sigma_h^*\,\sigma_v^*}$, the geometric mean of σ_h^* and σ_v^*. When we consider these relations, if we have a direct thickness measurement t_{act}, say from drilling, then we could use a sounding curve obtained from the Wenner data and invert for the thickness of the ice. Using the actual thickness t_{act} and the inverted thickness t we can calculate the factor of anisotropy $f=\sqrt{\sigma_h^*/\sigma_v^*}$ for the ice using

$$f = \frac{t}{t_{act}}. \tag{15}$$

The model we use to make the above calculation is a simple 3-layer model consisting of a thin, fairly conductive top layer, a thicker, less conductive middle layer and a semi-infinite, very conductive bottom layer representing the sea water.

Reid et al. (2006) have shown that typically the inversions yield a top layer which is just a few centimeters thick, which holds up under analysis of equivalent models. In this way the inverted thickness of the ice can be taken as the thickness of the second layer. The benefit of this is that the top layer is often granular and tends to be more isotropic, as the anisotropy arises from the preferred vertical orientation of the brine inclusions in columnar ice, whereas in granular ice any anisotropy is generally not so pronounced. Thus, from the model thickness of the second layer and the actual thickness obtained from drilling the ice, we can find the factor of anisotropy using $f=t/t_{act}$. We carried out the inversions using the software IP2WIN, which is used for 1-D Vertical Electrical Sounding (VES) interpretation and inversion, from the website http://geophys.geol.msu.ru/ipi2win.htm, V. A. Shevnin and I. N. Modin, Geological Faculty, Department of Geophysics, Moscow State University.

A typical 3-layer inversion is illustrated in Fig. 3, while some values for the inverted thickness and factor of anisotropy are presented in Table 2. We typically find that the factor of anisotropy f is reasonably close to 0.5, which can vary with equivalent models used. Table 2 represents some of the extreme values away from f=0.5. A result of f=0.5 agrees with results found by Buckley et al. (1986) for undeformed first year Antarctic sea ice.

3.3. Comparison of Wenner data to conductivity models

For our analysis, four sets of Wenner array measurements are paired up with brine volume fraction measurements to predict a sounding curve from our models. Other stations yield good sounding curves, but do not have corresponding brine volume fraction measurements with depth. Some stations were left out of the analysis due to a large shift in the thickness of the ice over the length of the array, which renders the Wenner technique inaccurate, as uniform thickness is needed. Our general approach is outlined here:

- First we plot the measured apparent resistivity ρ_a^* *vs.* the spacing a.
- We then perform a simple 3-layer inversion to obtain the factor of anisotropy f and estimate the thickness and resistivity of the first layer.
- Using the factor of anisotropy we relate our models for vertical conductivity as a function of brine volume fraction ϕ to the mean resistivity of the sea ice ρ_m^*. We also relate the thickness of directly measured layers to the thicknesses of layers which would yield an identical sounding curve (t=ft_a) using the mean resistivity.
- Using our estimate of the thickness and resistivity of the first layer from the 3-layer inversion, and the thicknesses of all subsequent layers calculated from our models and f, we build an n-layer model of the resistivity of sea ice with depth (step function).
- We then compare the predicted (gray) sounding curves from these models to the measured (black) curves which connect the data points.

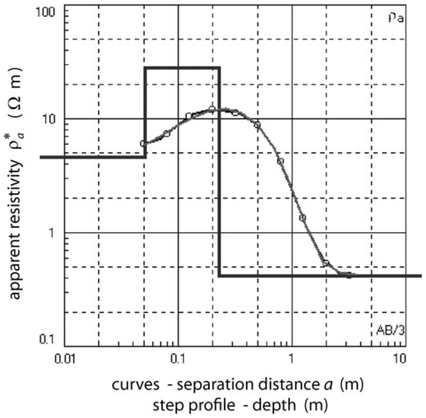

Fig. 3. A typical 3-layer inversion, where the black curve connects the measured data points, the step function represents the 3-layer model, and the gray curve is the predicted sounding curve from the 3-layer model, which matches the black curve very closely. The vertical axis represents the apparent mean resistivity $\rho_a^*=\sqrt{\rho_v^*\rho_h^*}$ while the horizontal axis represents the electrode spacing for the black and gray curves and depth for the step profile. Here the RMS error is 2.94%.

Table 2
The inverted thickness (t), actual thickness (t_{act}), factor of anisotropy f, and height of the first layer h_1 for the Wenner measurements at four different ice stations.

Ice station	t (cm)	t_{act} (cm)	$f=t/t_a$	h_1 (cm)
5	27.7	69	0.40	2.8
6	25.4	37	0.69	9
13	17.6	41	0.43	5.1
14	48.7	86	0.57	10

Given that our theoretical models reasonably represent the conductivity of sea ice, if we have measurements of the brine volume fraction ϕ and the conductivity of the brine σ_b for different depths of the ice, we should be able to predict an n-layer model which fits a measured Wenner sounding curve. However, we must take the anisotropy of the ice into account. Here we present a general method for making this kind of prediction using our Archie's law analysis. Here n is the number of sections of an ice core for which we have measurements. Most inversion schemes for Wenner sounding data take resistivity as an input, thus we can obtain a model using $\rho_v^*=(\sigma_v^*)^{-1}=(a\sigma_b\phi^m)^{-1}$.

Since Wenner arrays do not resolve anisotropy, we must account for this to predict an accurate sounding curve. As mentioned before, we can relate the horizontal and vertical conductivities to an equivalent isotropic conductivity through their geometric mean, $\sigma_m^*=\sqrt{\sigma_h^*\,\sigma_v^*}$ and the factor of anisotropy $f=\sqrt{\sigma_h^*/\sigma_v^*}$. Also, as stated before, sea ice is usually transversely isotropic. In this case (Maillet, 1947) a transversely isotropic layer with thickness t_{act} and conductivities σ_h^* and σ_v^* yields an identical DC sounding response to an isotropic layer of thickness $t=\sqrt{\sigma_h^*/\sigma_v^*}t_{act}$ and conductivity $\sigma_m=\sqrt{\sigma_h^*\sigma_v^*}$. We mention that a much more detailed analysis of anisotropy and its effect on resistance measurements in sea ice has been done by Jones et al. (2010).

If values for a and m are determined for the vertical conductivity in Archie's law, we can then find the equivalent isotropic resistivity ρ_m^* using the factor of anisotropy since $f\rho_m^*=f\frac{1}{\sigma_m^*}=\frac{1}{\sigma_v^*}=\rho_v^*$. Thus,

$$\rho_m^*=\frac{\rho_v^*}{f}=\frac{1}{f\sigma_v^*}=\frac{1}{fa\sigma_b\phi^m}. \tag{16}$$

If we have measurements for ϕ, σ_b, and f for a given layer, we can find the mean resistivity that would fit the Wenner sounding curve, and then we can build an n-layer model. However, finding a factor of anisotropy for each measured section is difficult. Instead we find a factor of anisotropy for the entire sea ice sheet using a simple 3-layered model inversion and the relation $f=t_{act}/t$, where t is the inverted thickness from the model.

From here we can build a profile of the mean resistivities at different depths given the brine volume fraction using (16). We can also calculate the apparent thickness of the layer at that depth using the known measured thickness of a layer for a given brine volume fraction and the factor of anisotropy with $t{=}ft_{act}$. It is important to note that the first layer of the inversion comes from granular ice. We allow the 3-layer inversion to predict its resistivity and thickness because it should be correct for an isotropic medium. If one does not do this, the resistivity is typically overestimated.

An overview of the n-layer inversion scheme is as follows:

1. Run a 3-layer inversion to find f and estimate the thickness and resistivity of the first layer.
2. Compute ρ_m^* for the subsequent layers using (16).
3. Compute the thickness the Wenner array "sees" for each layer with $t{=}ft_{act}$.
4. Compare the predicted sounding curve with the observed data.

Table 3 shows the results of these calculations for one of the measured sites, while Fig. 4 illustrates the calculated model.

We present three separate soundings, each from different ice stations, as well as predicted sounding curves from Archie's law with $a{=}1$ and $m{=}1.9$, and with $a{=}8.6$ and $m{=}2.75$. In the first case we see a similar departure from Archie's law as mentioned in the previous section. That is, when we have higher brine volume fractions ($\phi > 5\%$), Archie's law with $a{=}1$ tends to underestimate the conductivity and thus overestimate the resistivity. For lower brine volume fractions we see the predicted curve significantly underestimate the measured sounding curve. When using $a{=}8.6$, however, we see a predicted curve which tends to be much closer to the actual sounding curve determined from the measurements in both cases.

Table 3

A six layer model, with the 6th layer being the ocean, where ice resistivity and layer thickness are calculated from brine volume fraction measurements using the model $F(\phi) = 8.6\phi^{2.75}$ to calculate the mean resistivities as discussed in this section with $f{=}0.43$. These measurements come from station 13 and are shown in the left of Fig. 4. * The thickness of the first layer is determined by the preliminary three layer inversion.

Core section (m)	ϕ	l (m)	$f \cdot l$ (m)	ρ_m^* (Ω m)
0-0.05	0.14	0.05	*	4.53
0.05-0.1	0.14	0.05	0.0215	13.2
0.1-0.2	0.09	0.1	0.43	49
0.2-0.3	0.11	0.1	0.43	32
0.3-0.41	0.19	0.1	0.47	9.2

In Fig. 4, we show the results from station 13 where the brine volume fraction ranged from $\phi = 0.09$ to 0.22, all above the critical threshold. In this case we would expect that when $a{=}1$ and $m{=}1.9$, we should underestimate the conductivity since we are above the critical threshold, or overestimate the resistivity. This case is shown on the left where we do in fact see overestimation. When we apply Archie's law with $a{=}8.6$ and $m{=}2.75$, we do not see the same overestimation and the overall shape of the predicted curve matches more closely that of the data, implying that a percolation approach may better represent the actual vertical conductivity.

In Fig. 5, we show the results from station 5 where the brine volume fraction ranged from $\phi = 0.04$ to 0.07, all close to the critical threshold. In this case, we should expect that when $a{=}1$ and $m{=}1.9$ we would see an overestimation of the conductivity and thus an underestimation of the resistivity. In fact, in this case we do see an underestimation of the resistivity as shown on the left in Fig. 5. When we apply Archie's law with $a{=}8.6$ and $m{=}2.75$ we see a much better fit.

In Fig. 6, we show the results from station 6 where the brine volume fraction ranged from $\phi = 0.07$ to 0.22. For this we would expect much the same behavior as for station 13 with $a{=}1$ and $m{=}1.9$ with overestimation of the resistivity due to the range of brine volume fractions. However, we see a large underestimation. This can be understood since the conductivity values for this station are some of the highest values of the conductivity for given brine volume fractions. Thus, the associated resistivities are the lowest, which would give a large underestimation of the sounding curve. When $a{=}8.6$ and $m{=}2.75$, we do obtain sightly higher values which put us closer to the actual curve. However, we still have an underestimation, which may be the result of granular ice where anisotropy is not as pronounced.

This method for predicting a sounding curve works well provided that the appropriate value of m is used in Archie's Law. The best results are obtained when the value of m used correlates most closely with percolation theory. The above comparison is useful as it allows us to compare our models from our direct measurements to a different data set. The fact that we see the same behavior as in the previous sections reinforces our conclusions.

In the previous sections we have used various models derived from direct measurements of vertical conductivity (Golden et al.,

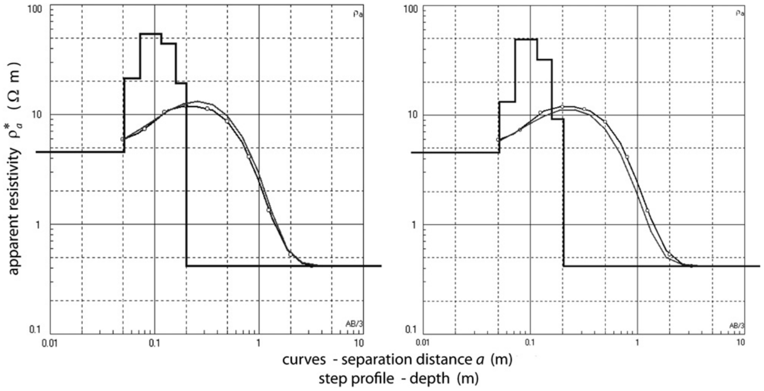

Fig. 4. Ice station 13. Left: predicted curve with $a{=}1$ and $m{=}1.9$ and actual measured curve showing overestimation in the higher brine volume fraction range. Right: predicted curve with $a{=}8.6$ and $m{=}2.75$ showing close agreement with a slight underestimation.

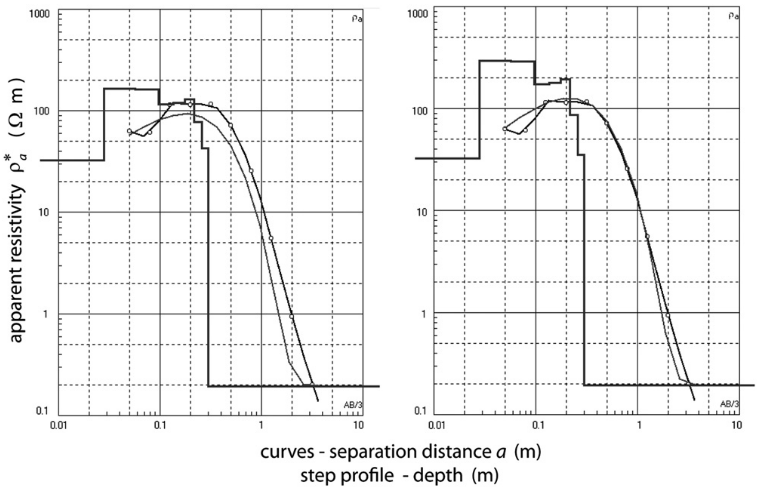

Fig. 5. Ice station 5. Left: predicted curve with $a=1$ and $m=1.9$ and actual measured curve showing underestimation in the lower brine volume fraction range. Right: predicted curve with $a=8.6$ and $m=2.75$, showing closer agreement with the measured curve.

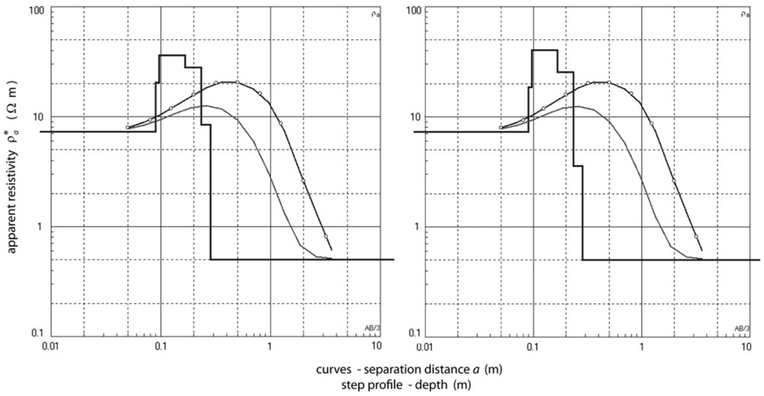

Fig. 6. Ice station 6. Left: predicted curve with $a=1$ and $m=1.9$ and actual measured curve showing large underestimation in resistivities probably due to the microstructure of the ice. Right: predicted curve with $a=8.6$ and $m=2.75$ showing slightly closer agreement. The underestimation may be a result of granular ice.

in preparation) and brine volume fraction to construct a prediction of what a Wenner sounding curve should look like at a given site. The close agreement of the predicted curves with actual soundings suggests that these theoretical curves could serve as a regularization model to aid in the construction of an n-layer resistivity profile of sea ice that represents the actual conditions.

Using the predicted model given by $F=8.56\phi^{2.75}$ to regularize the inversion problem, by least squares methods, we have constructed a 6-layer vertical resistivity profile for Ice Station 13. In the figure the 6th layer is the ocean which is not depicted. In this particular case we fix the total thickness of the ice as it is known from a core sample. In a case where the actual thickness was not known, an estimate can be made using the factor of anisotropy and the thickness given from the 3-layer inversion as discussed in the previous sections. Upon completion of the inversion, the vertical resistivity of each layer can be recovered by multiplying its apparent resistivity ρ_a by the factor of anisotropy f. The correct thickness of the layer can be obtained by dividing the inverted height h by f. Once this is done the actual values can be plotted.

We compare the predicted model with the inverted model in Fig. 7. It is apparent from the figure that the predicted and inverted profiles have similar structure suggesting a good estimate by the model. The main difference between the predicted (dashed) and inverted (solid) profiles is higher resistivity given by the inversion. This can be related back to Fig. 4, as the model shown on the left slightly underestimates ρ_a for Station 13.

The 6-layer inversion in Fig. 7 illustrates the subtle changes in resistivity of ice which go unnoticed in standard 3-layer models. Understanding how the resistivity changes with depth at a higher resolution may lead to more accurate models in mounted EM sounding techniques such as shipborne or airborne EM devices which currently model sea ice using only 3-layers.

It should be noted that we had available a detailed brine volume and temperature profile to use with our model. However, in principle one could use a temperature profile to estimate both brine volume fraction and brine conductivity with depth which can then be used to generate a regularization model. To illustrate the usefulness of even a less accurate, but still reasonable, regularization model in producing a realistic inverted profile, we introduce a 10% random error into the predicted model and repeat our inversion scheme using this less accurate model for regularization then compare this to the inversion result from the original predicted model in Fig. 8. It can be seen from Fig. 8 that the result, while not exactly the same, is not very different from that using a more accurate regularization model and shares the same overall distribution of resistivities. This is in contrast to the result obtained when not using a reasonable regularization model, i.e., a model not based on the actual properties of the ice, which we illustrate in Fig. 9. The result in Fig. 9 was obtained by dividing the middle layer from a simple 3-layer inversion into 4 equal pieces in both depth and resistivity while leaving the top layer and bottom layer alone, creating a hap-hazard 6-layer model to be used for regularization. We then invert using this model and compare the result to that when using the best predicted model. As can be seen in Fig. 9 the results of the two inversions are completely different, yet both will produce a forward model which fits the Wenner sounding curve well. In this way it can be seen how important it is to have a reasonable regularization model to prevent extraneous solutions which do not accurately represent the sea ice.

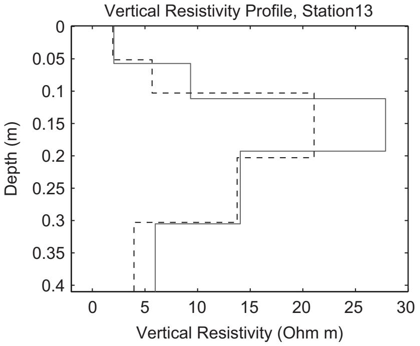

Fig. 7. The predicted (dashed) and inverted (solid) vertical resistivity profile for a 6-layer inversion of station 13 with depth. The x-axis is the resistivity while the y-axis is positively directed downward showing depth. The similar structure between the two suggests the predicted model is a good estimate.

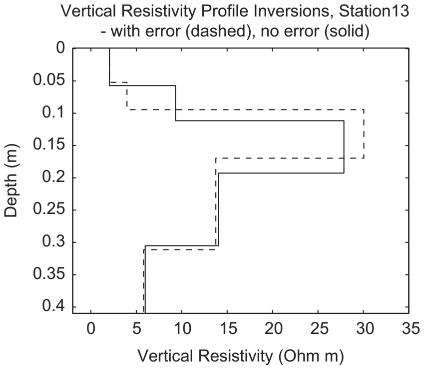

Fig. 8. Inverted vertical resistivity profiles from the predicted model with (dashed) and without (solid) an introduced 10% random error in the regularization model. From this figure the use of a regularization model in preserving the shape of a profile is illustrated.

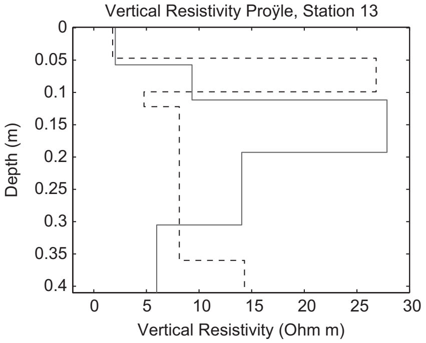

Fig. 9. Inverted vertical resistivity profiles with regularization (solid) and without (dashed). It can be seen that while both profiles produce sounding curves which match the sounding data their overall structure is quite different.

4. Conclusions

We have made indirect measurements of the electrical conductivity of Antarctic sea ice. We used Wenner array soundings to measure the apparent conductivity as a function of separation, yielding information about the conductivity profile with depth. We developed an *n*-layer inversion scheme to reconstruct the profiles from the Wenner array data, which relies on a regularization technique based on conductivity models for sea ice. Our work helps to provide a rigorous basis for the interpretation of thickness soundings, but also yields information about the conductivity of sea ice with depth. Such information, when combined with other work relating fluid and electrical transport properties, helps lay the groundwork for monitoring fluid processes in sea ice which are important in climate studies.

Acknowledgments

We are very grateful for the support provided by the Division of Mathematical Sciences and the Arctic Natural Sciences Program at the US National Science Foundation (NSF). Adam Gully was supported by the NSF Research Experiences for Undergraduates (REU) Program and an NSF VIGRE graduate fellowship, and Christian Sampson was supported by the NSF REU Program. We thank Joyce Lin for providing Fig. 2 illustrating the electric current streamlines for the Wenner array. We also thank the Australian Antarctic Division and the crew of the *Aurora Australis* for their help and support during the SIPEX Antarctic expedition.

References

Archie, G.E., 1942. The electrical resistivity log as an aid in determining some reservoir characteristics. Trans. Am. Inst. Min. Metall. Pet. Eng. 146, 54–64.

Bergman, D.J., 1978. The dielectric constant of a composite material—a problem in classical physics. Phys. Rep. C 43, 377–407.

Bhattacharya, P.K., Patra, H.P., 1968. Direct Current Geoelectric Sounding; Principles and Interpretation. Elsevier Publishing, Amsterdam.

Buckley, R.G., Staines, M.P., Robinson, W.H., 1986. In situ measurements of the resistivity of Antarctic sea ice. Cold Reg. Sci. Technol. 12, 285–290.

Frankenstein, G., Garner, R., 1967. Equations for determing the brine volume of sea ice from -0.5° to -22.9°C. J. Glaciol. 6, 943–944.

Fritsen, C.H., Lytle, V.I., Ackley, S.F., Sullivan, C.W., 1994. Autumn bloom of Antarctic pack-ice algae. Science 266, 782–784.

Fujino, K., Suzuki, Y., 1963. An attempt to estimate the thickness of sea ice by electrical resistivity method II. Low Temp. Sci. A 21, 151–157.

Golden, K., 1986. Bounds on the complex permittivity of a multicomponent material. J. Mech. Phys. Solids 34, 333–358.

Golden, K., Papanicolaou, G., 1983. Bounds for effective parameters of heterogeneous media by analytic continuation. Commun. Math. Phys. 90, 473–491.

Golden, K.M., Ackley, S.F., 1981. Modeling of anisotropic electromagnetic reflection from sea ice. J. Geophys. Res. (Oceans) 86, 8107–8116.

Golden, K.M., Ackley, S.F., Lytle, V.I., 1998a. The percolation phase transition in sea ice. Science 282, 2238–2241.

Golden, K.M., Cheney, M., Ding, K.H., Fung, A.K., Grenfell, T.C., Isaacson, D., Kong, J.A., Nghiem, S.V., Sylvester, J., Winebrenner, D.P., 1998b. Forward electromagnetic scattering models for sea ice. IEEE Trans. Geosci. Remote Sensing 36, 1655–1674.

Golden, K.M., Eicken, H., Gully, A., Ingham, M., Jones, K.A., Lin, J., Reid, J., Sampson, C., Worby, A.P. Critical behavior of electrical transport in sea ice. In preparation.

Golden, K.M., Eicken, H., Heaton, A.L., Miner, J., Pringle, D., Zhu, J., 2007. Thermal evolution of permeability and microstructure in sea ice. Geophys. Res. Lett. 34, L16501. doi:10.1029/2007GL030447 (6 pages and issue cover).

Gully, A., Backstrom, L.G.E., Eicken, H., Golden, K.M., 2007. Complex bounds and microstructural recovery from measurements of sea ice permittivity. Physica B 394, 357–362.

Haas, C., 1998. Evaluation of ship-based electromagnetic-inductive thickness measurements of summer sea-ice in the Bellingshausen and Amundsen Seas, Antarctica. Cold Reg. Sci. Technol. 27, 1–16.

Haas, C., 2003. Dynamics versus thermodynamics: the sea ice thickness distribution. In: Thomas, D.N., Dieckmann, G.S. (Eds.), Sea Ice: An Introduction to its Physics, Chemistry, Biology and Geology. Blackwell, Oxford, pp. 82–111.

Haas, C., 2004. Late-summer sea ice thickness variability in the Arctic Transpolar Drift 1991-2001 derived from ground-based electromagnetic sounding. Geophys. Res. Lett. 31, L09402. doi:10.1029/2007GL030447.

Haas, C., Gerland, S., Eicken, H., Miller, H., 1997. Comparison of sea-ice thickness measurements under summer and winter conditions in the Arctic using a small electromagnetic induction device. Geophysics 62, 749–757.

Hobbs, P.V., 1974. Ice Physics. Clarendon Press, Oxford.

Ingham, M., Pringle, D.J., Eicken, H., 2008. Cross-borehole resistivity tomography of sea ice. Cold Reg. Sci. Technol. 52, 263–277 10.1016/jcoldregions.2007.05.002.

Jackson, P.D., Smith, D.T., Stanford, P.N., 1978. Resistivity-porosity-particle shape relationships for marine sands. Geophysics 43, 1250–1268.

Jones, K.A., Ingham, M., Pringle, D.J., Eicken, H., 2010. Temporal variations in sea ice resistivity: resolving anisotropic microstructure through cross-borehole dc resistivity tomography. J. Geophys. Res. 115, C11023, doi:10.1029/2009JC006049.

Kovacs, A., Holladay, J.S., 1990. Sea ice thickness measurement using a small airborne electromagnetic sounding system. Geophysics 55, 1327–1337.

Maillet, R., 1947. The fundamental equations of the electrical prospecting. Geophysics 12 (4), 529–556.

Milton, G.W., 1980. Bounds on the complex dielectric constant of a composite material. Appl. Phys. Lett. 37, 300–302.

Milton, G.W., Golden, K., 1990. Representations for the conductivity functions of multicomponent composites. Commun. Pure. Appl. Math. 43, 647–671.

Parasnis, D.S., 1986. Principles of Applied Geophysics, fourth ed. Chapman and Hall, New York.

Perovich, D.K., Gow, A.J., 1996. A quantitative description of sea ice inclusions. J. Geophys. Res. 101, 18327–18343.

Pringle, D.J., Miner, J.E., Eicken, H., Golden, K.M., 2009. Pore-space percolation in sea ice single crystals. J. Geophys. Res. (Oceans) 114, C12017.

Prinsenberg, S.J., Holladay, S., Lee, J., 2002. Measuring ice thickness with EISFlow, a fixed-mounted helicopter electromagnetic-laser system. In: Chung, J.S., Sayed, M., Kashiwagi, M., Setoguchi, T., Hong, S.W. (Eds.), The Proceedings of the 12th International Conference on Offshore and Polar Engineering, Kitakyushu, Japan, vol. 1. International Society of Offshore and Polar Engineers, Cupertino, CA, pp. 737–740.

Reid, J.E., Pfaffling, A., Worby, A.P., Bishop, J.R., 2006. In situ measurements of the direct-current conductivity of Antarctic sea ice: implications for airborne electromagnetic sounding of sea-ice thickness. Ann. Glaciol. 44, 217–223.

Sahimi, M., 1995. Flow and Transport in Porous Media and Fractured Rock. VCH, Weinheim.

Sen, P.N., Scala, C., Cohen, M.H., 1981. A self-similar model for sedimentary rocks with application to the dielectric constant of fused glass beads. Geophysics 46, 781–795.

Serreze, M.C., Holland, M.M., Stroeve, J., 2007. Perspectives on the Arctic's shrinking sea-ice cover. Science 315, 1533–1536.

Stogryn, A., Desargant, G.J., 1985. The dielectric properties of brine in sea ice at microwave frequencies. IEEE Trans. Antennas Propag. AP 33, 523–532.

Thomas, D.N., Dieckmann, G.S. (Eds.), 2003. Sea Ice: An Introduction to its Physics, Chemistry, Biology and Geology. Blackwell, Oxford.

Thyssen, F., Kohnen, H., Cowan, M.V., Timco, G.W., 1974. DC resistivity measurements on the sea ice near pond inlet. Polarforschung 44, 117–126.

Timco, G.W., 1979. An analysis of the in-situ resistivity of sea ice in terms of its microstructure. J. Glaciol. 22, 461–471.

Worby, A.P., Griffin, P.W., Lytle, V.I., Massom, R.A., 1999. On the use of electromagnetic induction sounding to determine winter and spring sea ice thickness in the Antarctic. Cold Reg. Sci. Technol. 29, 49–58.

CHAPTER 7

NETWORK MODELING OF ARCTIC MELT PONDS

In this chapter we develop algorithmic techniques for mapping photographic images of melt ponds onto discrete conductance networks. We explore image processing methods which use mathematical morphology operations to produce conductance matrix representations of images of highly connected melt pond structures. Employing undirected graphs, we are able to map just the melt pond connections. The effective conductivity of these networks can be used to approximate lateral flow between connected ponds. This has relevance as connected ponds allow for the flow of melt water to large drainage features thus changing the albedo of the ice. Chapter 7 is a reprint originally published in *Cold Regions Science and Technology*, **124** (2016) 40-53 with authors **Meenakshi Barjatia, Tolga Tasdizn, Boya Song, Christian S. Sampson, and Kenneth M. Golden.** It is reproduced here with permission of the publisher.

Cold Regions Science and Technology 124 (2016) 40–53

Contents lists available at ScienceDirect

Cold Regions Science and Technology

journal homepage: www.elsevier.com/locate/coldregions

Network modeling of Arctic melt ponds

Meenakshi Barjatia [a], Tolga Tasdizen [a,b,*], Boya Song [c], Christian Sampson [c], Kenneth M. Golden [c]

[a] *Electrical and Computer Engineering, University of Utah, USA*
[b] *Scientific Computing and Imaging Institute, University of Utah, USA*
[c] *Department of Mathematics, University of Utah, USA*

ARTICLE INFO

Article history:
Received 27 February 2015
Received in revised form 14 August 2015
Accepted 28 November 2015
Available online 15 December 2015

Keywords:
Melt ponds
Horizontal conductivity
Mathematical morphology
Graph theory

ABSTRACT

The recent precipitous losses of summer Arctic sea ice have outpaced the projections of most climate models. A number of efforts to improve these models have focused in part on a more accurate accounting of sea ice albedo or reflectance. In late spring and summer, the albedo of the ice pack is determined primarily by melt ponds that form on the sea ice surface. The transition of pond configurations from isolated structures to interconnected networks is critical in allowing the lateral flow of melt water toward drainage features such as large brine channels, fractures, and seal holes, which can alter the albedo by removing the melt water. Moreover, highly connected ponds can influence the formation of fractures and leads during ice break-up. Here we develop algorithmic techniques for mapping photographic images of melt ponds onto discrete conductance networks which represent the geometry and connectedness of pond configurations. The effective conductivity of the networks is computed to approximate the ease of lateral flow. We implement an image processing algorithm with mathematical morphology operations to produce a conductance matrix representation of the melt ponds. Basic clustering and edge elimination, using undirected graphs, are then used to map the melt pond connections and reduce the conductance matrix to include only direct connections. The results for images taken during different times of the year are visually inspected and the number of mislabels is used to evaluate performance.

1. Introduction

Sea ice is a critical component of Earth's climate system and a sensitive indicator of climate change. The dramatic losses of summer Arctic sea ice observed in the past few decades have a substantial impact on Earth's climate system, yet most global climate models have significantly underestimated the rate of decline (Boé et al., 2009; Serreze et al., 2007; Stroeve et al., 2007). One of the fundamental challenges of climate science is to develop more rigorous representations of sea ice in climate models and to incorporate important small scale processes and structures into these large scale models. For example, during the melt season the Arctic sea ice cover becomes a complex evolving mosaic of ice, melt ponds on the sea ice surface, and open water. While white snow and ice reflect most incident sunlight, melt ponds and the ocean absorb most of it. The overall reflectance or albedo of sea ice floes – the ratio of reflected to incident sunlight – is determined by the evolution of melt pond coverage and geometry (Perovich et al., 2002; Polashenski et al., 2012; Scott and Feltham, 2010). As melting increases, the albedo is lowered, which increases solar absorption, leading to more melting, and so on. This key mechanism is called *ice–albedo feedback* (Curry et al., 1995), and has played a significant role in the decline of the summer Arctic ice pack (Perovich et al., 2008; Pistone et al., 2014). Sea ice albedo is a significant source of uncertainty in climate projections and one of the most important parameters in climate modeling (Flocco et al., 2010; Pedersen et al., 2009; Polashenski et al., 2012; Scott and Feltham, 2010).

While melt ponds form a key component of the Arctic marine environment, comprehensive observations or theories of their formation, coverage, and evolution remain relatively sparse. Available observations of melt ponds show that their areal coverage is highly variable. This is particularly true for first year ice early in the melt season, with rates of change as high as 35% per day (Polashenski et al., 2012; Scharien and Yackel, 2005).

Such variability, as well as the influence of many competing factors controlling melt pond and ice floe evolution, makes the incorporation of realistic treatments of albedo into climate models quite challenging (Polashenski et al., 2012). Small and medium scale models of melt ponds which include some of these mechanisms have been developed (Flocco and Feltham, 2007; Scott and Feltham, 2010; Skyllingstad et al., 2009), and melt pond parameterizations are being incorporated into global climate models (Flocco et al., 2010; Flocco et al., 2012; Hunke and Lipscomb, 2010; Hunke et al., 2013; Pedersen et al., 2009).

As melting progresses during the season, the evolution of melt ponds from small isolated structures into large interconnected networks is responsible for a number of processes that help control the rate at which the ice pack melts. It is believed (Hohenegger et al., 2012) that this evolution of connectedness is an example of a percolation transition

---

* Corresponding author at: Electrical and Computer Engineering, University of Utah, USA. Tel.: +1 801 581 3539.
E-mail address: tolga@sci.utah.edu (T. Tasdizen).

http://dx.doi.org/10.1016/j.coldregions.2015.11.019
0165-232X/

(Christensen and Moloney, 2005; Stauffer and Aharony, 1992). Such a transition occurs when one phase in the microstructure of a composite material, for example, becomes connected on macroscopic scales as a controlling parameter exceeds a critical value called the *percolation threshold* (Broadbent and Hammersley, 1957; Christensen and Moloney, 2005; Stauffer and Aharony, 1992).

In the case of melt ponds the controlling parameter which gives rise to critical behavior is thought to be the fraction of the area of the sea ice surface covered by melt ponds.

An important example of critical behavior related to percolation theory as applied to sea ice, and important for melt pond drainage, comes from the study of fluid flow through the porous microstructure of sea ice. Specifically, the brine microstructure displays a percolation threshold at a critical brine volume fraction of around 5 % in columnar sea ice (Golden et al., 1998; Golden et al., 2007; Pringle et al., 2009), which corresponds to a critical temperature $T_c \approx -5\ ^\circ$C for a typical bulk salinity of 5 ppt. Below this threshold the brine phase of the sea ice consists primarily of isolated, disconnected pockets. It is only above the threshold where the brine phase becomes connected over large scales. This threshold acts as an on-off switch for fluid flow through sea ice, and is known as the *rule of fives*. It leads to critical behavior of fluid flow, where sea ice is effectively impermeable to fluid transport for brine volume fractions below 5 % and increasingly permeable for volume fractions above 5 %.

In addition to identifying the critical behavior of fluid transport in sea ice, the percolation theory of fluid and electrical transport through lattices (Christensen and Moloney, 2005; Stauffer and Aharony, 1992) was used to produce models of the fluid permeability of sea ice as a function of brine volume fraction (Golden et al., 2007). In this work X-ray computed tomography images of the brine microstructure of sea ice were analyzed and mapped onto random graphs of nodes and edges, in order to establish the percolative behavior of the system (Golden et al., 2007; Pringle et al., 2009), and the rule of fives in particular.

Other types of network models have also been used to describe both fluid and electrical transport in the brine phase of sea ice. For example, in the random pipe model, the diameters of random pipes, which represent brine channels in the ice, are chosen from lognormal probability distributions that describe the cross-sectional areas of the brine inclusions in sea ice and then assigned to the edges in a square lattice (Zhu et al., 2006). The fluid permeability of the model is then computed by using a random resistor network representation of the system and employing a fast multigrid method to find its effective conductivity which can then be related to the permeability. This same approach can also be used to directly model the electrical conductivity of the ice, an important parameter in remote sensing of sea ice thickness, fluid transport properties, and microstructural transitions (Addison, 1969; Buckley et al., 1986; Fujino and Suzuki, 1963; Ingham et al., 2008; Reid et al., 2006; Thyssen et al., 1974). Network models have been used extensively in analyzing the transport properties of composite materials (Milton, 2002; Torquato, 2002).

It has been suggested that percolative behavior occurs for melt ponds on the sea ice surface, As they cover more of the surface, disconnected, isolated ponds begin to evolve into large connected structures with complex boundaries, presumably achieving large scale connectivity above a critical area fraction (Hohenegger et al., 2012).

Increased connectivity of melt ponds promotes further melting through increased heat transport, contributes to the break-up of ice floes, and allows increased horizontal transport of meltwater toward drainage avenues such as large vertical brine channels, cracks, leads, and seal holes (Polashenski et al., 2012; Scharien and Yackel, 2005). Other melt pond models including both vertical and horizontal transport of melt water, such as a type of cellular automata, have been developed elsewhere, as in Scott and Feltham (2010).

In this work we begin to develop techniques for network modeling of melt ponds, their connectivity, and horizontal flow characteristics. Some of the groundwork for this type of modeling was laid in Hohenegger et al. (2012). Images of melting Arctic sea ice collected during two Arctic expeditions – the 2005 Healy-Oden Trans Arctic Expedition (HOTRAX) (Perovich et al., 2009) and the 1998 Surface Heat Budget of the Arctic Ocean (SHEBA) expedition (Perovich et al., 2002) – were analyzed for area–perimeter data on thousands of individual melt ponds. Algorithmic methods of distinguishing melt ponds from the ocean in leads between the sea ice floes were developed. This data was used to discover that pond fractal dimension transitions from 1 to 2 around a critical length scale of 100 m^2 in area (Hohenegger et al., 2012). Pond complexity was found to increase rapidly through the transition as smaller ponds coalesce to form large connected regions, reaching a maximum for ponds larger than about 1000 m^2 whose boundaries resemble space filling curves.

In earlier work on melt ponds and sea ice albedo, image processing has been used to measure the area fractions of melt ponds and leads from aerial and satellite images. In Perovich et al. (2002) these area fractions from June to October, using SHEBA images taken in 1998 (Perovich et al., 2002), show how the area fraction of melt ponds increases as summer progresses, and starts decreasing again at the end of summer as new ice forms. A probability distribution for the size of melt ponds is also derived from the data, which depends on the progress of the melt season.

In the work reported here, the connectivity of these melt pond networks is determined using aerial images of Arctic sea ice from the SHEBA and HOTRAX databases. We develop an algorithmic method of mapping a configuration of melt ponds onto a graph of nodes and edges. These melt pond configurations may be disconnected individual components, or partially or completely connected across an image. The edges are assigned values which indicate the width of "bottlenecks" separating larger pools of melt water, which are identified with the nodes of the graph.

The horizontal flow of water between melt ponds depends on the narrowest bottlenecks between them and the width of these bottlenecks is inversely proportional to the fluid conductance between them.

Mathematical morphology based image processing techniques (Gonzalez and Woods, 2008) are used with a clustering algorithm and graph theory to find a conductance graph associated with each melt pond configuration studied. Further work will explore the relationship of these graphs and associated conductance networks with the actual flow of fluid in the pond network, and the effect on sea ice albedo.

2. Method

The images of melt ponds from the SHEBA and HOTRAX expeditions are in color. The intensity and color of each pixel in the image are encoded using the intensities of the Red, Green and Blue colors that make up each pixel. The image is represented as a matrix of pixels, with each pixel being a vector of three variables — red, green and blue color values. These are called, respectively, the red, green and blue channels of the image.

These images are converted to gray-scale to reduce each pixel to only one intensity and lessen the number of computations required. The gray scale image is derived using the red channel as we see the largest difference between ice and water there.

A simple thresholding operation, as described in the Appendix A, is sufficient to segment the melt pond water from ice and produce a binary image. Otsu's method (Gonzalez and Woods, 2008) is used to determine this threshold individually for each image, which is then segmented based on this threshold. Fig. 1 shows a histogram of the intensity levels of a gray-scale aerial image with Otsu's threshold. After having segmented water from ice, it is also possible to use the blue color intensity in the images to distinguish between the ocean water leads and melt pond water. However, in this paper, we have selected images that do not contain any ocean water leads.

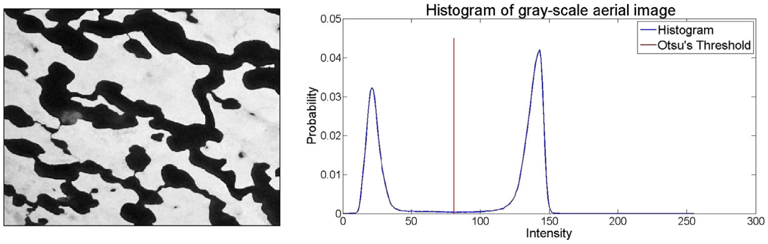

Fig. 1. An aerial grayscale image of melt ponds from HOTRAX is shown on the left, with horizontal scale of about 80 m. A histogram of red channel intensities of the image is shown on the right. The bi-modal distribution is evident and Otsu's threshold, marked on the histogram, can be used to separate melt ponds and ice.

The images used are cropped from those in the SHEBA and HOTRAX databases, which have dimensions around 865 × 770 pixels. The size of the images does not affect the algorithm as long as the resolution remains the same. Only the processing time varies with image size. In this paper we calculate the sizes of ponds and bottlenecks only in terms of pixels. The number of pixels could be converted to a physical scale by knowing the helicopter altitude, camera characteristics, and so on, or if there were an object of known size, such as a ship, in the image. This information can be different for each image used, thus our focus here on pixel size. However, in Fig. 1 the horizontal scale of the image is about 80 m.

2.1. Preprocessing the image

The binary image produced by Otsu's method can have small pieces of ice floating in the melt ponds, melt ponds that are too small to provide much information, and other small artifacts due to noise. These can clutter up the final connectivity graph with unnecessary data. Basic mathematical morphology operations involving erosion and dilation as described in Gonzalez and Woods (2008) and Appendix A are used to clean up the image.

A predetermined mask or structuring element of fixed size is centered at each pixel of the image and only those pixels, at which the structuring element fits inside the original image, are set to one. So, if a 3 × 3 structuring element is used, it will remove the outermost layer of pixels from the foreground, a 5 × 5 structuring element would remove two layers and so on. Morphological dilation is a complementary process where all those pixels, at which the intersection between the structuring element and the image is non-zero, are set as one. Dilation by a 3 × 3 structuring element would cause the foreground to grow another layer of pixels. Opening involves erosion followed by dilation with the same structuring element and is used to remove smaller structures from the foreground like protrusions and narrow connections. Closing on the other hand is dilation followed by erosion and it fills in small gaps in the foreground. Geodesic opening or closing involves finding the intersection of the result of opening or closing with the original image to preserve the shape of the image. The image is first cleaned up using geodesic opening of melt ponds to remove inconsequential melt ponds and geodesic closing to remove floating ice. Circular masks, as shown in Fig. 14, are used for these processes to maintain the curvy shapes of ponds. The mask size can be adjusted as desired. Here a 3 × 3 mask, like the first image in Fig. 14, is used. Note that care should be taken to ensure that the mask size is at least smaller than the narrowest bottleneck in the image, otherwise this connection will be lost.

2.2. Isolating melt ponds

The previous step results in large interconnected melt pond networks. The next step is to find individual melt ponds. First, connected components described in Appendix A are used to find all the separate unconnected melt pond networks and label each uniquely as X_i where $1 \le i \le N_{max}$. Here, N_{max} is the number of unconnected melt pond networks in the image.

Each of these networks is then eroded progressively with a 3 × 3 circular mask. Every erosion iteration scrapes away the outermost layer of pixels from the melt pond network image and the connections between the melt ponds gets narrower and some connections may break. In other words, at each erosion, some ponds might break away from the main network. These can be identified from an increase in the number of unconnected regions in the image, which are found using connected components. The j^{th} region that breaks away from the network X_i is labeled as X_{ij}. This can be an individual melt pond or a smaller network of melt ponds. The connection strength of the separated region X_{ij}, to its parent network X_i, is proportional to the number of erosion iterations after which it breaks away. Each of these smaller melt pond networks X_{ij} is further eroded in a similar manner. The aim is to continue this until all the networks have broken down into their individual components, i.e., to separate out all the individual melt ponds.

Depending on the season in which the photographs are taken and the resolution of the photographs, we can find the expected largest bottlenecks in the melt pond network empirically by performing the above erosion steps repeatedly until all the connections between melt ponds are broken. This was done for a sample image in each image set in Table 1. Knowing that a 3 × 3 circular mask erodes two layers of pixels from the bottleneck — one from each side, we can calculate the number of erosion iterations that are needed to break the network into

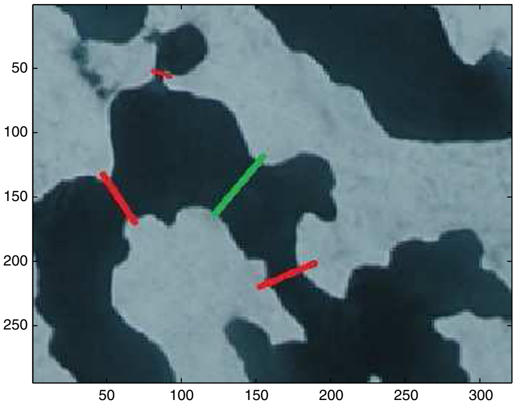

Fig. 2. The red lines indicate constricted regions that should be marked as a boundary between two different melt ponds. The green line indicates a region that is simply a part of one large melt pond but might be treated as a divider between two different melt ponds because it is slightly constricted. (For interpretation of the references to color in this figure legend, the reader is referred to the web version of this article.).

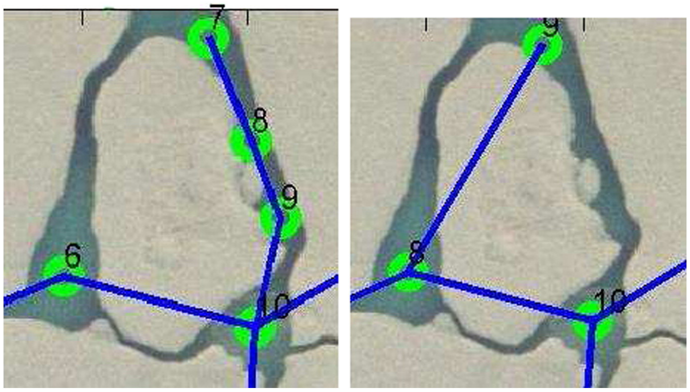

Fig. 3. The connection between melt ponds is incorrectly labeled in the image on the left. Ponds 7 and 10 are connected by a long channel but the image shows the presence of two additional melt ponds due to the constrictions present in the channel. The image on the right uses the constriction ratio to determine that these constrictions are too wide in comparison to the surrounding area to be labeled as separate melt ponds. Hence, it correctly labels two separate melt ponds — 9 and 10.

individual ponds. For example, if the widest bottleneck is 60 pixels across, 30 erosions are required. So the repeated erosions defined above are performed until this maximum bottleneck size is reached. After this maximum bottleneck size is reached in the above connected components process, it is assumed that all the remaining melt ponds are individual ponds and not networks of smaller melt ponds.

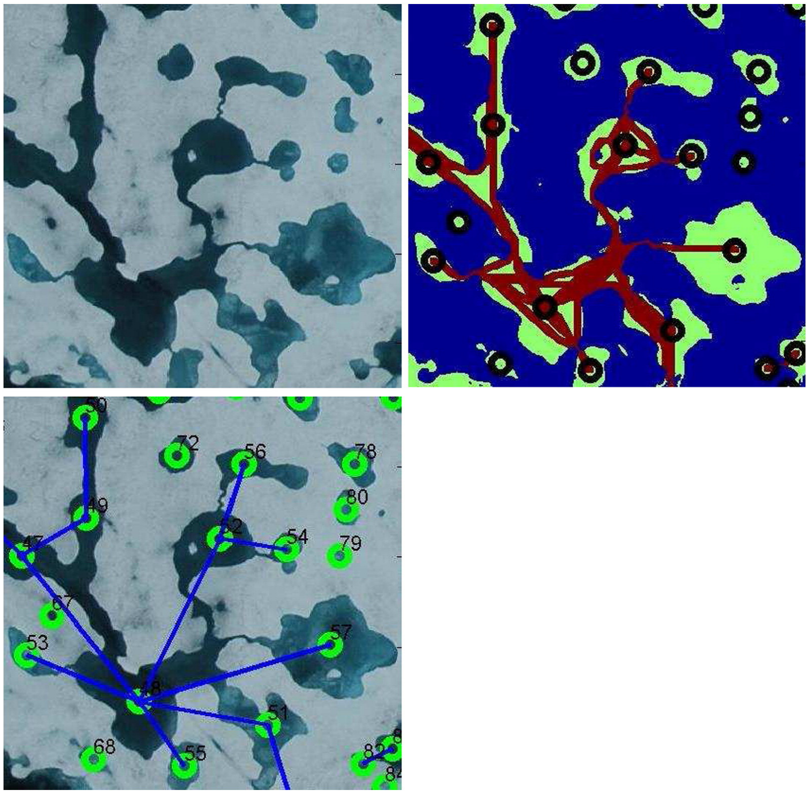

Fig. 4. The first figure on the top left is the input image used. The second figure on top-right shows geodesic distances between melt pond nodes; this figure is a binary version of the first figure — blue is ice, green is water and maroon shows the smallest geodesic paths between nodes. The third figure on the bottom shows the final connections obtained after edge elimination.

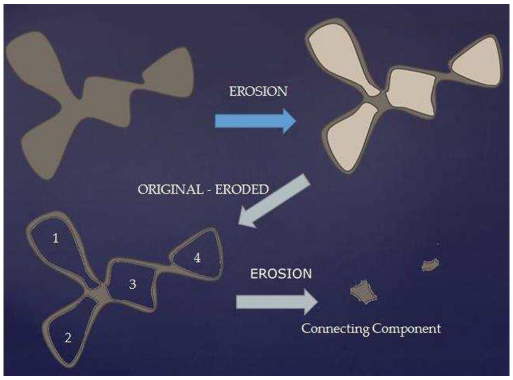

Fig. 5. Here we show how the connecting components between the separated (after erosion) melt ponds are generated after subtracting the eroded image from the original image, to obtain the layer that was peeled away, followed by erosion to isolate just the connecting components between the melt ponds. These connecting components can then be used to determine how well the individual ponds were connected to each other.

Consider the image in Fig. 2. Here, the red lines indicate bottleneck regions and should be eroded away eventually as they are connections between melt ponds. The green line indicates a region that is slightly constricted, but cannot be considered as a bottleneck as it is large relative to the pond surrounding it. Simply performing erosions as described above would eventually break all of these connections. To prevent this, we consider a so-called *constriction ratio*, *CR*, defined as

$$CR = \frac{\text{pond area}}{\text{bottleneck size}}.$$

It was empirically found that a constriction ratio of $CR_{min} = 20$ worked well with the images used in this paper. During any erosion step, if a network under consideration has a constriction ratio CR such that $CR < CR_{min}$, then this is probably a melt pond and should not be broken down any further. Another example of this is shown in Fig. 3. The image on the left shows the melt pond network that is obtained without using the constriction ratio. It can be seen that the ponds that are labeled 8 and 9 in this image are just a part of the long channel that connects ponds 7 and 10. The image on the right uses the constriction ratio and correctly labels the ponds.

2.3. Connections between melt ponds

The last part of the problem is finding the conductances between the individual melt ponds. As already described in the previous section, this is done while the interconnected melt ponds are being separated into smaller melt pond networks. To re-iterate, each erosion with a 3×3 mask removes the outermost pixel layer. Thus two layers of pixels, one from each side of the bottleneck, are removed. If a region separates from the main network at the k^{th} erosion iteration, then the bottleneck joining this region to the network is $2 \times i$ pixels wide.

Until this point, the method has concentrated on grouping the melt ponds that are connected to each other and finding the sizes of bottlenecks between a melt pond and the network to which it belongs. The next step in the algorithm is to find out exactly which melt ponds are connected to each other and represent them using undirected graphs.

The problem also requires that we find only direct connections between ponds. To understand what this means, let each individual melt pond be a node in an undirected graph. Consider the 3rd image in Fig. 4 which labels each pond as a node. The node 56 is connected to all the nodes from 47 to 55 in this image. However, it is immediately or directly connected only to node 52. We can characterize the connection between nodes 56 and 48 by instead using the connection between modes 56 and 52 followed by connection between nodes 52 and 48.

At each erosion iteration, the interconnected melt pond network splits into a number of smaller ponds in the same erosion step. We have to find out which ponds are directly connected to each other as described above. Two simple methods of doing this would involve the following operations:

(i) morphological dilation (Gonzalez and Woods, 2008),
(ii) a simple clustering approach (Gonzalez and Woods, 2008) followed by a graph theory method (Van Steen, 2010).

In the first method, at each iteration, the eroded image is subtracted from the original image to get only the bottlenecks that were eroded away. This resulting image is then dilated and a simple overlapping operation (using the logical OR function) is performed to check which ponds form a direct connection with each other. This is illustrated in Fig. 5. A major problem with this approach is that sometimes the dilation is not sufficient to cause an overlap with the expected ponds and this leads to incorrect or missing connections.

In the second method, the center of each melt pond pixel-cluster is located using the mean of the cluster with Euclidean distances. One

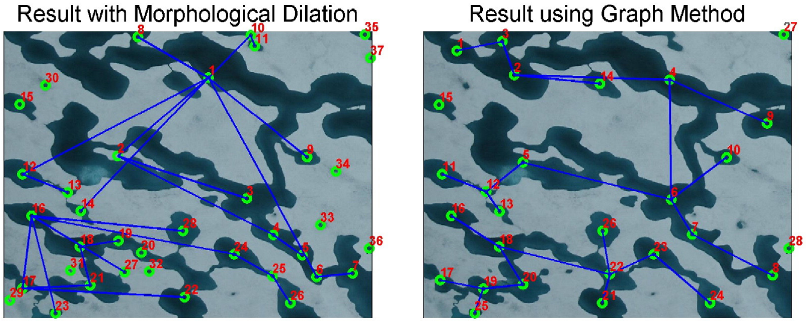
Result with Morphological Dilation
Result using Graph Method

Fig. 6. The image on the left results from using morphological dilation for mapping pond connections. The image on the right uses the clustering and graph method approach. It can be seen that without trying to determine the strongest connection using edge weights in undirected graphs, the connections between melt ponds do not connect the nearest neighbors with each other.

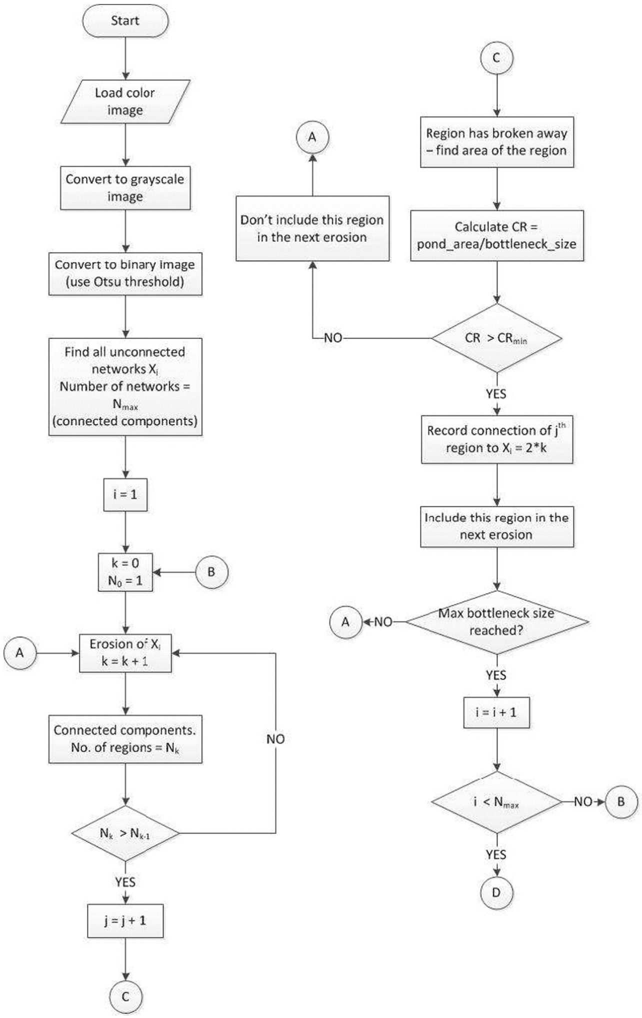

Fig. 7. Flowchart representation of the method.

may try to use k-means clustering on the initial image to separate the ponds, but as this only uses Euclidean distances between pixels and needs a fixed estimate of the number of clusters at the output, it will assign more than one cluster center to larger ponds and may ignore the smaller ponds. The geodesic distances between these cluster centers are calculated. The distance between unconnected ponds is set to infinity because the strength of the connection between two ponds decreases with increasing distance and an infinite distance corresponds to the absence of any connection between ponds. These distances are then used along with the conductance strengths calculated below to construct a graph of the melt pond network.

The nodes of the graph are the cluster centers found above, and all the nodes belonging to connected melt ponds are connected to each other with graph edges. Note that the conductance strength here only refers to the width of the channel connecting different ponds and gives a basis for relative comparison of ease of flow of fluid between these channels. Let the conductance strength between nodes i and j be denoted by σ_{ij} and the geodesic distance between them be d_{ij}. Each edge between two nodes i and j is assigned a weight w_{ij} given by,

$$w_{ij} = \frac{\sigma_{ij}}{d_{ij}} \ . \tag{1}$$

The above equation is analogous to conductance in an electrical circuit, which is directly proportional to conductivity of the wire and inversely proportional to the length of the wire. Between each pair of connected nodes, the direct path and all paths involving only one intermediate connection are considered. For any node, there are $(n-1)$ possible paths to another node, or $(n-2)$ indirect

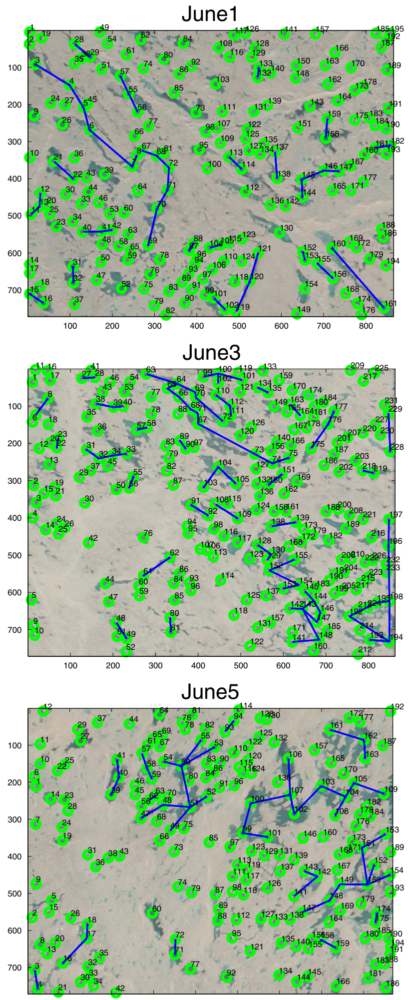

Fig. 8. Melt ponds in June from SHEBA early in the melt season. Here there are no complete connections that go across the entire image, so that the conductivity factors are zero.

paths with one intermediate node and one direct path. The weight of the k th indirect path connecting two nodes is calculated as,

$$w_{ij}^{(k)} = \left(\frac{\sigma_{ik}}{d_{ik}} + \frac{\sigma_{kj}}{d_{kj}}\right), \forall k \neq i, j. \tag{2}$$

Here $\frac{\sigma_{ik}}{d_{ik}}$ is the weight of the edge from node i to node k. The weight of the edge which directly connects nodes i and j is $w_{ij} = \frac{\sigma_{ij}}{d_{ij}}$. Only the path corresponding to the maximum weight between two nodes is retained and all the edges corresponding to other paths are removed. This favors paths which are either very short or have large conductances. At each step, one pair of nodes in the graph is considered. For the next pair, the previously updated connection graph is used so that the edges that no longer exist are not reconsidered. The final step of the algorithm is for node deletion, where the algorithm searches for very small nodes that lie between two or more much larger nodes, and eliminates these small nodes based on a predetermined ratio. This step is performed because, if a really small melt pond lies between two much larger melt ponds, it is probably just a part of the channel connecting the two large melt ponds and should not be labeled as an individual melt pond. For the results presented in this paper, this ratio is empirically set to 20.

The second graph method performs much better for mapping connections than the dilation method. Fig. 6 shows the results obtained using the two different approaches. Consider nodes 5 and 6 at the bottom right corner in the first figure. The connection between the two nodes is not detected because dilation of the connection shown in Fig. 5 is not sufficient to overlap with ponds 5 and 6. Thus, pond 6 is shown connected directly to pond 1. This issue is solved in the second figure by using the clustering and graph method.

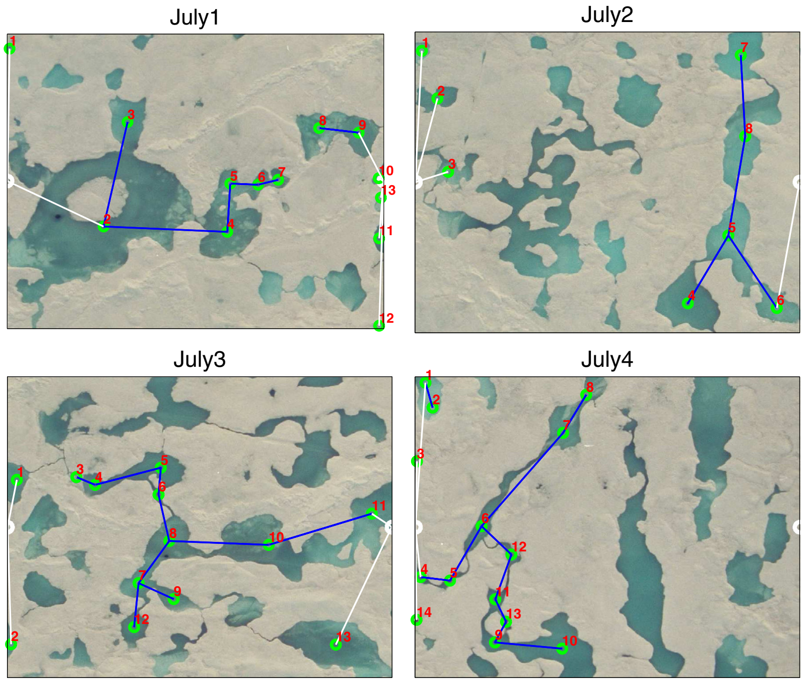

Fig. 9. Melt ponds in July from SHEBA. Here the white nodes are battery nodes. Conductivity factor values are calculated across these battery notes and give an indication of the horizontal fluid conductance from the left to right edge of the image. The white lines represent direct connections to the battery nodes while the blue lines are simply connections between ponds. For the conductivity to be nonzero there must be at least one full connection from left to right. Ponds which do not connect to battery nodes or which do not connect across the image are unlabeled to reduce clutter in the image. (For interpretation of the references to color in this figure legend, the reader is referred to the web version of this article.).

2.4. Conductivity factor calculations

To calculate the horizontal fluid "conductivity", first two battery nodes are added to the left and right of the image. This is analogous to an electrical circuit, where the conductivity between two points can be calculated and the flow of current through the circuit depends on the potential drop across the battery nodes as well as the connectedness and local conductances of the graph representing the circuit. The left battery node is connected to all the ponds touching the left edge of the image with a conductance value of 1 for each connection. The right battery node is similarly connected. The purpose of the battery nodes is to simulate the computation of the effective or equivalent conductivity of a conductor network, which must be subjected to a potential difference, most easily visualized by connecting a battery. The effective conductivity of the network, between these battery nodes, is then measured. The conductivity of very large networks can be calculated approximately by considering smaller sections and then replacing these subsections with their equivalent conductivities in a hierarchical fashion similar to renormalization group techniques (Goldenfeld, 1992). The conductivity of each section could be calculated to create a new, simpler graph model.

To calculate the conductivity between battery nodes, and thus the effective conductivity of the graph with given bond conductivities, let c_{ij} be the conductivity of the edge between nodes i and j, and consider the formulation of the problem of finding the effective conductivity of a graph as found in Golden (1991). Here, each c_{ij} is the normalized edge weight,

$$c_{ij} = \frac{w_{ij}}{\max\limits_{i,j}(w_{ij})}, \quad \forall i, j. \tag{3}$$

Let M be the total number of nodes in the graph, including the two battery nodes. We define the $M \times M$ matrix A such that

$$A_{ij} = -c_{ij}, \quad i, j = 1 \ldots M, i \neq j, \tag{4}$$

$$A_{ii} = \sum_{\forall j: j \neq i} c_{ij} \qquad i = 1 \ldots M. \tag{5}$$

The matrix A' is the $(M-1) \times (M-1)$ array obtained by removing the first row and column of A, which corresponds to the left battery node. Removing the last row and column of matrix A', corresponding to right battery node, gives the $(M-2)(M-2)$ matrix A''. The conductivity factor of the image represented by matrix A, between the battery nodes, is given by Golden (1991) and Mason and Zimmermann (1960)

$$\sigma(A) = \frac{det(A')}{det\left(A''\right)}. \tag{6}$$

It should be noted that the conductivity factor obtained is then related to the fluid permeability of the network, but not equal to the effective conductivity of the network, due to the length scale involved. As noted in the Introduction, further work will explore the relationship of this computed network conductivity to the horizontal fluid flow properties of melt pond configurations. Our goal here is to establish a viable method of transforming images of arrays of melt ponds and map them onto random, labeled graphs. The connectivity and local conductance characteristics of these graphs provide idealized, mathematical models of melt pond connectivity and effective, horizontal flow properties.

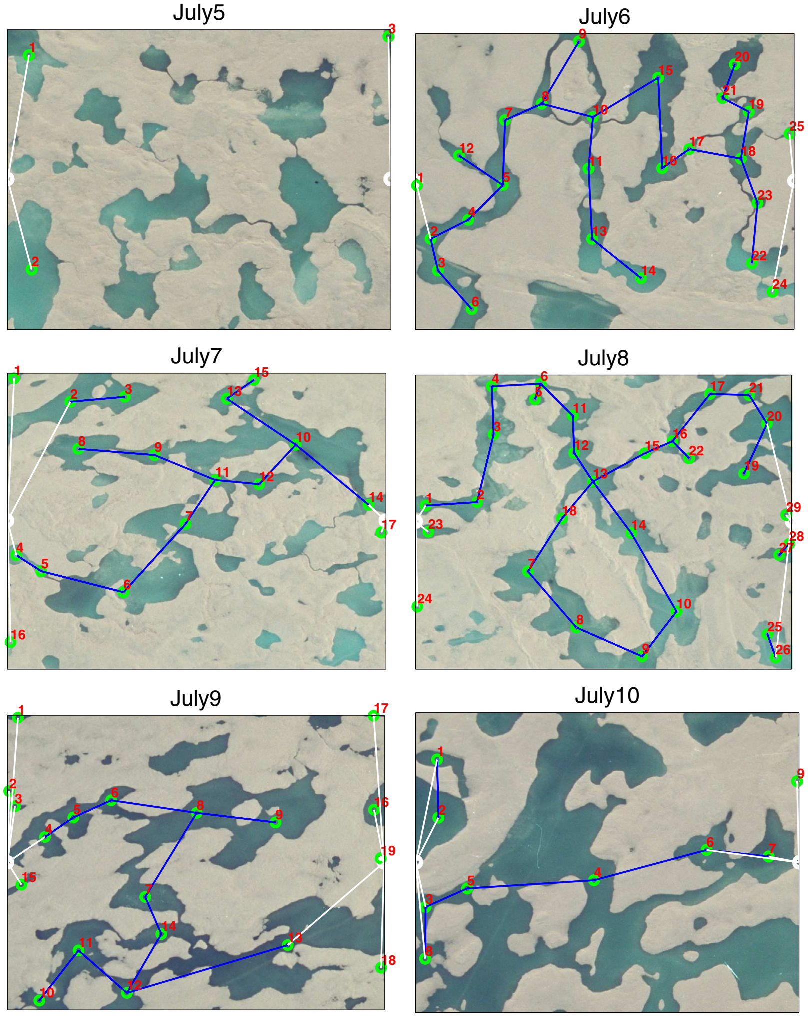

Fig. 10. Continued from Fig. 9, melt ponds in July from SHEBA. Here the white nodes are battery nodes. Conductivity factor values are calculated across these battery nodes and give an indication of the horizontal fluid conductance from the left to the right edge of the image. The white lines represent direct connections to the battery nodes while the blue lines are simply connections between ponds. For the conductivity to be nonzero there must be at least one full connection from left to right. Ponds which do not connect to battery nodes or which do not connect across the image are unlabeled to reduce clutter in the image. (For interpretation of the references to color in this figure legend, the reader is referred to the web version of this article.).

A brief summary of the method discussed in this section is presented in the form of a flowchart in Fig. 7.

3. Results

The above method is used to generate conductance graphs for different sets of images as described in Table 1. MATLAB is used to implement the method summarized above for each of these images.

This method was found to be most useful for images obtained in mid-summer, i.e. July, as the melt ponds are large and interconnected. The average time taken for different sets of images was calculated and is shown in Table 2. The SHEBA images taken in July were processed the quickest, because the images consist of larger and fewer melt ponds. Consequently, the operations involving connected components and the calculation of geodesic distances do not occupy the processor for too long. When these times are compared to the August melt pond images from SHEBA, which have many more melt ponds per image, the computations take much longer. Only about 10% of the computation time is spent in the calculation of geodesic distances and using graph methods to eliminate all but the direct connections between melt ponds. A major part of the computation time is spent in iteratively eroding the image, finding all the connected components and updating the bottleneck widths at each iteration. This can be sped up by using parallel processing for different connected components. Another step in reducing the time latency would be to ignore all ponds that have no other connections. However, this choice would be application specific, as even the isolated ponds may be used to study the evolution of networks with time, because they might, at some point further in time join larger interconnected networks. Table 3 gives a list of the parameters used for different sets of images.

In image processing, ground truth refers to data from images that have already been processed and are known to be correct. Ground truth data are often used to evaluate the performance of an algorithm as they provide a desired solution to the problem under consideration. Due to lack of any ground truth for these images, they are visually inspected to ascertain the performance of the method used. We manually count the number of mislabels and missed connections in each image. A mislabel occurs when a large channel is labeled as a pond or a large pond with a complex morphology may be labeled as 2 or more connected ponds. We find that less than 10 % of labels are obvious mislabels. In terms of calculating the conductance, whether or not a large channel is considered a pond, or one large pond is considered two connected ponds, is less important. It is the connectedness that matters most for this calculation. Missed connections occur when the connection is very small or appears broken in the image. We find that at most 1 in 10 of connections in our images are missed and typically are only missed when pond size is much larger then channel size.

The processed images from July, August and June are shown in Figs. 9, 10, 11, 12 and 8 respectively. Fig. 13 shows the conductance graph obtained for the 3rd image in Fig. 11. The conductivity factors for these figures are shown in Tables 4, 5 and 6. Note that in the images shown in Figs. 9, 10, 11 and 12, the melt ponds that are not part of the network which connects the battery nodes have not been labeled to prevent excess clutter in the figures (these melt ponds do not contribute to the horizontal conductivity calculations). The images shown in Fig. 8 do not have any complete connections that go across the image from left to right. For this reason, unlike the abovementioned figures, the images are shown without removing the melt pond labels which are unconnected to the battery nodes. The conductivity factor values for all these images are zero.

4. Conclusions

Melt ponds play a critical role in determining the albedo of the sea ice pack. Understanding their role in climate processes and incorporating their impact into climate models are fundamental challenges in climate science. In particular, quantifying key characteristics of melt pond geometry and connectivity are critical to quantifying and modeling melt pond growth, decay, and evolution. We have developed here a method of extracting the essential connectivity and scale characteristics of complex melt pond configurations and representing them in a discrete model. We have used image processing techniques in order to map melt ponds onto graphs whose edges represent horizontal flow pathways through the configuration. By computing the effective conductivity of these graphs, we obtain an idealized way of estimating the ease of horizontal flow of meltwater, which is important in melt pond evolution.

After visual inspection, it can be concluded that the algorithm we have developed does a very good job of identifying individual melt ponds, labeling their connections and creating the conductance matrix. More work can be done to improve its speed and remove the few mislabeling errors. The edge elimination method used assigns weights to the edges between nodes (melt pond centers) based on geodesic distance and widths of the connections. The function assigning weights to the edges can be modified and the weights of the nodes (areas of melt ponds) can also be used.

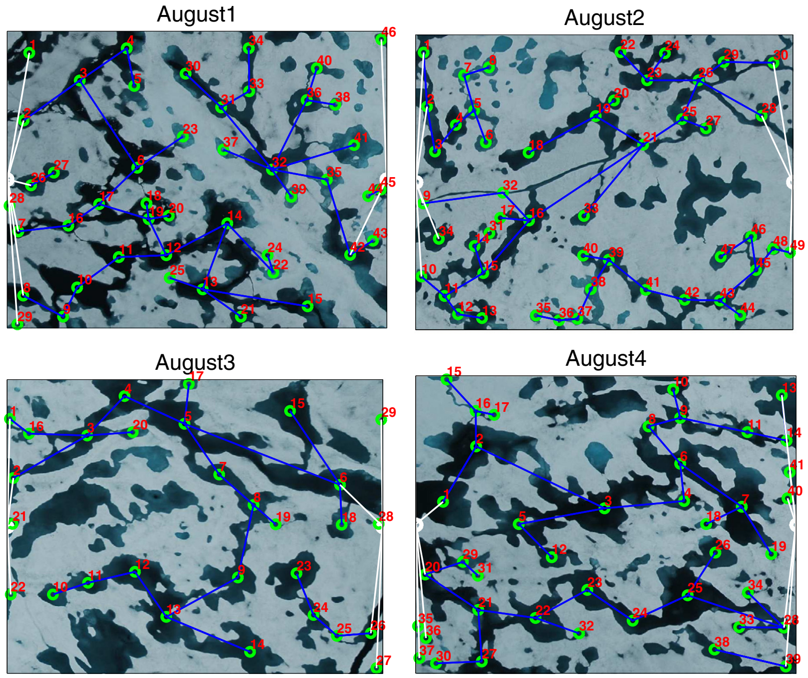

Fig. 11. Melt ponds in August from HOTRAX. It can be seen that there are more parallel paths that exist between the battery nodes compared to both June and July images as the melting has progressed much further, evolving into large interconnected networks. This is also reflected in the data of Tables 4, 5, and 6.

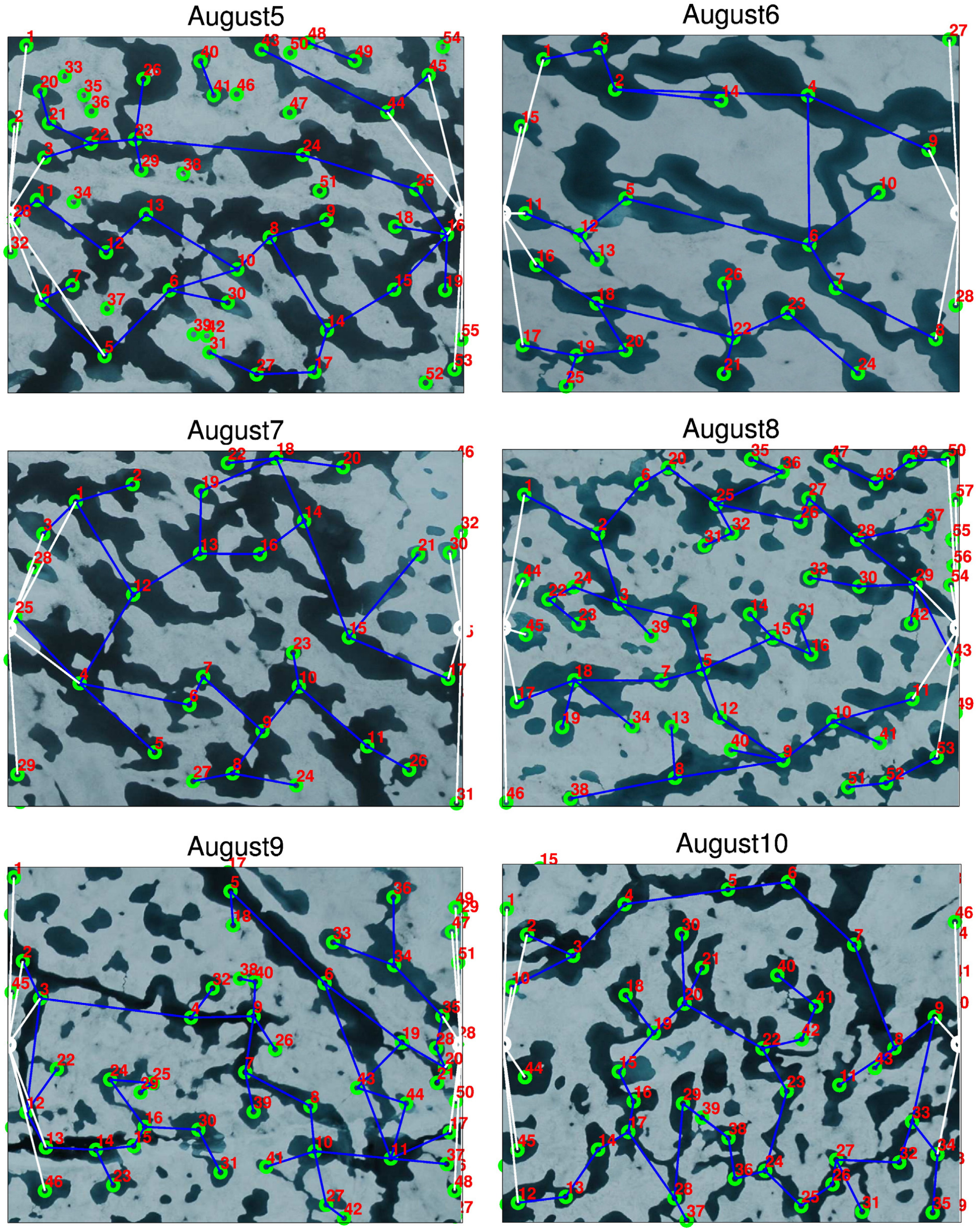

August5

August6

August7

August8

August9

August10

Fig. 12. Continued from Fig. 11, melt ponds in August from HOTRAX. It can be seen that there are more parallel paths that exist between the battery nodes compared to both June and July images as the melting has progressed much further evolving into large interconnected networks. This is also reflected in a the data of Tables 4, 5, and 6.

The work done here can be used to aid in understanding both the horizontal water and heat flow between melt ponds. These are important parameters to consider when modeling melt pond evolution and drainage which are the major controlling factors of ice albedo during the melt season. The conductivity factors calculated can be used to represent effective behavior of the ice–pond composite, and in turn this can be used to develop simpler models of the complex processes which govern melt pond evolution, ultimately to include them in climate models.

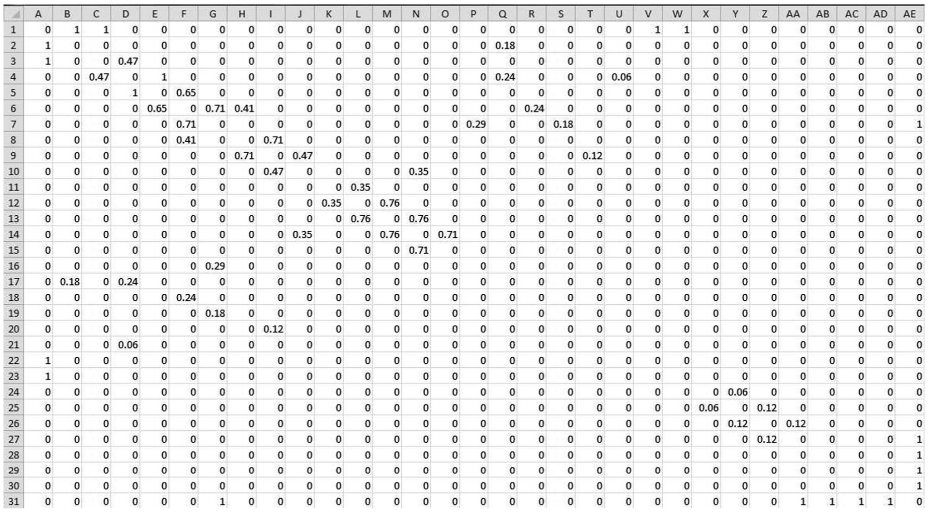

	A	B	C	D	E	F	G	H	I	J	K	L	M	N	O	P	Q	R	S	T	U	V	W	X	Y	Z	AA	AB	AC	AD	AE
1	0	1	1	0	0	0	0	0	0	0	0	0	0	0	0	0	0	0	0	0	0	1	1	0	0	0	0	0	0	0	0
2	1	0	0	0	0	0	0	0	0	0	0	0	0	0	0	0	0.18	0	0	0	0	0	0	0	0	0	0	0	0	0	0
3	1	0	0	0.47	0	0	0	0	0	0	0	0	0	0	0	0	0	0	0	0	0	0	0	0	0	0	0	0	0	0	0
4	0	0	0.47	0	1	0	0	0	0	0	0	0	0	0	0	0	0.24	0	0	0	0.06	0	0	0	0	0	0	0	0	0	0
5	0	0	0	1	0	0.65	0	0	0	0	0	0	0	0	0	0	0	0	0	0	0	0	0	0	0	0	0	0	0	0	0
6	0	0	0	0	0.65	0	0.71	0.41	0	0	0	0	0	0	0	0	0	0.24	0	0	0	0	0	0	0	0	0	0	0	0	0
7	0	0	0	0	0	0.71	0	0	0	0	0	0	0	0	0	0.29	0	0	0.18	0	0	0	0	0	0	0	0	0	0	0	1
8	0	0	0	0	0	0.41	0	0	0.71	0	0	0	0	0	0	0	0	0	0	0	0	0	0	0	0	0	0	0	0	0	0
9	0	0	0	0	0	0	0	0.71	0	0.47	0	0	0	0	0	0	0	0	0	0.12	0	0	0	0	0	0	0	0	0	0	0
10	0	0	0	0	0	0	0	0	0.47	0	0	0	0	0.35	0	0	0	0	0	0	0	0	0	0	0	0	0	0	0	0	0
11	0	0	0	0	0	0	0	0	0	0	0	0.35	0	0	0	0	0	0	0	0	0	0	0	0	0	0	0	0	0	0	0
12	0	0	0	0	0	0	0	0	0	0	0.35	0	0.76	0	0	0	0	0	0	0	0	0	0	0	0	0	0	0	0	0	0
13	0	0	0	0	0	0	0	0	0	0	0	0.76	0	0.76	0	0	0	0	0	0	0	0	0	0	0	0	0	0	0	0	0
14	0	0	0	0	0	0	0	0	0	0.35	0	0	0.76	0	0.71	0	0	0	0	0	0	0	0	0	0	0	0	0	0	0	0
15	0	0	0	0	0	0	0	0	0	0	0	0	0	0.71	0	0	0	0	0	0	0	0	0	0	0	0	0	0	0	0	0
16	0	0	0	0	0	0	0.29	0	0	0	0	0	0	0	0	0	0	0	0	0	0	0	0	0	0	0	0	0	0	0	0
17	0	0.18	0	0.24	0	0	0	0	0	0	0	0	0	0	0	0	0	0	0	0	0	0	0	0	0	0	0	0	0	0	0
18	0	0	0	0	0	0.24	0	0	0	0	0	0	0	0	0	0	0	0	0	0	0	0	0	0	0	0	0	0	0	0	0
19	0	0	0	0	0	0	0.18	0	0	0	0	0	0	0	0	0	0	0	0	0	0	0	0	0	0	0	0	0	0	0	0
20	0	0	0	0	0	0	0	0	0.12	0	0	0	0	0	0	0	0	0	0	0	0	0	0	0	0	0	0	0	0	0	0
21	0	0	0	0.06	0	0	0	0	0	0	0	0	0	0	0	0	0	0	0	0	0	0	0	0	0	0	0	0	0	0	0
22	1	0	0	0	0	0	0	0	0	0	0	0	0	0	0	0	0	0	0	0	0	0	0	0	0	0	0	0	0	0	0
23	1	0	0	0	0	0	0	0	0	0	0	0	0	0	0	0	0	0	0	0	0	0	0	0	0	0	0	0	0	0	0
24	0	0	0	0	0	0	0	0	0	0	0	0	0	0	0	0	0	0	0	0	0	0	0	0	0.06	0	0	0	0	0	0
25	0	0	0	0	0	0	0	0	0	0	0	0	0	0	0	0	0	0	0	0	0	0	0	0.06	0	0.12	0	0	0	0	0
26	0	0	0	0	0	0	0	0	0	0	0	0	0	0	0	0	0	0	0	0	0	0	0	0	0.12	0	0.12	0	0	0	0
27	0	0	0	0	0	0	0	0	0	0	0	0	0	0	0	0	0	0	0	0	0	0	0	0	0	0.12	0	0	0	0	1
28	0	0	0	0	0	0	0	0	0	0	0	0	0	0	0	0	0	0	0	0	0	0	0	0	0	0	0	0	0	0	1
29	0	0	0	0	0	0	0	0	0	0	0	0	0	0	0	0	0	0	0	0	0	0	0	0	0	0	0	0	0	0	1
30	0	0	0	0	0	0	0	0	0	0	0	0	0	0	0	0	0	0	0	0	0	0	0	0	0	0	0	0	0	0	1
31	0	0	0	0	0	0	1	0	0	0	0	0	0	0	0	0	0	0	0	0	0	0	0	0	0	0	1	1	1	1	0

Fig. 13. Conductance values for August (HOTRAX 3rd photograph). The first column on the left and the first row on top represent ponds that are connected to the battery node on the left. The last column on the right and the last row represent the battery node on the right. Each nonzero value on the graph represents the conductance between two melt ponds.

Acknowledgments

We gratefully acknowledge support from the Arctic and Global Prediction Program at the Office of Naval Research (ONR) through Grant N00014-13-10291. We are also grateful for the support from the Division of Mathematical Sciences and the Division of Polar Programs at the U.S. National Science Foundation (NSF) through Grants ARC-0934721, DMS-0940249, and DMS-1413454. We would like to thank the NSF Math Climate Research Network (MCRN) as well for their support of this work, and Don Perovich for providing the melt pond images.

Appendix A

Here we explain in more detail some of the concepts and techniques of image processing and analysis used in the body of the paper.

(i) *Thresholding:* Consider an image in which the value of each pixel is denoted by $f(x, y)$ where x and y are the 2-dimensional coordinates of the pixel. If the image is bimodal, i.e., most pixel values fall in two major groups, then this image can be converted to a binary image by performing the following threshold operation:

$$g(x,y)=\left(\begin{array}{ll}0 & \text{if} \quad f(x,y)>T,\\ 1 & \text{if} \quad f(x,y)\leq T.\end{array}\right.$$

In the resulting image $g(x, y)$, all unity-valued pixels are considered to be the foreground and the zero-valued pixels are the background.

(ii) *Mathematical morphology:* This uses set theory and is commonly applied in image processing solutions as it applies well to the analysis of geometric shapes and structures. For example, in a binary image, the set of all zero-valued pixels can be considered to represent the background, and the unity-valued pixels, the foreground. When applied in image processing, mathematical morphology usually employs structuring elements or masks which are used to perform various operations on the images of interest. Some examples of structuring elements are shown in Fig. 14.

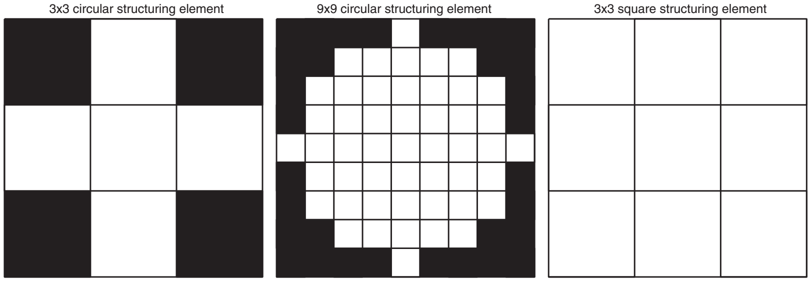

Fig. 14. Structuring elements of different sizes.

(–
ii-
i-

Table 1
List of images considered.

Set	Month	Number of images	Database
1	June	5	SHEBA
2	July	10	SHEBA
3	August	10	HOTRAX

Table 2
Average time to process each image.

Set	Month	Database	Number of iterations	Average time (minutes)
1	June	SHEBA	8	31.66
2	July	SHEBA	20	9.06
3	August	HOTRAX	20	18.04

) *Translation:* A 2-D image can be represented by a 2-D integer space Z^2. Each pixel in the image has a value and is associated with a fixed location $z = (x, y)$. Translation of a set B, by $z = (z_1, z_2)$ is given by,

$$(B)_z = \{c | c = b + z, \forall\ b \in B\}.$$

Translation shifts every point in B, (x, y), to $(x + z_1, y + z_2)$ to result in $(B)_z$.

(iv) *Reflection:* Reflection of a set B is given by

$$\hat{B} = \{c | c = -b, \forall\ b \in B\}.$$

Reflection is the mirror image of B such that every point in B, (x, y), is reflected to $(-x, -y)$, resulting in $\hat{B}$. If B is symmetric then $B = \hat{B}$.

(v) *Erosion:* The erosion of A by B is defined as

$$A \ominus B = \{z | (B)_z \subset A\} \text{where } A, B \in Z^2.$$

Erosion of A by B results in a set of points z so that all the elements of B translated by z fit completely inside A. Erosion usually results in the removal of the outermost layers of the foreground.

(vi) *Dilation:* The dilation of A by B is defined as

$$A \oplus B = \left\{z | \left(\hat{B}\right)_z \cap A \subset A\right\} \text{ where } A, B \in Z^2.$$

Dilation of A by B results in a set of points z so that at least one element of B translated by z overlaps with A. Dilation results in the addition of layers to the foreground in an image.

(vii) *Geodesic opening:* Opening of A by B is erosion of A by B followed by dilation of the result by B,

$$A \circ B = (A \ominus B) \oplus B. \tag{7}$$

This results in smoothing of the image by the removal of small protrusions and breakage of narrow connections.

Table 3
List of parameters used for different image sets.

Set	Constriction ratio	Number of erosion steps
1	20	8
2	20	18
3	20	20

Table 4
Conductivities for image set 1.

Image1	Image2	Image3	Image4	Image5
0	0	0	0	0

Table 5
Conductivities for image set 2.

Image1	Image2	Image3	Image4	Image5
0	0	0	0	0
Image6	**Image7**	**Image8**	**Image9**	**Image10**
0	0.0546	0.0283	0.0443	0.2062

Table 6
Conductivities for image set 3.

Image1	Image2	Image3	Image4	Image5
0	0.0542	0.1353	0.1216	0.0563
Image6	**Image7**	**Image8**	**Image9**	**Image10**
0.1778	0.1003	0.1078	0.0718	0.1127

(viii) *Geodesic closing:* Closing of A by B is dilation of A by B followed by erosion of the result by B.

$$A \bullet B = (A \oplus B) \ominus B. \tag{8}$$

This results in smoothing of the image by filling in of small gaps and fusing of narrowly separated components.

(ix) *Geodesic distance:* The geodesic distance between two points in a binary image is the distance length of the path between the two points in pixels, such that the entire path lies in the same set as the two points. For example, in the foreground (unity-valued pixels), the distance between two pixels is measured along paths in which all pixels are unity.

(x) *Connected components:* This is a technique for finding all the elements in a binary image that are connected to each other. Let A be the image in which we are trying to find connected components and B be a 3 × 3 structuring element. X_0 is an image with the same size as A, but containing one unity-valued pixel at the same location as the component of interest in A. This is called the seed. To find all the pixels in A connected to the seed, the following operation is performed recursively until $X_k = X_{k-1}$,

$$X_k = (X_{k-1} \oplus B) \cap A \ \ with\ \ k = 1, 2, \ldots \tag{9}$$

References

Addison, J., 1969. Electrical properties of saline ice. J. Appl. Phys. 40, 3105–3114.

Boé, J., Hall, A., Qu, X., 2009. September sea-ice cover in the Arctic Ocean projected to vanish by 2100. Nat. Geosci. 2, 341–343. http://dx.doi.org/10.1038/NGEO467.

Broadbent, S.R., Hammersley, J.M., 1957. Percolation processes I. Crystals and mazes. Proc. Camb. Philos. Soc. 53, 629–641.

Buckley, R.G., Staines, M.P., Robinson, W.H., 1986. In situ measurements of the resistivity of Antarctic sea ice. Cold Reg. Sci. Technol. 12 (3), 285–290.

Christensen, K., Moloney, N.R., 2005. Complexity and Criticality. Imperial College Press, London.

Curry, J.A., Schramm, J.L., Ebert, E.E., 1995. On the sea ice albedo climate feedback mechanism. J. Clim. 8, 240–247.

Flocco, D., Feltham, D.L., 2007. A continuum model of melt pond evolution on Arctic sea ice. J. Geophys. Res. 112, C08016. http://dx.doi.org/10.1029/2006JC003836.

Flocco, D., Feltham, D.L., Turner, A.K., 2010. Incorporation of a physically based melt pond scheme into the sea ice component of a climate model. J. Geophys. Res. 115, C08012. http://dx.doi.org/10.1029/2009JC005568 (14 pp.).

Flocco, D., Schroeder, D., Feltham, D.L., Hunke, E.C., 2012. Impact of melt ponds on arctic sea ice simulations from 1990 to 2007. J. Geophys. Res. 117 (C9), C09032. http://dx.doi.org/10.1029/2012JC008195 (17 pp.).

Fujino, K., Suzuki, Y., 1963. An attempt to estimate the thickness of sea ice by electrical resistivity method II. Low Temp. Sci. A21, 151–157.

Golden, K., 1991. Bulk conductivity of the square lattice for complex volume fraction. Int. Ser. Numer. Math. 102.

Golden, K.M., Ackley, S.F., Lytle, V.I., 1998. The percolation phase transition in sea ice. Science 282, 2238–2241.

Golden, K.M., Eicken, H., Heaton, A.L., Miner, J., Pringle, D., Zhu, J., 2007. Thermal evolution of permeability and microstructure in sea ice. Geophys. Res. Lett. 34, L16501. http://dx.doi.org/10.1029/2007GL030447 (6 pages and issue cover).

Goldenfeld, N., 1992. Lectures on Phase Transitions and the Renormalization Group. Westview Press, Boulder.

Gonzalez, R.C., Woods, R.E., 2008. Digital Image Processing. Third edition. Prentice Hall, Upper Saddle River, NJ.

Hohenegger, C., Alali, B., Steffen, K.R., Perovich, D.K., Golden, K.M., 2012. Transition in the fractal geometry of Arctic melt ponds. Cryosphere 6, 1157–1162.

Hunke, E.C., Lipscomb, W.H., 2010. CICE: the Los Alamos Sea Ice Model Documentation and Software User's Manual Version 4.1 LA-CC-06-012. T-3 Fluid Dynamics Group. Los Alamos National Laboratory.

Hunke, E.C., Hebert, D.A., Lecomte, Olivier, 2013. Level-ice melt ponds in the Los Alamos sea ice model, CICE. In: Perrie, W., Gerdes, R., Hunke, E., Treguier, A.-M. (Eds.), Ocean Modelling. 71, pp. 26–42 (Special Issue on the Arctic).

Ingham, M., Pringle, D.J., Eicken, H., 2008. Cross-borehole resistivity tomography of sea ice. Cold Reg. Sci. Technol. 52, 263–277. http://dx.doi.org/10.1016/jcoldregions.2007.05.002.

Mason, S.J., Zimmermann, H.J., 1960. Electronic Circuits, Signals and Systems. John Wiley and Sons, New York.

Milton, G.W., 2002. Theory of Composites. Cambridge University Press, Cambridge.

Pedersen, C.A., Roeckner, E., Lüthje, M., Winther, J., 2009. A new sea ice albedo scheme including melt ponds for ECHAM5 general circulation model. J. Geophys. Res. 114, D08101. http://dx.doi.org/10.1029/2008JD010440.

Perovich, D.K., Tucker III, W.B., Ligett, K.A., 2002. Aerial observations of the evolution of ice surface conditions during summer. J. Geophys. Res. 107 (C10). http://dx.doi.org/10.1029/2000JC000449.

Perovich, D.K., Richter-Menge, J.A., Jones, K.F., Light, B., 2008. Sunlight, water, and ice: extreme Arctic sea ice melt during the summer of 2007. Geophys. Res. Lett. 35, L11501. http://dx.doi.org/10.1029/2008GL034007.

Perovich, D.K., Grenfell, T.C., Light, B., Elder, B.C., Harbeck, J., Polashenski, C., Tucker III, W.B., Stelmach, C., 2009. Transpolar observations of the morphological properties of Arctic sea ice. J. Geophys. Res. 114, C00A04. http://dx.doi.org/10.1029/2008JC004892.

Pistone, K., Eisenman, I., Ramanathan, V., 2014. Observational determination of albedo decrease caused by vanishing arctic sea ice. Proc. Natl. Acad. Sci. 111 (9), 3322–3326.

Polashenski, C., Perovich, D., Courville, Z., 2012. The mechanisms of sea ice melt pond formation and evolution. J. Geophys. Res. C Oceans 117, C01001. http://dx.doi.org/10.1029/2011JC007231 (23 pp.).

Pringle, D.J., Miner, J.E., Eicken, H., Golden, K.M., 2009. Pore-space percolation in sea ice single crystals. J. Geophys. Res: Oceans 114, C12017. http://dx.doi.org/10.1029/2008JC005145 (12 pp.).

Reid, J.E., Pfaffling, A., Worby, A.P., Bishop, J.R., 2006. In situ measurements of the direct-current conductivity of Antarctic sea ice: implications for airborne electromagnetic sounding of sea-ice thickness. Ann. Glaciol. 44, 217–223.

Scharien, R.K., Yackel, J.J., 2005. Analysis of surface roughness and morphology of first-year sea ice melt ponds: implications for microwave scattering. IEEE Trans. Geosci. Rem. Sens. 43, 2927.

Scott, F., Feltham, D.L., 2010. A model of the three-dimensional evolution of Arctic melt ponds on first-year and multiyear sea ice. J. Geophys. Res. 115, C12064. http://dx.doi.org/10.1029/2010JC006156.

Serreze, M.C., Holland, M.M., Stroeve, J., 2007. Perspectives on the Arctic's shrinking sea-ice cover. Science 315, 1533–1536.

Skyllingstad, E.D., Paulson, C.A., Perovich, D.K., 2009. Simulation of melt pond evolution on level ice. J. Geophys. Res. 114, C12019. http://dx.doi.org/10.1029/2009JC005363.

Stauffer, D., Aharony, A., 1992. Introduction to Percolation Theory. Second edition. Taylor and Francis Ltd., London.

Stroeve, J., Holland, M.M., Meier, W., Scambos, T., Serreze, M., 2007. Arctic sea ice decline: faster than forecast. Geophys. Res. Lett. 34 (9), L09591. http://dx.doi.org/10.1029/2007GL029703.

Thyssen, F., Kohnen, H., Cowan, M.V., Timco, G.W., 1974. DC resistivity measurements on the sea ice near pond inlet. Polarforschung 44, 117–126.

Torquato, S., 2002. Random Heterogeneous Materials: Microstructure and Macroscopic Properties. Springer-Verlag, New York.

Van Steen, M., 2010. Graph Theory and Complex Networks, An Introduction. Maarten Van Steen.

Zhu, J., Jabini, A., Golden, K.M., Eicken, H., Morris, M., 2006. A network model for fluid transport in sea ice. Ann. Glaciol. 44, 129–133.

CHAPTER 8

WAVE-ICE INTERACTION IN THE MARGINAL ICE ZONE

In this chapter we employ the tools of Homogenization Theory to develop the first bounds for the effective viscoelasticity of ice-water mix in the marginal ice zones of the Arctic and Antarctic. Wave-ice interaction is an important but difficult process to model and often numerically expensive. As a result continuum models have been developed which treat the ice-water mix as a single viscoelastic material atop an inviscid ocean. All of the models depend on knowledge of the effective rheological properties of the top layer and to date have only been guessed at or estimated. However, we have developed a Stieltjes integral representation for the complex viscoelasticity involving the spectral measure of a self adjoint operator in the quasi-static limit. This produces rigorous bounds for the effective parameter which take into account the geometry of the ice floes. We further relate the effective parameter to a wave equation, valid in the quasi-static limit, which produces a simplified dispersion relation where the wave number and attenuation rate of plane-like waves propagating through the marginal ice zone are defined by the effective parameter itself. We are also able to use this relation in the reverse direction to extract data from *in situ* measurements of wave propagation made during SIPEX II in 2012. The data sit comfortably within the bounds. We also explore the use of this wave equation in capturing some of the average properties of the marginal ice zone such as the effect waves have on the floe size distribution and the extent of the marginal ice zone. Chapter 8 will be written up for publication and will include authors: **Christian Sampson, Elena Cherkaev, Ben Murphy, and Kenneth M. Golden.**

8.1 Abstract

The marginal ice zone (MIZ) is the region of sea ice cover that is close enough to the open ocean to be affected by its dynamics. Over the past several years there has been an

increasing realization of the importance of wave-ice interactions in the growth and decay of the seasonal ice pack. In fact, a striking correlation between Antarctic sea ice extent and wave activity has been found recently. In both the Arctic and Antarctic, the ice floe size distribution in the MIZ plays a central role in the properties of wave propagation through it. Ocean waves break up and shape the ice floes which, in turn, attenuate various wave characteristics, controlling which wave magnitudes and wavelengths propagate further into the pack. This ice-ocean interaction has become increasingly important recently in the Arctic, due to the dramatic decrease of the summer ice extent which has increased the size of the Arctic MIZ. These interactions are complex and often numerically expensive to incorporate in large scale sea ice models. By employing the tools of homogenization theory, we seek to improve our understanding of the key processes in wave ice interactions as well as develop simple models which capture the overall behavior of wave propagation in the MIZ. Here we derive bounds for the effective parameter of a recent continuum model for wave propagation, a model already being incorporated into numerical models. We further develop a simple model of ice break up from wave action and use it to capture some average characteristics of the floe size distribution of the Antarctic MIZ.

8.2 Introduction

Wave-ice interactions in the polar oceans comprise a complex but important set of processes influencing sea ice extent, ice pack albedo, and ice thickness. Waves have always played an important role in shaping the MIZ in the Antarctic. Incoming waves from the southern ocean propagate into the ice pack, breaking and shaping the ice. In the Arctic, due to recent decrease in summer sea ice extent, wave propagation has become increasingly important to the dynamics of the ice pack. Because sea ice is an integral component of the Earth's climate system it is important to consider wave-ice interactions in any large scale sea ice model. This can be difficult due to the complexity of the processes at play as well as the numerical cost when modeling individual floes under wave action. There are also two scales at play here, on the small scale, for short wave length waves, wave scattering off of individual floes will heavily attenuate incoming waves along with some viscous effects. At the larger scale, long wave lengths, scattering plays a smaller role and longer waves typically attenuate much more slowly and propagate further into the ice pack [19, 20, 22, 32, 37]. As a result it is the long wave length waves which have the greatest effect on the MIZ and could be considered the dominating factor. It is therefore useful to develop simple models which accurately capture the the dominant behavior of waves in the MIZ which can be applied to large scale sea ice models. This is our focus here.

Many studies of MIZ wave propagation focus on solitary floe models, where the scattering of an incoming wave is simplified to that of an isolated floe or multiple floes. Recently, continuum models have been developed which treat the MIZ as a two component composite of ice and slushy water. Several of the proposed models treat the ice and slushy water mix as a single material atop an inviscid ocean. These models are particularly appropriate for longer wavelengths. The top layer has been taken to be purely elastic [1], purely viscous [17], and viscoelastic [25, 38]. At the heart of these models are effective parameters, namely, the effective elasticity, viscosity, and complex viscoelasticity. In practice, these effective parameters, which depend on the composite geometry and the physical properties of the constituents, are quite difficult to determine. To help overcome this limitation, we employ the methods of homogenization theory, in a quasi-static, fixed frequency regime, to find a Stieltjes integral representation for the complex viscoelasticity of the two layer model presented in [38]. We choose this model as it is a more general case which can be reduced to the purely viscous or purely elastic cases. The derivation is motivated by earlier work in [8]. There a Stieltjes integral representation is derived for a compressible viscoelastic material. The analytic Stieltjes integral representation has been extended to effective elastic properties in the past as well [6, 9, 24, 29]. Stieltjes integral representations for the effective viscoelastic shear modulus have been previously obtained using the torsion of a viscoelastic cylinder whose microstructure is uniform in the axial direction [4, 5, 35]. The integral representation we find involves the spectral measure of a self adjoint operator and provides bounds on the effective viscoelasticity using the analytic continuation method [3, 16, 23]. The bounds themselves depend on the moments of the measure: the more moments known, the tighter the bounds. We further develop a simple wave equation which governs wave motion in the quasi-static regime. This equation produces a simplified dispersion relation that relates the wave number and attenuation rate of plane like waves traveling through the MIZ to the effective parameter. We then use the wave equation to model wave breaking of ice in the MIZ and are able to accurately capture many average characteristics of the floe size distribution in the marginal ice zone of Antarctica.

8.3 General Governing Equations

For a linear incompressible material the momentum balance equation and incompressibility condition are given by:

$$\nabla \cdot (\sigma + PI) + F = \rho \frac{\partial^2 u}{\partial t^2} \tag{8.1}$$

$$\nabla \cdot u = 0 \tag{8.2}$$

where u is the displacement, $\sigma_{ij} = C_{ijkl}\epsilon_{kl}$ is the stress tensor, C_{ijkl} the elasticity tensor, $\epsilon = \nabla u + \nabla^T u$ the symmetric strain tensor, and F the body forces. In our case we will take F as the force of gravity.

For an incompressible-viscoelastic material $C_{ijkl} = \nu\Lambda_s$ where $\nu \in \mathbb{C}$ and $\Lambda_s = \delta_{ik}\delta_{jl} + \delta_{il}\delta_{jk} - \frac{2}{3}\delta_{ij}\delta_{kl}$ is the shear projection onto the deavitoric portion of the stress tensor [8]. The compressive stress lies with the pressure term, PI, where I is the identity matrix. Further, since $\nabla \cdot u = 0$ we have that,

$$\sigma_{ij} = C_{ijkl}\epsilon_{kl} = \nu\Lambda_{s_{ijkl}}\epsilon_{kl} = 2\nu\epsilon_{ij}. \tag{8.3}$$

We may also define the compliance tensor as the inverse of the elasticity tensor, $L_{ijkl} = C^{-1}_{ijkl}$, in which case we have the constitutive relation $\epsilon_{ij} = L_{ijkl}\sigma_{kl}$. Then from eq (8.3) we may say,

$$L_{ijkl}\sigma_{kl} = \frac{1}{2\nu}\sigma_{ij} = \epsilon_{ij}. \tag{8.4}$$

We will also assume that our material is irrotational in which case

$$\nabla \times \epsilon = 0. \tag{8.5}$$

Here $\nabla\times$ is the curl as defined for a rank two tensor, $\nabla \times \epsilon = e_{ikl}\left(\partial_k \epsilon_{lj}\right)$, where e_{ikl} is the Levi-Civita symbol.

8.4 Kelvin-Voight Model

In this section we establish the conditions of "quazi-static" for the particular case of the two layer model presented in [38]. This will enable us to derive bounds for the complex viscoelasticity in section 8.4.1. In this model the ice layer is taken to be viscoelastic and sits atop an inviscid ocean. The model itself is developed under the assumption of harmonic wave propagation and the viscoelasticity is modeled as a Kelvin-Voight type material. Our goal is to recast the equations of motion into a elastostatic form which we may then homogenize.

The Kelvin-Voight model for viscoelasticity, in conjunction with incompressibility, is consistent with the general governing equations outlined above. In this model, our material is taken to be a combination of a spring and dash pot in parallel. In this case, the deviatoric part of the stress is given by:

$$\sigma = 2G\epsilon + 2\rho v \frac{\partial \epsilon}{\partial t}. \tag{8.6}$$

Here, G is the shear modulus and v the kinematic viscosity. Under the assumption of a simple harmonic wave, $u(x,z,t) = u(z)e^{i(kx-\omega t)}$, we may say $\frac{\partial \epsilon}{\partial t} = -i\omega\epsilon$. In this case, the wave number is $k = k_r + iq$ where k_r is the wave number and q is the attenuation rate. Applying this to (8.6) we obtain:

$$\sigma = 2G\epsilon - 2i\rho v\omega\epsilon = 2\nu\epsilon, \qquad \nu = G - i\rho v\omega \tag{8.7}$$

We can then define the elasticity tensor for this case as $C_{ijkl} = \nu\Lambda_{s_{ijkl}}$ so that $\sigma_{ij} = C_{ijkl}\epsilon_{kl} = 2\nu\epsilon_{ij}$. Then since $\nabla \cdot u = 0$ we have that $\nabla \cdot \epsilon = \nabla^2 u$ and our momentum balance equation (8.1) becomes:

$$2\nu\nabla^2 u + \nabla P - \rho g e_z = \rho\frac{\partial^2 u}{\partial t^2}. \tag{8.8}$$

This is equivalent to the model presented in [38]. However ours is written in terms of displacement and strain, instead of velocity and strain rate.

To apply this model to gravity waves in a ice covered ocean, we consider a two layer model in which the ice and slush form an effective viscoelastic layer which sits atop an inviscid ocean. We illustrate this in Figure 8.1. As noted above, we consider harmonic waves, in particular, waves for which the wavelength is much larger than the thickness of the ice layer and for which the frequency ω is small. In this case the wave number k is small, and we consider waves for which $|kh| << 1$, $|k\omega| << 1$ and $\omega^2 << 1$. We also consider waves for which the amplitude is on the order of the ice thickness.

For a simple harmonic wave and the boundary conditions presented in [38], the model we employ, ∇P takes the form:

$$\nabla P = \left[\rho\omega k e^{i(kx-\omega t)}\left(A\cosh(kz) + B\sinh(kz)\right), \tag{8.9}$$

$$\rho\omega k e^{i(kx-\omega t)}\left(A\sinh(kz) + B\cosh(kz)\right) + \rho g\right]. \tag{8.10}$$

Under the long wave length, low frequency assumption in the first layer, we have $|kz| \leq |kh| << 1$ and $|\omega k| << 1$. We then see that $\nabla P \approx \rho g e_z$. Further, because of our harmonic wave assumption, we see that $\frac{\partial^2 u}{\partial t^2} = -\omega^2 u(z) e^{i(kx-\omega t)}$. Then, taking $\omega^2 \approx 0$ but keeping the terms of order ω in ν, we arrive at the quasi-static limit for fixed frequency,

$$2\nu\nabla^2 u = 0. \tag{8.11}$$

or

$$\nabla \cdot \sigma = 0 \tag{8.12}$$

Putting this back in terms of the elasticity tensor and strain tensor we have,

$$\nabla \cdot \left(C_{ijkl}\epsilon_{kl}\right) = 0, \qquad C_{ijkl} = \nu\Lambda_{s_{ijkl}}. \tag{8.13}$$

We note that when using the Kelvin-Voight model, our effective parameter depends on density and frequency and as a result the bounds we derive later will as well.

8.4.1 Integral Representation and Elementary Bounds

Consider Hooke's law for a linear elastic material,

$$\sigma_{ij}(x,\psi) = C_{ijkl}(x,\psi)\epsilon_{kl}(x,\psi)$$

where $x \in \mathbb{R}^d$, $\psi \in \Psi$ and Ψ is the set of all realizations of the random elastic medium and is pared with a probability measure P. We then define $\langle\cdot\rangle$ to be the ensemble average over Ψ. We will assume that our material is statistically isotropic. Thus, $C_{ijkl}(x,\psi), \epsilon_{ij}(x,\psi), \sigma_{ij}(x,\psi)$ are ergodic stationary random fields, which implies that the ensemble average over ψ will be equivalent the spatial average over all of $\mathbb{R}^d$ [28]. We can then define the effective elasticity tensor C^*_{ijkl} through the equation [8, 24, 28, 29],

$$\langle \sigma_{ij} \rangle = \langle C_{ijkl} \epsilon_{kl} \rangle = C^*_{ijkl} \langle \epsilon_{kl} \rangle, \tag{8.14}$$

where we have omitted (x, ψ) for notational simplicity. In this way, we have defined the effective elasticity tensor to be the constant tensor which relates the average stress to the average strain. Similarly, we can define the effective compliance tensor L^*_{ijkl} [28] as,

$$\langle \epsilon_{ij} \rangle = \langle L_{ijkl} \sigma_{kl} \rangle = L^*_{ijkl} \langle \sigma_{kl} \rangle. \tag{8.15}$$

Next, we consider the set of quazistatic, irrotational governing equations and respective constitutive relations for the stationary random fields ϵ, σ,

$$\nabla \cdot \sigma = 0 \qquad\qquad C_{ijkl} \epsilon_{kl} = 2\nu \epsilon_{ij} = \sigma_{ij} \tag{8.16}$$

$$\nabla \times \epsilon = 0 \qquad\qquad L_{ijkl} \sigma_{kl} = \frac{1}{2\nu} \sigma_{ij} = \epsilon_{ij}, \tag{8.17}$$

on a two component viscoelastic material where materials one and two have complex viscoelasticity ν_1 and ν_2, respectively. In this case we may define the local elasticity tensor by,

$$C_{ijkl} = \left(\chi_1 \nu_1 + (1 - \chi_1) \nu_2\right) \Lambda_{s_{ijkl}}. \tag{8.18}$$

Here $\chi_1(x)$ is an indicator function which takes on value 1 when in material 1 and 0 otherwise. Inserting this into (8.13) we obtain,

$$\nabla \cdot \left(\chi_1 \nu_1 + (1 - \chi_1) \nu_2\right) \Lambda_{s_{ijkl}} \epsilon_{kl} = 0. \tag{8.19}$$

Defining $s = 1/(1 - \frac{\nu_1}{\nu_2})$, using the fact that $\Lambda_{s_{ijkl}} \epsilon_{kl} = 2\epsilon_{ij}$, and dropping subscripts for notational simplicity we obtain,

$$\nabla \cdot \nu_2 \left(1 - \frac{1}{s} \chi_1\right) 2\epsilon = 0. \tag{8.20}$$

Following previous work [8], we define $\epsilon^f = \nabla^s \phi$ to represent the mean fluctuation of the average strain ϵ^0 so that $\epsilon = \epsilon^0 + \nabla^s \phi$. Applying this to (8.20) we obtain,

$$\nabla \cdot \nabla^s \phi = \nabla \cdot \left(\frac{1}{s} \chi_1 (\epsilon^0 + \nabla^s \phi)\right). \tag{8.21}$$

We then apply the operator $\nabla^s (\nabla \cdot \nabla^s)^{-1}$, add ϵ^0 to both sides, and rearrange to arrive at the equation,

$$\epsilon^0 + \nabla^s \phi - \nabla^s (\nabla \cdot \nabla^s)^{-1} \nabla \cdot \left(\frac{1}{s} \chi_1 (\epsilon^0 + \nabla^s \phi)\right) = \epsilon^0. \tag{8.22}$$

Defining $\Gamma = \nabla^s(\nabla \cdot \nabla^s)^{-1}\nabla\cdot$ and solving for ϵ we arrive at

$$\epsilon = \left(1 - \frac{1}{s}\Gamma\chi_1\right)^{-1} \epsilon^0. \tag{8.23}$$

It is worth noting that the operator gamma is analogous to that defined in [14] where $\nabla \cdot \nabla^s$ is replaced with $\nabla \cdot \nabla = \nabla^2$.

In a similar way we may find a resolvent representation for the stress tensor σ. It is given by,

$$\sigma = \left(1 - \frac{1}{s}\Upsilon\chi_2\right)^{-1} \sigma^0 \tag{8.24}$$

where $\chi_2 = 1 - \chi_1$ and $\Upsilon = \nabla \times (\nabla \times \nabla\times)^{-1} \nabla\times$. The key observation necessary to derive the expression in (8.24) is the existence of a symmetric tensor A such that our symmetric stress tensor can be defined by:

$$\sigma = \nabla \times \nabla \times A \tag{8.25}$$

The existence of A comes from the fact that $\nabla \cdot \sigma = 0$ and is a consequence of the Donati-Beltrami theorem [7]. We will further define $\Sigma = \nabla \times A$ so that $\sigma = \nabla \times \Sigma$.

We now define the inner products $(f, g) = \langle \chi_i \bar{f}, g \rangle$, $i = 1, 2$ over the Hilbert spaces defined by,

$$H^\epsilon = \left\{ f \in L^2(\Psi, P) | \Gamma f = f \ \ \textit{weakly} \right\}$$

$$H^\sigma = \left\{ f \in L^2(\Psi, P) | \Upsilon f = f \ \ \textit{weakly} \right\}.$$

Here the inner product with $i = 1$ is paired with H^ϵ and $i = 2$ with H^σ. In this case we have that $\epsilon \in H^\epsilon$ and $\sigma \in H^\sigma$ since,

$$\Gamma\epsilon = \Gamma\nabla^s u = \nabla^s(\nabla \cdot \nabla^s)^{-1}\nabla \cdot \nabla^s u = \nabla^s u = \epsilon$$

and

$$\Upsilon\sigma = \Upsilon\nabla \times \Sigma = \nabla \times (\nabla \times \nabla\times)^{-1} \nabla \times \nabla \times \Sigma = \nabla \times \Sigma = \sigma.$$

In this way, Γ and Υ is are symmetric projectors on their respective spaces. Further, χ_1 and χ_2 are symmetric projectors which implies that $\Gamma\chi_1$ and $\Upsilon\chi_2$ are self adjoint with respect to their corresponding inner product. Now we consider (ϵ^0, σ) and write $C_{ijkl}\epsilon_{kl} = C : \epsilon$ where $A : B$ is the conctraction operation. On one hand we have,

$$(\epsilon^0, \sigma) = \langle \chi_1 \epsilon^0 : (C : \epsilon) \rangle = \epsilon^0 : \langle C : \epsilon \rangle = \epsilon^0 : C^* : \epsilon^0.$$

On the other, making use of the representation of C_{ijkl} in (8.20), we find,

$$\begin{aligned} \langle \chi_1 \epsilon^0 : (C : \epsilon) \rangle &= \epsilon^0 : \langle \nu_2 \left(1 - \frac{1}{s}\right) 2\epsilon \rangle \\ &= 2\nu_2 \epsilon^0 : \langle \epsilon \rangle - 2\nu_2 \epsilon^0 \langle \frac{1}{s} \chi_1 \epsilon \rangle. \end{aligned}$$

Realizing that $\epsilon^0 : \langle \epsilon \rangle = ||\epsilon^0||^2$ and substituting in our expression for ϵ in (8.23) we find that,

$$2\nu_2 ||\epsilon^0||^2 - 2\nu_2 \epsilon^0 : \langle \chi_1 (s - \Gamma\chi_1)^{-1} \epsilon^0 \rangle.$$

Applying the spectral theorem to our resolvent representation we find,

$$\epsilon^0 : C^* : \epsilon^0 = 2\nu_2 \left(||\epsilon^0||^2 - \int_0^1 \frac{d\mu(\lambda)}{s - \lambda} \right). \tag{8.26}$$

where $\mu(\lambda) = \big(Q(\lambda)\epsilon^0, \epsilon^0\big) = \langle \chi_1 Q(\lambda) \overline{\epsilon^0} : \epsilon^0 \rangle$ and Q is a self adjoint operator with positive measure μ. We note that this integral representation is the incompressible analog to the one derived for compressible materials in [8].

For our particular problem we require $C^*_{ijkl} = \nu^* \Lambda_{s_{ijkl}}$. In this case (8.26) takes the form,

$$\frac{\nu^*}{\nu_2} = 1 - F(s), \quad F(s) = ||\epsilon^0||^{-2} \int_0^1 \frac{d\mu(\lambda)}{s - \lambda} \tag{8.27}$$

The function $F(s)$ can be expanded in terms of its moments μ^n [15, 16],

$$F(s) = \frac{\mu^0}{s} + \frac{\mu^1}{s^2} + \cdots, \tag{8.28}$$

where,

$$\mu^n = \int \lambda^n d\mu(\lambda) = \big(\chi_1 (\Gamma\chi_1)^n \epsilon^0, \epsilon^0\big) = \langle (\chi_1 \Gamma \chi_1)^n \epsilon^0 : \epsilon^0 \rangle, \tag{8.29}$$

and $\chi_1(\Gamma\chi_1)^n = (\chi_1\Gamma\chi_1)^n$ since χ_1 is a projection. Assumptions about the geometry are incorporated into μ via its moments.

Bounds on ν^* can be obtained for a fixed contrast parameter s and are determined by varying over admissible measures μ. This is the equivalent to varying over admissible geometries of the composite material. The bounds may be derived using just the moments of μ. The more moments known, the tighter the bounds [14, 26]. For the elementary bounds knowledge of only the mass of the measure μ^0 is required and is easily calculated using (8.29). For the case where ϵ^0 has unit magnitude, it is given by,

$$\mu^0 = \left(\chi_1(\Gamma\chi_1)^0\epsilon^0, \epsilon^0\right) = \langle\chi_1\epsilon^0 : \epsilon^0\rangle = \langle\chi_1\rangle||\epsilon^0||^2 = p_1 \tag{8.30}$$

where p_1 is the volume fraction of material 1 and $0 \leq p_1 \leq 1$. If we consider the set M of positive Borel measures on $[0,1]$ with mass less than unity, $F(s)$ becomes a linear functional of the measure μ for fixed complex s off the interval $[0,1]$. It is convenient to define the function

$$m(h,\mu) = \frac{\nu^*}{\nu_2} = 1 - F(s,\mu), \;\; h = \frac{\nu_1}{\nu_2}. \tag{8.31}$$

If we then examine the set,

$$M_k^\mu = \left\{\mu' \in M | \int_0^1 \lambda^n d\mu'(\lambda) = \mu^n, n = 0..k\right\} \tag{8.32}$$

we can define the set of possible values of $m(h)$ as,

$$N_\mu^k = \left\{m(h,\mu') \in \mathbb{C} | h \notin (-\infty, 0], \mu' \in M_k^\mu\right\}.$$

The set M_k^μ forms a compact, convex subset of M [16] which implies, since $F(s,\mu)$ is linear in μ, that N_μ^k is a compact subset of the complex plane. In the case that only the mass of the measure is known, $k = 0$, the extreme points of M_0^μ are the one point measures $\mu^0\delta_\lambda$ [11]. In an analogous way we can define the function

$$\hat{m}(h,\eta) = \frac{\nu_1}{\nu^*} = 1 - E(s,\eta), \qquad E(s,\eta) = ||\sigma^0||^{-2}\int_0^1 \frac{d\eta(\hat{\lambda})}{s - \hat{\lambda}} \tag{8.33}$$

and the analogous sets $M_0^\eta \subset M$ and $N_\eta^0 \subset \mathbb{C}$ for which the extreme points are also one point measures $\eta^0\delta_\lambda$.

To find the elementary bounds we take $k = 0$ and fix the volume fractions p_1 and $p_2 = 1 - p_1$. In this case we have that,

$$F(s,\mu^0) = \frac{\mu^0}{s - \lambda} \qquad E(s,\eta^0) = \frac{\eta^0}{s - \hat{\lambda}} \tag{8.34}$$

Then we may say that the values of $F(s,\mu)$ and $E(s,\eta)$ must lie with in the circles [16, 26]

$$C_0(\lambda) = \frac{p_1}{s - \lambda} \qquad \hat{C}_0(\hat{\lambda}) = \frac{p_2}{s - \hat{\lambda}} \qquad -\infty < \lambda, \hat{\lambda} < \infty \tag{8.35}$$

since $\mu^0 = p_1$ and $\eta^0 = p_2$. Using equations (8.31) and (8.33) we can map to the common ν^* plane and see that ν^* must lie with in the circular arcs [14],

$$Q_0 = \nu_2 \left(1 - \frac{p_1}{s-\lambda}\right), \qquad 0 \le \lambda \le p_2 \qquad \hat{Q}_0 = \frac{\nu_1}{1 - \frac{p_2}{s-\lambda}}, \qquad 0 \le \lambda \le p_1 \tag{8.36}$$

We note that these are analogous to the elementary bounds in the electric case [14]. In order to plot the bounds, knowledge of the component parameters $\nu_1 = G_1 - i\rho\omega v_1$ and $\nu_2 = G_2 - i\rho\omega v_2$ is needed. For the density we take the average of the densities between ice and water, $\rho \approx 974 kg/m^3$. Measurements of the shear modulus of first year ice have been made and suggest it is on the order of $G \approx 10^9 Pa$ [34]. Measurements of the viscosity of slush and grease ice suggest $v \approx 10^{-2} m^2/s$ [27, 37]. However, in the viscosity experiments elasticity is ignored. More recent wave tank experiments [40] show that a mix of mostly frazil ice, with some pancake ice, may have an effective viscoelastic parameter $\nu = G - i\rho\omega v$ with $G = 21 Pa$ and $v = 0.014 m^2/s$ suggesting that there is some component of elasticity to be considered. One would be tempted to take the ice phase as purely elastic $\nu = G + 0i$. However, this would mean the ice is not lossy. In fact, ice attenuates waves much more strongly than the slush. This is due to scattering, and friction effects at the interface of the ice and water [20]. For our analysis we will take the slush to have parameters $G = 10 Pa$ ad $v = 0.01 m^2/s$ and we will consider the ice phase to have $G = 10^9 Pa$, $v = 15 m^2/s$. This choice of v for the ice phase was estimated using (8.39). It was chosen so that the attenuation rate for “pure ice” would be on the same order as those measured for high concentrations of ice in [20]. We will also consider $G = 10^7 Pa$ for the ice as the value of 10^9 is technically associated with solid, thick first year ice. In the MIZ, the ice tends to be thinner and well soaked with a lower freeboard making it more pliable. This is especially true near the edge and very characteristic of pancake ice. The value of $G = 10^7 Pa$ produces tighter bounds which our data comfortably sit within. The bounds are shown in Figures 8.2, 8.3, and 8.4 where we plot the complex conjugate of ν^* to better highlight the contrast in parameters. In reality the bounds are reflected over the real axis. The data shown in the figures have been extracted from [13, 22] are discussed in 8.5.1.

8.5 Wave Equation

Since Λ_s is a projector on our space of strain fields and we assume the material to be incompressible we may derive a simplified wave equation in the long wave length low frequency limit. If we reintroduce the second time derivative of u and use the average stress tensor we have:

$$\nabla \cdot \langle C_{ijkl}\epsilon_{kl}\rangle = \nabla \cdot \nu^* \Lambda_{s_{ijkl}}\epsilon_{kl} = \rho \frac{\partial^2 u}{\partial t^2}. \tag{8.37}$$

Since $\nabla \cdot u = 0$ and $\Lambda_{s_{ijkl}}\epsilon_{kl} = 2\epsilon_{ij}$, we can say that $\nabla \cdot \nu^* \Lambda_{s_{ijkl}}\epsilon_{kl} = 2\nu^* \nabla^2 u$, in this case equation (8.37) becomes:

$$\nabla^2 u = \frac{\rho}{2\nu^*}\frac{\partial^2 u}{\partial t^2} \tag{8.38}$$

Under the plane wave assumption we would expect a 1-d Solution of the form $u(x,t) = A_0 e^{i(kx-\omega t)}$, where A_0 is the amplitude of the wave as it enters the MIZ. In this case, substitution of the 1-d solution into the wave equation produces a simplified dispersion relation given by:

$$(k_r + iq)^2 = \frac{\rho\omega^2}{2\nu^*}. \tag{8.39}$$

In this way, the wave number k_r, and the attenuation rate q, can be defined by the effective parameter. Or, given measurement of the wave number and attenuation rates one can infer the effective parameter.

8.5.1 Comparison to Measurement

While data on the viscoelastic parameter are difficult to obtain there have been measurements on the attenuation rate and wave number of long wavelength, low frequency waves. Most notably it was found in [22] that the energy attenuation rate of waves in the MIZ with ice fractions between 20%-60% follow the relationship,

$$\alpha = \frac{a}{T^2} + \frac{b}{T^4} \qquad\qquad a = 2.12 \times 10^{-3}, b = 4.59 \times 10^{-2}. \tag{8.40}$$

These data used in [22] were obtained using wave buoys deployed in the MIZ on the Sea Ice Physics and Ecosystem Experiment II (SIPEX II) expedition to Antarctica. Based on measurements obtained in 1998 in a similar manner, it was found in [13] that for long wave lengths, the relationship between frequency ω and wave number k_r follows a power law close to that of deep water given by,

$$k_r = c\omega^{2.41}, \qquad\qquad c = \frac{1}{g}\left(\frac{2\pi}{10}\right)^{-0.41}. \tag{8.41}$$

Taking $T = 2\pi/\omega$ and using the fact that the amplitude decay rate is half of the energy decay rate, we may substitute equations (8.40),(8.41) into (8.39) and solve for ν^* which yields,

$$\nu^* = \frac{\rho\omega^2}{2}\left(c\omega^{2.41} + i\frac{1}{2}\left(\frac{a\omega^2}{4\pi^2} + \frac{b\omega^4}{16\pi^4}\right)\right)^{-2}. \tag{8.42}$$

Here we have taken $\omega = 2\pi/T$. The data are shown in Figures 8.2, 8.3, and 8.4. We only consider frequencies from $\frac{1}{4} \leq \omega \leq 1$ corresponding to a range of periods $6s \leq T \leq 25s$. It can be seen to sit well within our bounds for sufficiently low frequencies.

8.5.2 1-d Model for Floe Breaking

Another potential use for the 1-d wave equation model is as a simple model for wave propagation in the MIZ, in particular, to understand the role that waves play in determining the floe size distribution and extent of the MIZ. In the long wave length, low frequency regime many of the waves which propagate into the ice pack act like plane waves, and thus can be modeled by the solution to the 1-d wave equation above. We will model the ice pack as a 1-d viscoelastic plate that bends to match an incoming wave profile. We will further suppose that there is a critical wave amplitude at which the ice will fracture into pieces of the size of half the wavelength of the breaking wave. This is illustrated in Figure 8.5. To determine the critical amplitude needed to break an ice floe, we follow [10] and consider breaking due to strain and stress failures. If the ice is thought to be flexural and nonrigid, breaks may form due to strain failures while more rigid ice will fail under gravitational and buoyant forces overcoming the flexural strength of the material.

The flexural strain may be defined as:

$$\epsilon = \frac{h}{2}\frac{\partial^2\eta}{\partial x^2}, \tag{8.43}$$

where η is the sea surface elevation and h the ice thickness. For a simple harmonic wave the maximum strain would be given by

$$\epsilon = \frac{hAk^2}{2}$$

where A is the amplitude, k the wave number and ω the frequency. Supposing a critical yield strain ϵ_c, we see that the crtical amplitude for strain failure is given by,

$$A_c^{\epsilon} = \frac{2\epsilon_c}{hk^2} = \frac{\epsilon_c\lambda^2}{2\pi^2 h}. \tag{8.44}$$

To model stress failure we may think of the ice as a beam of thickness h and width b placed on two supports separated by a distance L. A force F is then applied to the center between the supports. This is often referred to as the three point flexural test. The flexural stress σ may then be determined as [31]

$$\sigma = \frac{3FL}{2bh^2}. \tag{8.45}$$

In the ice case $L = \lambda/2$, and to calculate F/b we consider the average upward and downward pressure over one wavelength. At a wave crest we consider a net upward pressure (P_u) as a buoyant force proportional to the density of the water ρ_w. At a wave trough, we consider a downward pressure (P_d) resulting from an extra weight proportional to the density of the ice ρ_{ice}. We further take $P_d = P_u$ to maintain equilibrium and consider a simple sinusoidal wave profile, $A\sin(kx)$, which fits with our plane wave assumption from before. In this case F/b may be taken to be,

$$\frac{F}{b} = \frac{1}{2}\left(\rho_w g\left|\int_0^{\lambda/2} A\sin(kx)dx\right| + \rho_{ice} g\left|\int_{\lambda/2}^{\lambda} A\sin(kx)dx\right|\right) = \frac{(\rho_w + \rho_{ice})gA}{k}, \tag{8.46}$$

where $\bar{\rho} = (\rho_w + \rho_{ice})/2$. Taking $k = 2\pi/\lambda$ and making the appropriate substitutions into (8.45) we obtain,

$$\sigma = \frac{3g\bar{\rho}A\lambda^2}{2\pi h^2}. \tag{8.47}$$

If we define the critical breaking stress as σ_c, we can then find the breaking amplitude A_c^σ to be,

$$A_c^\sigma = \frac{2\pi h^2 \sigma_c}{3g\bar{\rho}\lambda^2}. \tag{8.48}$$

Using these amplitudes we can then determine how far into the ice pack a wave of a given wave length may break ice. Since we assume it will break the ice into pieces of size $\lambda/2$, this will also tell us the maximum flow size at a given position in the MIZ. For a plane wave traveling into the MIZ, the amplitude as a function of distance from the ice edge is given by $A(x) = A_0 e^{-\alpha x}$, where A_0 is the amplitude as it enters the ice field and α the attenuation rate. Thus, a wave will break the ice as long as,

$$A_0 e^{-\alpha x} \geq A_c^\epsilon \qquad \text{or} \qquad A_0 e^{-\alpha x} \geq A_c^\sigma.$$

Applying these criteria to equations (8.44) and (8.48), solving the inequalities for x, and taking the maximum, we can find the range of distances for which a given wave can break ice with maximum breaking distance occurring at equality.

$$x_b \leq max\left\{\frac{1}{\alpha}\ln\left(\frac{2\pi^2 hA_0}{\epsilon_c\lambda^2}\right), \frac{1}{\alpha}\ln\left(\frac{3g\bar{\rho}\lambda^2 A_0}{2\pi h^2\sigma_c}\right)\right\} \tag{8.49}$$

To parameterize the critical strain and stress, we take the values used in [10], $\epsilon_c = 3\times10^{-5}$ and $\sigma_c = 0.67MPa$. These values are based on work in [21, 33] and consider not only the critical threshold but the effect of fatigue as well.

To determine the initial amplitude for each wave, we make use of the Pierson-Moskowitz wave energy spectrum [30] which describes the wave energy distribution for a fully developed sea as a function of period T. The distribution is parameterized by the peak period T_p and is given by,

$$S_p(T) = 8.1\times10^{-3}g^2\left(\frac{T}{2\pi}\right)^5 \exp\left(-1.25\left(\frac{T}{T_P}\right)^4\right). \tag{8.50}$$

The corresponding amplitude distribution is then calculated from S_p with,

$$A(T) = \sqrt{4\pi S_P(T)/T}. \tag{8.51}$$

To determine the attenuation rates and write λ as a function of period we substitute (8.40) and (8.41) into (8.49). In this way, we have the maximum breaking distance of a plane like wave given by,

$$BD(T) = max\left\{\frac{1}{\alpha}\ln\left(\frac{2\pi^2 hA_0T^{4.82}}{\epsilon_c c^2(2\pi)^{4.82}}\right), \frac{1}{\alpha}\ln\left(\frac{3g\bar{\rho}c^2(2\pi)^{4.82}A_0}{2\pi h^2 T^{4.81}\sigma_c}\right)\right\} \tag{8.52}$$

$$\alpha = \frac{a}{T^2} + \frac{b}{T^4}, a = 2.12\times10^{-3}, b = 4.59\times10^{-2}, c = \frac{1}{g}\left(\frac{2\pi}{10}\right)^{-0.41}. \tag{8.53}$$

Since we are in the long wavelength regime with this approximation, we will only consider waves with period $T > 6s$. Further, waves with periods $T > 16s$ have such large wave lengths, $\lambda > 484m$, and they produce floe sizes $> 240m$ which we would not consider small enough to be included in the MIZ.

For ice thickness, we first consider the annual mean in the MIZ of $h \approx .85$ [39] and study the effect of different peak periods at the ice edge. The distance that waves, with sufficient energy to break ice, can travel into the ice pack depends sensitively on the peak period of the incident sea at the ice edge. For waves induced by storm like conditions,

$T_p > 10$, waves can travel over a thousand kilometers into the ice pack. This is exemplified in Figure. 8.6. There we show the floe sizes resulting from wave break up ($D = \lambda/2$) as a function of distance from the ice edge for waves with periods $6 \leq T \leq 16$. The maximum floe size at a given distance will be the minimum of floe sizes produced by wave breaking. That is,

$$D_{max}(x) = \frac{1}{2} \min_{\lambda} \{\lambda | BD(\lambda) = x\}. \tag{8.54}$$

It can also be noted that for storm like conditions the decay of waves with sufficient amplitude to break ice appears linear. This type of behavior was observed during the SIPEX II expedition after a storm event in the MIZ in 2012 [19].

In order to capture the average state of the MIZ we consider a Gaussian distribution of peak periods with a mean of $T_p = 7$ and a standard deviation of $S_d = 1$. We can then calculate a weighted average of the maximum breaking distance. Here we will consider peak periods from $T_p = 4s - 10s$. The reason this is important to consider can be thought of in the following way. While a storm event, characterized by high peak period, may break ice significantly far into the ice pack, eventually that ice will rejoin through freezing processes and won't be broken by waves until the next storm. In this way, only studying one peak period ignores refreezing. In a similar way, smaller waves will propagate further into the pack near the ice edge when the peak period is small, an effect also ignored if we only study one peak period. As a result we define the average breaking distance as,

$$\overline{BD}(T) = \frac{1}{6} \int_4^{10} BD(T, T_p) e^{\frac{(T_p - 7)^2}{2}} dT_P. \tag{8.55}$$

When comparing this average to measurements taken in the Antarctic MIZ in [36], we find good agreement with $h = 0.85m$. If we do vary the thickness, increasing thickness with distance, we can find better agreement in the relevant regimes as well. That is to say, choosing a specific ice thickness matching that at a given distance from the ice edge produces the correct maximum floe sizes. This is shown in Figure 8.7. This also allows us to determine the extent of the MIZ. We can define the extent of the marginal ice zone as the maximum distance waves with periods $T \leq 16S$, corresponding to a floe of $\approx 250m$, have sufficient energy to break ice.

One use of this simple model is the study of the effect waves have on the MIZ under differing climatic conditions. It has been proposed that a warming climate will lead to changes in storm frequency and intensities [18]. Simulations in the past have suggested that while tropical cyclones may decrease in frequency, there may be a doubling of the frequency of category 4 and 5 storms by the end of the 21st century [2]. Other studies observe statistical increases in storm duration and intensity over the last 40 years which correlate well with increasing sea surface temperatures [12]. As a result one would expect higher average peak periods in the marginal ice zone. Thus, waves would, on average, propagate further into the MIZ. This can have an effect on the overall volume of ice in the ice pack as broken ice is subject to lateral melting [36]. A changing MIZ could also dramatically affect wildlife in the region. In Figure 8.8 we show the maximum flow size for average peak periods of $T_p = 7, 8, 9$ and an average thickness of $h = 0.85m$. Notably, even a small change in the average peak period can produce a drastically different MIZ extent.

8.6 Conclusion

Motivated by previous works [8, 14, 29] we have developed rigorous bounds for the complex viscoelasticity of an incompressible material in equilibrium. We have further applied these bounds to the specific case of continuum models of wave dynamics in the MIZ in the long wave length, low frequency regime. When in this this regime, the governing equations can be reduced to a simplified wave equation which produces a simplified dispersion relation for plane like waves entering the marginal ice zone. Using this relation and *in situ* data collected in the MIZ of Antarctica, we have extracted an estimate of the effective complex viscoelasticity for waves of periods $6s < T < 25s$ which fit squarely with in the bounds. Using these estimates, our simplified wave equation, and ice floe fracture models, we have also produced a simple model of wave effects on the extent of of the MIZ as well as the distribution of maximum floe size as a function of distance from the ice edge.

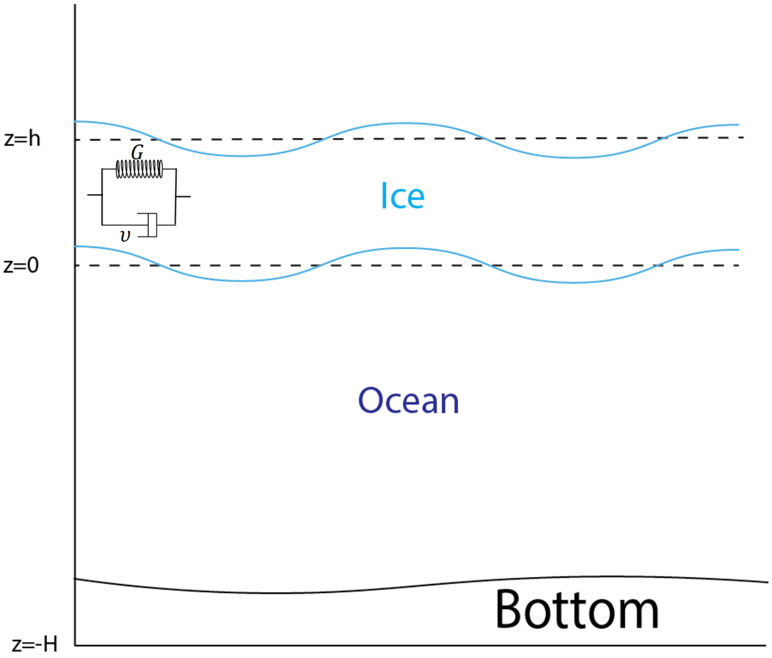

Figure 8.1: A viscoelastic layer atop an inviscid ocean of thickness h being deformed by harmonic wave profile.

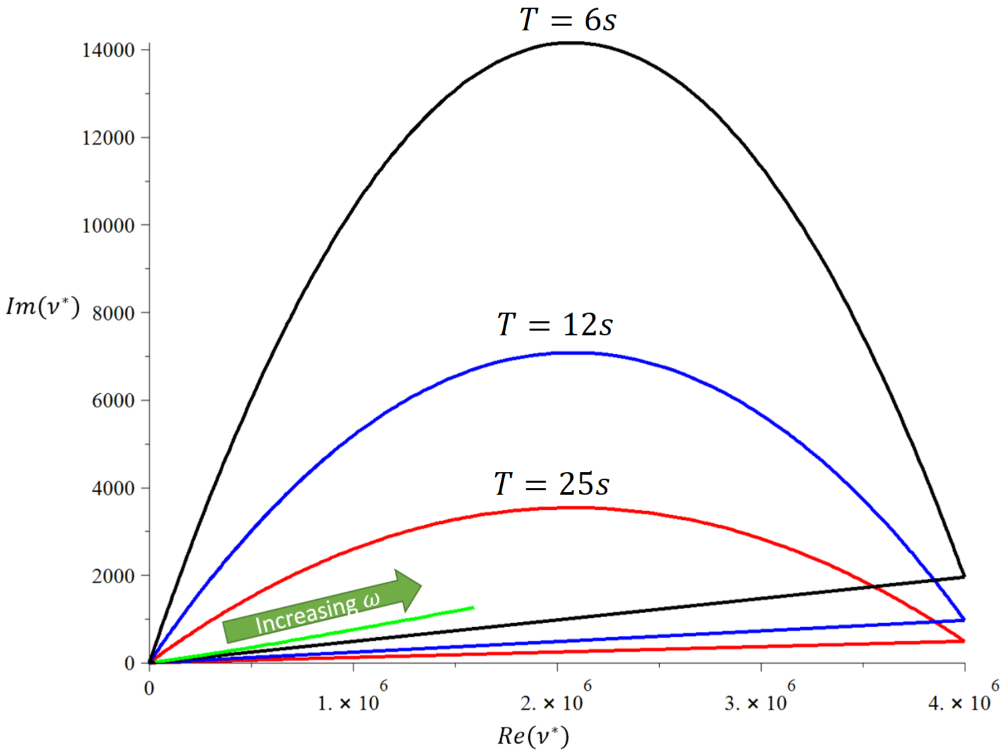

Figure 8.2: Bounds for $\bar{\nu^*}$ plotted for several periods, $T = 2\pi/\omega$, with $G = 10^7 Pa$ for the ice phase. We have plotted the complex conjugate of ν^* to better highlight the contrast in the parameters. In green are data extracted from the 1-d model and the work in [13, 22] for periods $6s \leq T \leq 25s$. Note that near $T = 6s$ the data just begin to violate the bounds. This suggests a lower limit for which the long wave length assumption is valid. Here the volume fraction of ice is $p = 0.4$, in the range for which we consider the data valid.

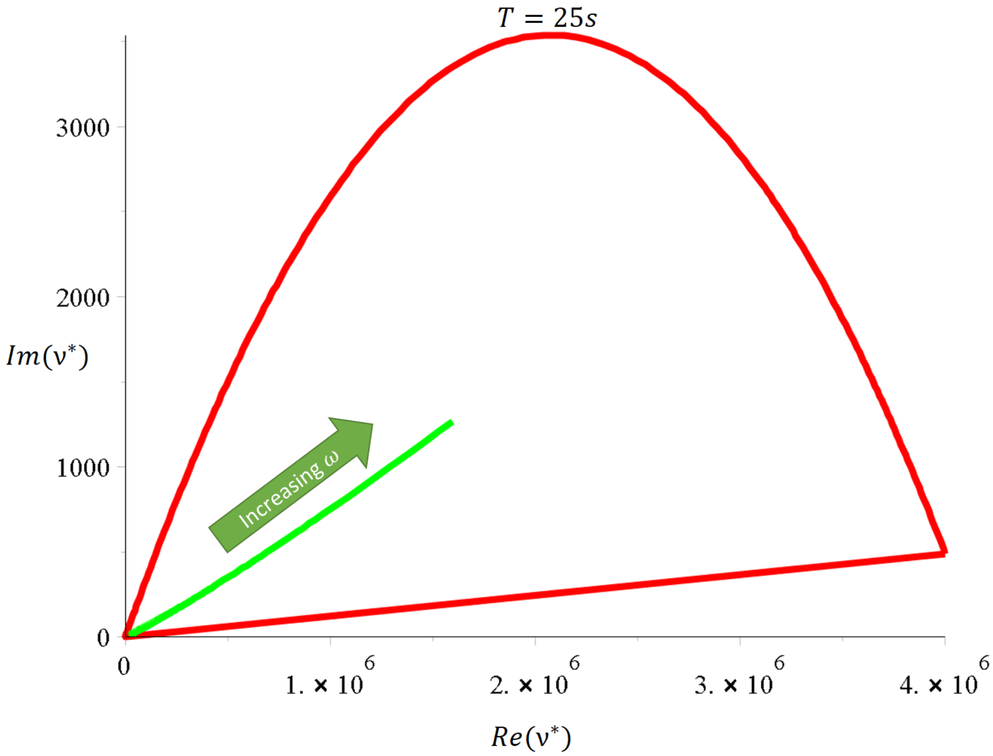

Figure 8.3: Bounds for $\bar{\nu}^*$ and $T = 25s$ with $G = 10^7 Pa$ for the ice phase. We have plotted the complex conjugate of ν^* to better highlight the contrast in the parameters. In green are data extracted from the 1-d model and the work in [13, 22] for periods $6s \leq T \leq 16s$. Here the volume fraction of ice is $p = 0.4$, in the range for which we consider the data valid.

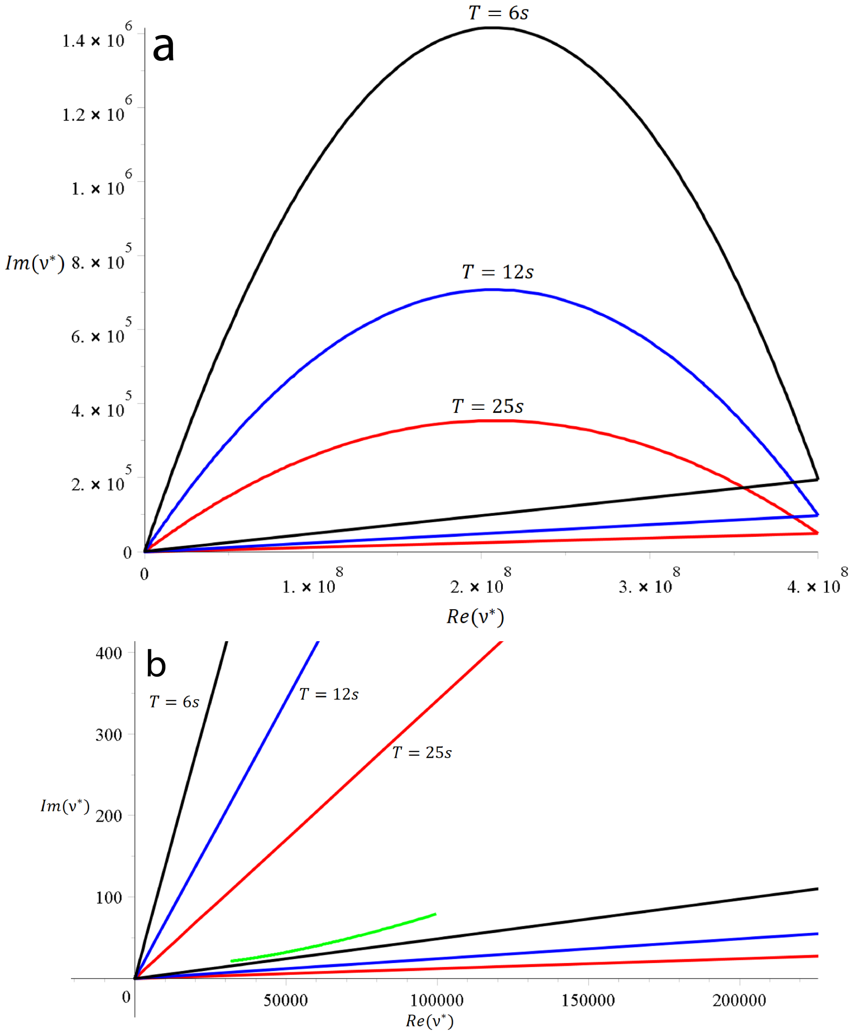

Figure 8.4: The bounds when the shear modulus of the ice phase is taken to be $10^9 Pa$. In (a) we show the bounds for $\bar{\nu}^*$ plotted for several periods, $T = 2\pi/\omega$, with $G = 10^9 Pa$, $\nu = 0.014 m^2/s$. In (b) we zoom in to show where the data lie. We have plotted the complex conjugate of ν^* to better highlight the contrast in the parameters. Bottom: Zoomed in, in green are data extracted from the 1-d model and the work in [13, 22] for periods $6s \leq T \leq 25s$. Note that near $T = 6s$ the data just begin to violate the bounds. This suggests a lower limit for which the long wave length assumption is valid. Here the volume fraction of ice is $p = 0.4$, in the range for which we consider the data valid. We note though that near the ice edge $G = 10^9$ may be too high.

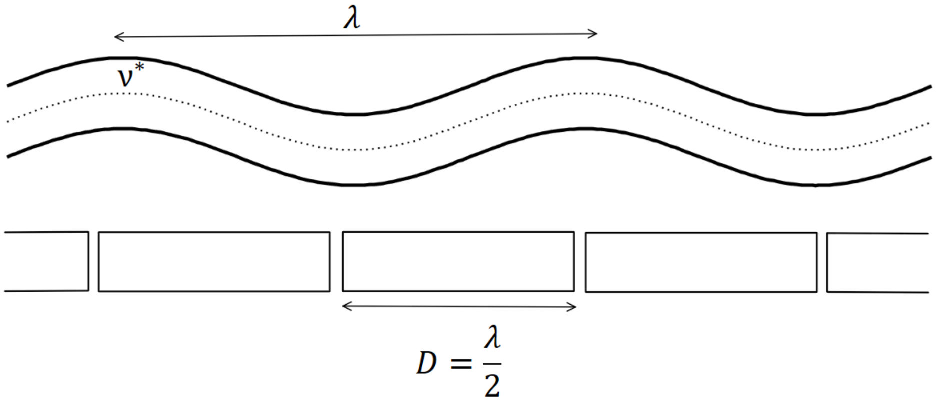

Figure 8.5: The ice modeled as a viscoelastic plate which can break into pieces of size $\lambda/2$ for waves with sufficient amplitude.

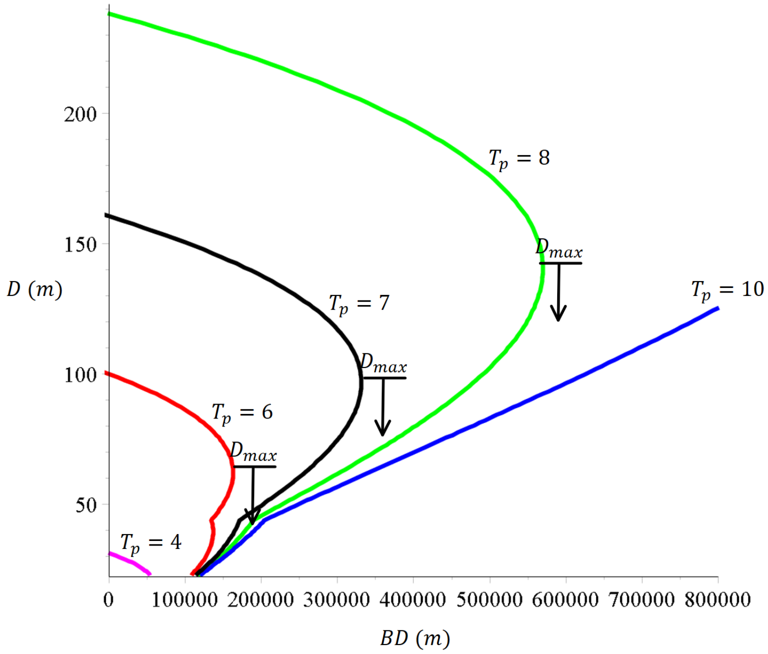

Figure 8.6: Maximum floe size as a function of distance from the ice edge for waves of period $6s \leq T \leq 16$ with $h = 0.85$ for each curve. The distance a given wave may break ice in the MIZ depends sensitively on peak period T_p. Note that we define the maximum floe size at a given distance from the ice edge to be the minimum floe size produced by waves with sufficient amplitude to fracture the ice at that position.

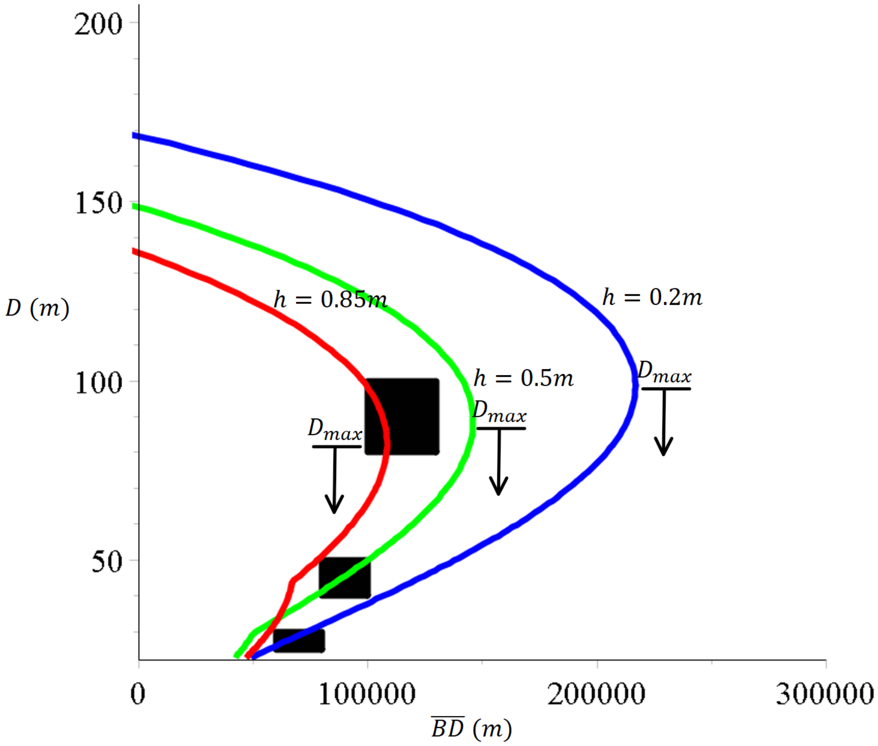

Figure 8.7: The average breaking distance and maximum floe size for ice thicknesses of $h = 0.2, 0.5, 0.85$ and waves of period $6s \leq T \leq 16$. The black rectangles represent measurements of the maximum floe size in the Antarctic MIZ from [36]. Note that we define the maximum floe size at a given distance from the ice edge to be the minimum floe size produced by waves with sufficient amplitude to fracture the ice at that position.

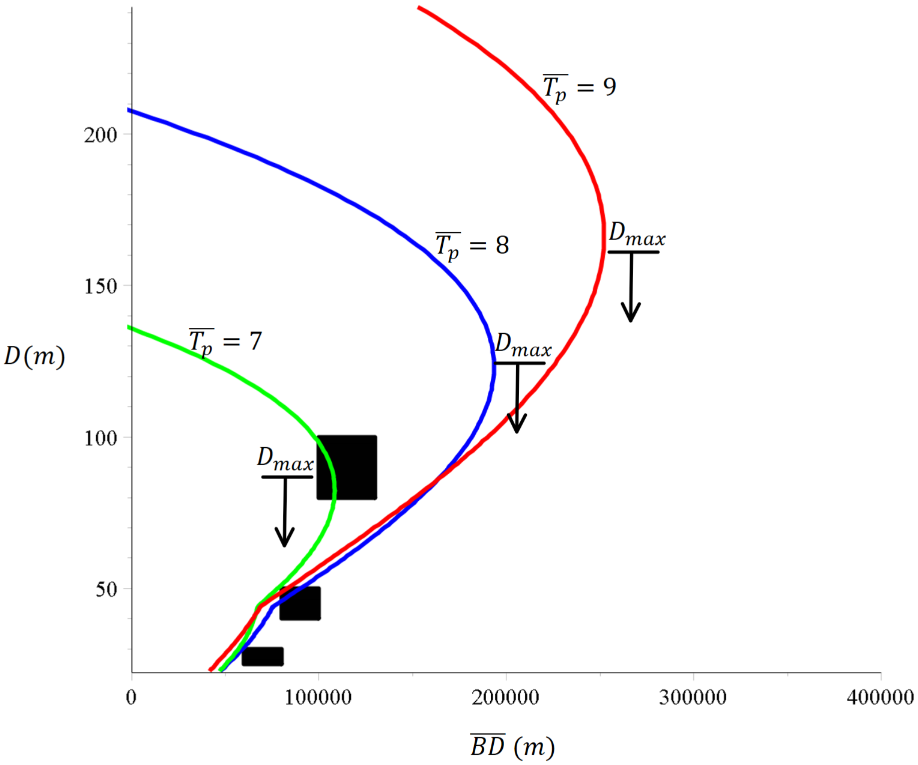

Figure 8.8: The average breaking distance and maximum floe size for varying average peak periods, $\bar{T}_P = 7, 8, 9$ all with standard deviation $S_d = 1$. Here the thickness is $h = 0.85m$ and we consider wave periods of $6s \leq T \leq 16$. Note that we define the maximum floe size at a given distance from the ice edge to be the minimum floe size produced by waves with sufficient amplitude to fracture the ice at that position.

8.7 References

[1] Howard F. Bates and Lewis H. Shapiro. Long-period gravity waves in ice-covered sea. *Journal of Geophysical Research*, 85(C2):1095, 1980.

[2] Morris A Bender, Thomas R Knutson, Robert E Tuleya, Joseph J Sirutis, Gabriel A Vecchi, Stephen T Garner, and Isaac M Held. Modeled impact of anthropogenic warming on the frequency of intense Atlantic hurricanes. *Science*, 327(5964):454–458, 2010.

[3] David J Bergman. Rigorous bounds for the complex dielectric constant of a two-component composite. *Annals of Physics*, 138(1):78–114, jan 1982.

[4] Carlos Bonifasi-Lista and Elena Cherkaev. *Identification of Bone Microstructure from Effective Complex Moduls*, pages 91–96. Springer Netherlands, Dordrecht, 2007.

[5] Carlos Bonifasi-Lista and Elena Cherkaev. Analytical relations between effective material properties and microporosity: Application to bone mechanics. *International Journal of Engineering Science*, 46(12):1239–1252, dec 2008.

[6] Oscar P. Bruno and Perry H. Leo. On the stiffness of materials containing a disordered array of microscopic holes or hard inclusions. *Archive for Rational Mechanics and Analysis*, 121(4):303–338, 1993.

[7] D.E. Carlson and Y.C. Chen. *Advances in Continuum Mechanics and Thermodynamics of Material Behavior: In Recognition of the 60th Birthday of Roger L. Fosdick*. Springer Netherlands, 2012.

[8] Elena Cherkaev and Carlos Bonifasi-Lista. Characterization of structure and properties of bone by spectral measure method. *Journal of Biomechanics*, 44(2):345–351, jan 2011.

[9] GF Dell'Antonio, R Figari, and E Orlandi. An approach through orthogonal projections to the study of inhomogeneous or random media with linear response. In *Annales de l'IHP Physique théorique*, volume 44, pages 1–28, 1986.

[10] D. Dumont, A. Kohout, and L. Bertino. A wave-based model for the marginal ice zone including a floe breaking parameterization. *Journal of Geophysical Research*, 116(C4), apr 2011.

[11] N. Dunford and J.T. Schwartz. *On Point Measures*. Wiley, Hoboken, NJ, 1998.

[12] Kerry Emanuel. Increasing destructiveness of tropical cyclones over the past 30 years. *Nature*, 436(7051):686–688, 2005.

[13] Colin Fox and Tim G. Haskell. Ocean wave speed in the Antarctic marginal ice zone. *Annals of Glaciology*, 33(1):350–354, jan 2001.

[14] K. Golden. Bounds on the complex permittivity of a multicomponent material. *Journal of the Mechanics and Physics of Solids*, 34(4):333–358, jan 1986.

[15] K. Golden. Bounds on the complex permittivity of sea ice. *Journal of Geophysical Research*, 100(C7):13699, 1995.

[16] K. Golden and G. Papanicolaou. Bounds for effective parameters of heterogeneous media by analytic continuation. *Communications in Mathematical Physics*, 90(4):473–491, dec 1983.

[17] Joseph B. Keller. Gravity waves on ice-covered water. *Journal of Geophysical Research: Oceans*, 103(C4):7663–7669, apr 1998.

[18] Thomas R. Knutson, Joseph J. Sirutis, Stephen T. Garner, Gabriel A. Vecchi, and Isaac M. Held. Simulated reduction in atlantic hurricane frequency under twenty-first-century warming conditions. *Nature Geoscience*, 1(6):359–364, 2008.

[19] A. L. Kohout, M. J. M. Williams, S. M. Dean, and M. H. Meylan. Storm-induced sea-ice breakup and the implications for ice extent. *Nature*, 509(7502):604–607, may 2014.

[20] Alison L. Kohout, Michael H. Meylan, and David R. Plew. Wave attenuation in a marginal ice zone due to the bottom roughness of ice floes. *Annals of Glaciology*, 52(57):118–122, may 2011.

[21] Patricia J. Langhorne, Vernon A. Squire, Colin Fox, and Timothy G. Haskell. Break-up of sea ice by ocean waves. *Annals of Glaciology*, 27(1):438–442, 1998.

[22] Michael H. Meylan, Luke G. Bennetts, and Alison L. Kohout. In situ measurements and analysis of ocean waves in the Antarctic marginal ice zone. *Geophysical Research Letters*, 41(14):5046–5051, jul 2014.

[23] G. W. Milton. Bounds on the complex permittivity of a two-component composite material. *Journal of Applied Physics*, 52(8):5286–5293, aug 1981.

[24] G.W. Milton. *The Theory of Composites*. Cambridge Monographs on Applied and Computational Mathematics. Cambridge University Press, 2002.

[25] Johannes E. M. Mosig, Fabien Montiel, and Vernon A. Squire. Comparison of viscoelastic-type models for ocean wave attenuation in ice-covered seas. *Journal of Geophysical Research: Oceans*, 120(9):6072–6090, sep 2015.

[26] N. Benjamin Murphy, Elena Cherkaev, Christel Hohenegger, and Kenneth M. Golden. Spectral measure computations for composite materials. *Communications in Mathematical Sciences*, 13(4):825–862, 2015.

[27] Karl Newyear and Seelye Martin. Comparison of laboratory data with a viscous two-layer model of wave propagation in grease ice. *Journal of Geophysical Research: Oceans*, 104(C4):7837–7840, apr 1999.

[28] Martin Ostoja-Starzewski. Material spatial randomness: From statistical to representative volume element. *Probabilistic Engineering Mechanics*, 21(2):112–132, apr 2006.

[29] Miao-Jung Ou and Elena Cherkaev. On the integral representation formula for a two-component elastic composite. *Mathematical Methods in the Applied Sciences*, 29(6):655–664, 2006.

[30] Willard J. Pierson and Lionel Moskowitz. A proposed spectral form for fully developed wind seas based on the similarity theory of S. A. Kitaigorodskii. *Journal of Geophysical Research*, 69(24):5181–5190, dec 1964.

[31] J. Schwarz, R. Frederking, V. Gavrillo, I.G. Petrov, K.-I. Hirayama, M. Mellor, P. Tryde, and K.D. Vaudrey. Standardized testing methods for measuring mechanical properties of ice. *Cold Regions Science and Technology*, 4(3):245–253, jul 1981.

[32] V.A. Squire. Of ocean waves and sea-ice revisited. *Cold Regions Science and Technology*, 49(2):110–133, aug 2007.

[33] G.W. Timco and S. O'Brien. Flexural strength equation for sea ice. *Cold Regions Science and Technology*, 22(3):285–298, mar 1994.

[34] G.W. Timco and W.F. Weeks. A review of the engineering properties of sea ice. *Cold Regions Science and Technology*, 60(2):107–129, feb 2010.

[35] S Tokarzewski, JJ Telega, and A Gałka. Torsional rigidities of cancellous bone filled with marrow: The application of multipoint pads approximants. *Engineering Transactions*, 49(2-3):135–153, 2001.

[36] Takenobu Toyota, Christian Haas, and Takeshi Tamura. Size distribution and shape properties of relatively small sea-ice floes in the Antarctic marginal ice zone in late winter. *Deep Sea Research Part II: Topical Studies in Oceanography*, 58(9-10):1182–1193, may 2011.

[37] P. Wadhams. SAR imaging of wave dispersion in Antarctic pancake ice and its use in measuring ice thickness. *Geophysical Research Letters*, 31(15), 2004.

[38] Ruixue Wang and Hayley H. Shen. Gravity waves propagating into an ice-covered ocean: A viscoelastic model. *Journal of Geophysical Research*, 115(C6), June 2010.

[39] Anthony P. Worby, Cathleen A. Geiger, Matthew J. Paget, Michael L. Van Woert, Stephen F. Ackley, and Tracy L. DeLiberty. Thickness distribution of Antarctic sea ice. *Journal of Geophysical Research*, 113(C5), may 2008.

[40] Xin Zhao and Hayley H. Shen. Wave propagation in frazil/pancake, pancake, and fragmented ice covers. *Cold Regions Science and Technology*, 113:71–80, may 2015.

CHAPTER 9

SUMMARY OF THE MULTISCALE MODELS OF SEA ICE PRESENTED IN THIS DISSERTATION

In this dissertation we have investigated mathematical models of sea ice phenomena on multiple scales. On the scale of sea ice microstructure, we have investigated the applicability of percolation theory in modeling both electrical transport and fluid transport through the porous structure of the ice. We find that there is a strong electrical signature at the critical brine volume fraction threshold of about 5% in columnar sea ice. Before this threshold, the ice is effectively impermeable to fluid flow. This is known as *the rule of fives*. We further find that the vertical electrical conductivity of sea ice follows a universal power law, explained by percolation theory, as a function of brine volume fraction above the 5% threshold. This allows us to link specific electrical profiles of the ice to important state variables of the ice pack. These findings open the door to new generations of *in situ* analysis and remote monitoring of transport processes.

We have also investigated the differences in electrical and fluid transport in different crystallographic types of ice. Continuum percolation theory and the compressed powder model predict that for granular sea ice, the critical threshold for fluid flow should be around 10%. Further, as with columnar ice, the permeability should exhibit universal power law behavior. Indeed, experiments done during the SIPEX II expedition in 2012 confirm this result. Interestingly, however, we do not see correspondence between the fluid and electrical thresholds in granular ice. This can be explained by the fact that fluid requires larger channels for flow than does electrical current. We do however find greater variability in the vertical conductivity of granular sea ice. That is, the vertical conductivity of columnar sea ice changes continuously as brine volume fraction increases; this is not the case for granular ice. This fact could be used to develop inversion schemes which could potentially detect ice type by noting changes in the conductivity as the ice temperature changes. This is important due to the stark contrast in the critical threshold of 5% and 10% between the two ice types for fluid flow.

On the medium scale, we explored the applicability of surface impedance tomography in the determination of ice thickness and composition. Using indirect measurements of the electrical conductivity of Antarctic sea ice, we developed an n-layer inversion scheme to reconstruct resistivity profiles from Wenner array data taken during the SIPEX I expedition in 2007. Through the linkages between the fluid and electrical transport properties discussed above, this potentially provides a method to monitor important state variables in the ice pack, in particular, thickness, which is an important parameter for many large scale climate models and is difficult to obtain remotely.

On the larger scale, we developed a method of extracting the essential connectivity and scale characteristics of complex melt pond configurations from photographic images of melt pond structures. Further, we mapped the melt pond connections onto discrete conductance networks for which the effective conductance can be calculated. The effective conductance can serve as a way to estimate the ease of lateral flow. This is important since connected ponds allow melt water to flow to large drainage structures. Understanding how easily this flow can progress is important to large scale sea ice models since melt ponds are the major controlling factor of sea ice albedo.

Also on the larger scale, we explore wave-ice interactions in the marginal ice zone. In particular, we derive the first rigorous bounds on the effective viscoelasticity of the ice water-mix. With much recent interest in using continuum models, which depend on this effective parameter to model wave propagation in the MIZ, these bounds provide a way to estimate the effective viscoelasticity based on the concentration and geometry of the floes. We also developed a simplified wave equation for the propagation of plane-like waves in the marginal ice zone which produces a dispersion relation that defines the wave number and attenuation rate of the traveling wave through the effective viscoelasticity. Through that relation we also extracted estimates of the effective viscoelasticity from measurements of waves in the marginal ice zone made during the SIPEX II expedition in 2012. Using these estimates and our simplified wave equation, we further explored a 1-d model of ice floe breaking by waves. This model is analytic in nature and is capable of capturing many of the average properties of both the floe size distribution in the marginal ice zone as well as its extent.